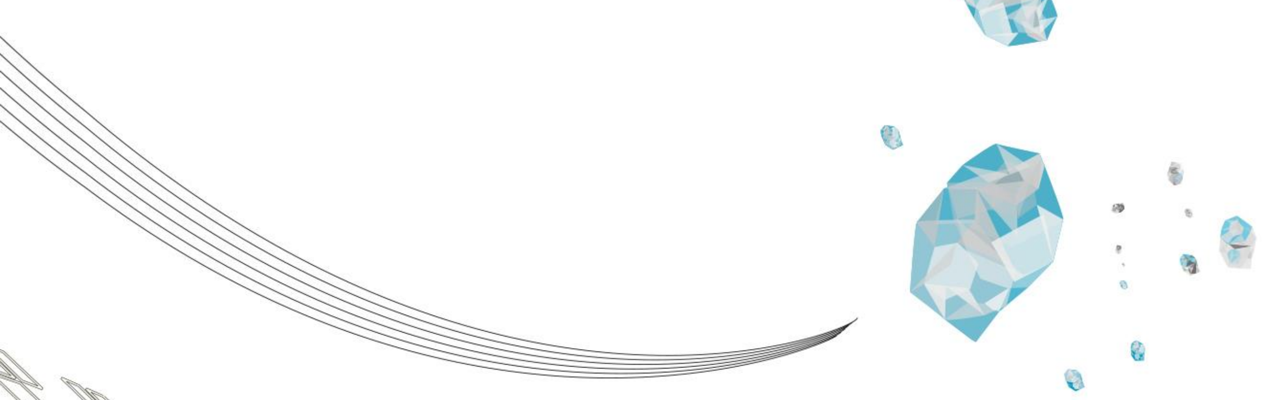

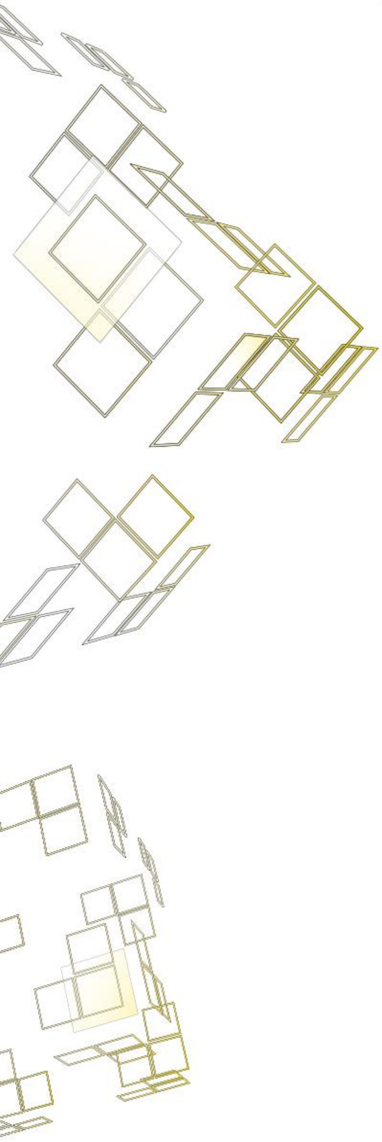

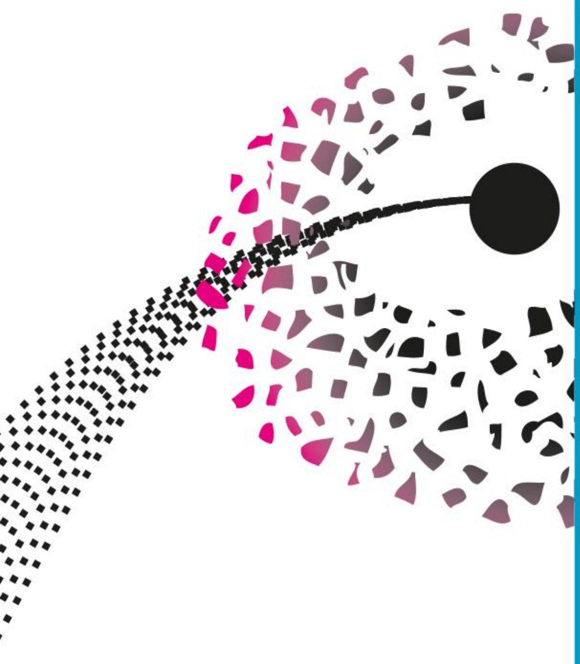

QUANTIFICATION OF CALCIFICATION IN PERIPHERAL ARTERIAL DISEASE USING DUAL-ENERGY COMPUTED TOMOGRAPHY ANGIOGRAPHY

MASTER THESIS

TECHNICAL MEDICINE – MEDICAL IMAGING & INTERVENTIONS

R.B.M. WIGGERS

16 MAY 2022

UMC UTRECHT – DEPARTMENT OF VASCULAR SURGERY

UNIVERSITY OF TWENTE.

Graduation committee

Technological supervisor & Chairman	Prof. dr. ir. C.H. Slump Department of Robotics and Mechatronics (RAM) Faculty of Electrical Engineering, Mathematics and Computer Science (EEMCS) University of Twente, Enschede, The Netherlands
Medical supervisor	Dr. C.E.V.B. Hazenberg Department of Vascular Surgery University Medical Center Utrecht, Utrecht, The Netherlands
Process supervisor	Drs. N.S. Cramer Bornemann Technical Medicine (TM) Faculty of Science and Technology (TNW) University of Twente, Enschede, The Netherlands
External member	Dr. E. Groot Jebbink Multi-Modality Medical Imaging Group (M3I) Faculty of Science and Technology (TNW) University of Twente, Enschede, The Netherlands

Acknowledgements

This thesis is the final product of my graduation internship at the department of Vascular Surgery of the University Medical Center Utrecht. During these challenging and very educational 10 months, I have gotten the opportunity to develop myself as a healthcare professional, both clinically and scientifically, which I am very grateful for. Therefore, I would like to take this opportunity to express my gratitude to the people who helped me during this internship.

First, I am grateful to all the clinicians and researchers at the department of Vascular Surgery of the UMC Utrecht, for allowing me to take an active role in clinical care and research meetings and thus gain a lot of experience. I would in particular like to thank my medical supervisor, dr. Stijn Hazenberg, for his continuous involvement in the research project and my clinical activities. You were always available whenever I needed help or your advice. I have really enjoyed working together during this internship and I look forward to working together after my graduation as well.

Likewise, I am very grateful to prof. Kees Slump for his input in the research project. Thank you for reminding me to keep the clinical need in mind throughout all steps of the research project and for steering me in the right direction with critical questions. Thank you as well for your thorough comments on the draft version of this thesis, which have really benefitted the quality of this work.

I would also very much like to thank my process supervisor, drs. Nicole Cramer Bornemann, for her guidance throughout two years of internships and for encouraging me to continuously reflect on my own behavior and take an active role in my learning process. I look back positively on our intervision meetings and I’m sure the insights I have learned in these meetings will be useful throughout my career.

I would also like to extend my sincere thanks to dr. Madeleine Kok and dr. Arnold Schilham from the departments of Radiology and Clinical Physics of the UMC Utrecht, for their help with the phantom experiment and analysis of patient data.

Finally, I want to thank my family and friends for all their support, trust and patience throughout this year. Without this, I doubt I would have been able to finish this internship within this time frame.

List of abbreviations and acronyms

Abbreviations and acronyms	
ACM	All-cause mortality
ACS	Angiographic calcium score
BDC	Body densitometry calibration
CaHA	Calcium hydroxyapatite
CM/M	Cardiac morbidity and mortality
CT	Computed tomography
CTA	Computed tomography angiography
CLI	Critical limb ischemia
CLTI	Chronic limb-threatening ischemia
DECT	Dual-energy computed tomography
DECTA	Dual-energy computed tomography angiography
DFU	Diabetic foot ulcer
DM	Diabetes mellitus
DSA	Digital subtraction angiography
EBR	Evidence-based revascularization
EC	Extensive calcification
FMM	Fast Marching Method
FP	Femoropopliteal
GLASS	Global Limb Anatomic Staging System
GVG	Global Vascular Guidelines
HR	Hazard ratio
HU	Hounsfield Units
IC	Intermediate calcification
IP	Infrapopliteal
IQR	Interquartile range
kVp	Peak kilovoltage
LLAC	Lower limb arterial calcification
LLL	Late lumen loss
MAC	Medial arterial calcification
MACE	Major adverse cardiovascular events
MALE	Major adverse limb events
MIP	Maximum intensity projection
MC	Minimal calcification
OR	Odds ratio
PACSS	Peripheral arterial calcium scoring system
PAD	Peripheral arterial disease
PRISMA	Preferred Reporting Items for Systematic reviews and Meta-Analyses
ROI	Region of interest
SFA	Superficial femoral artery
SVS	Society for Vascular Surgery
TAC	Tibial artery calcification
TAP	Target arterial path
TLR	Target lesion revascularization
UMC	University Medical Center
VME	Virtual mono-energetic
VNC	Virtual non-contrast
WIfI	Wound, Ischemia and foot Infection

Table of contents

Thesis outline

The aim of the research project for this internship is to explore the possibility of quantifying peripheral arterial calcification and its implications for clinical outcomes in patients with peripheral arterial disease. This thesis documents the methods and results of this study.

The thesis starts with a general introduction, which describes the clinical background of peripheral arterial disease and the current best practice for risk stratification in this patient group. The need for quantitative calcium scoring as an additional means for risk stratification is introduced in this section as well, from which the research objectives for this project follow.

Chapter 1 is a systematic review exploring the methods for calcification scoring which have been described and the evidence on the association between peripheral calcification and clinical outcomes currently available in literature. This review will be submitted for publication in the European Journal of Vascular and Endovascular Surgery (ISSN: 1078-5884).

Chapter 2 documents the results of a phantom experiment, which was conducted to investigate the potential of spectral computed tomography for quantification of calcification and separation of calcification from iodine contrast agent in a controlled setting.

Chapter 3 describes the development of a workflow for segmentation and quantification of calcifications in patients with peripheral arterial disease based on spectral computed tomography angiography data. As a proof of concept, the performance of this workflow is assessed based on the data for six patients.

Finally, the thesis will conclude with a general discussion and conclusion, in which the results and limitations of this research project will be summarized and discussed and an outlook will be provided on the future perspectives of this research line.

General introduction

Clinical background

Peripheral arterial disease (PAD) is characterized by progressive stenosis or occlusion of the arteries supplying the lower extremity and is associated with significant morbidity and mortality [1,2]. PAD may cause ischemia of the affected limb and result in intermittent claudication, defined as limb pain that occurs with exercise and is relieved by rest [1,3]. As a result, symptomatic PAD leads to loss of function of the affected limbs, which exhibits through significantly reduced walking distance and leads to a reduced quality of life and an increased rate of depression in afflicted patients [4]. Moreover, a significant proportion of patients who are asymptomatic or experience intermittent claudication continue to develop chronic limb-threatening ischemia (CLTI), with reported estimates ranging from 5 to 21% within five years [2]. CLTI, which is characterized by rest pain, persistent wounds and infections, and gangrenous lesions, has been associated with high rates of amputation, even in patients who successfully undergo revascularization [1,2]. This not only leads to substantial disability, but also significantly increases mortality rate, which has been reported to be as high as 50% within 5 years after amputation [1,2]. In addition, PAD in general has been associated with an increased risk of coronary artery disease, major adverse cardiovascular events such as myocardial infarction or cerebrovascular accidents, and overall mortality [1,2]. The global prevalence of PAD was estimated to be over 200 million in 2010, marking a 23.5% increase in prevalence between 2000 and 2010, a rise which has been mainly attributed to aging of the general population and the increasing collective burden of cardiovascular risk factors, particularly diabetes mellitus (DM) [2,5,6]. Due to this increase, which is expected to continue over the following decades, PAD can be expected to impose an increasing burden on patients and healthcare resources [1,2,6].

Identifying which patients are at risk of these far-reaching consequences remains difficult. Severe PAD may be recognized too late, causing irreparable damage to the limb by deferring endovascular evaluation and adequate treatment [1]. This is illustrated by the findings of Goodney et al., who have observed that 54% of 20,464 patients undergoing major amputation of the lower limb had not received any vascular procedure in the year leading up to amputation [7]. Similarly, Reinecke et al. found that "among 4,298 amputated patients with CLI, 37% had not received any angiography or revascularization neither during index hospitalization nor the 24 months before" [8]. Consequently, there is need for prognostic markers which can identify patients at high risk for adverse events, such as amputation. After all, early detection of high-risk patients may allow for targeted patient education, lifestyle intervention and endovascular treatment, thus averting or deferring adverse outcomes [1].

Risk stratification: current best practice

The search for prognostic markers to identify patients at high risk for amputation and other adverse events has been a major research focus. The 2019 Global Vascular Guidelines (GVG) on the Management of Chronic Limb-Threatening Ischemia, an international initiative of several leading vascular societies, emphasize the concept of evidence-based revascularization (EBR) [2]. To this end, the GVG propose the PLAN framework to support clinical decision-making [2]. This framework consists of three components, i.e. Patient risk, Limb severity and ANatomic pattern of disease, which should be assessed in that order of priority [2]. These components will be discussed briefly in this paragraph.

The first step in the PLAN framework, 'Patient risk', concerns assessment of the patient's condition, periprocedural risk, and life expectancy. After all, while the severity of limb threat may necessitate treatment and the anatomic pattern of disease may allow for intervention, the condition of the patient may contraindicate intervention. Therefore, the risk and invasiveness associated with the projected intervention should be weighed against the expected hemodynamic and functional gain. Several risk stratification tools have been developed to aid in this decision, such as Finnvasc or PREVENT III. These tools incorporate risk factors (e.g. smoking, BMI), comorbidities (such as DM or chronic kidney disease) and other measures such as frailty. [2]

The second component in the framework for EBR involves staging the severity of limb threat. Traditionally, in vascular surgery, the Fontaine or Rutherford classifications are used for this and these systems are still highly prevailing in clinical practice. However, these classifications are ischemia-dominant and do not adequately reflect the complex interaction of ischemia, polyneuropathy, wound characteristics and infection often seen in CLTI patients as DM steadily replaces smoking as the most prevalent risk factor. [2] Therefore, the GVG instead advise the use of the Society for Vascular Surgery (SVS) WIfI classification (See Table 1) [2,9]. This system grades the limb on Wound, Ischemia and foot Infection components in a way analogous to the TNM classification used in oncology, making use of clinical signs and symptoms as well as objective hemodynamic studies [2,9]. The SVS WIfI classification has been shown to correlate with limb salvage, risk of amputation and wound healing and can aid in determining which patients likely benefit from revascularization [2,10].

The third and final part of the PLAN framework entails assessment of the anatomic pattern of disease, for which the GVG introduce the Global Limb Anatomic Staging System (GLASS) [2]. This system focuses on infrainguinal disease, as adequate classifications for aorto-iliac disease had already been defined, such as TASC II [2,4].

GLASS, which is based on angiography, integrates the anatomic pattern of disease at multiple arterial levels; this is advantageous within the context of defining revascularization strategies, as successful revascularization typically requires restoration of in-line (i.e. along an uninterrupted arterial path), pulsatile flow to the foot. GLASS concerns two main segments: the femoropopliteal (FP) segment, defined from the origin of the superficial femoral artery (SFA) to the trifurcation at the end of the popliteal artery, and the infrapopliteal (IP) segment, defined as the crural arteries including the tibioperoneal trunk. Each of these segments is scored between 0 and 4 based on the severity of disease within the segment; for the infrapopliteal (IP) segment, this requires the definition of a target arterial path (TAP), which is defined as the optimal arterial path to return in-line, pulsatile flow to the foot and usually involves the least diseased artery. The FP and IP grades are then combined into a single GLASS stage according to the scheme shown in Table 2. GLASS also includes an inframalleolar (below the ankle) modifier to describe the status of the pedal vessels. However, this modifier is presently not considered in the global GLASS stage, due to a lack of evidence on the outcomes of pedal (endo)vascular intervention, which is rarely performed; this modifier is therefore not shown in this paragraph for the sake of brevity. As is shown in Table 3, the GLASS stages are correlated with technical success of and limb-based patency after peripheral endovascular intervention. [2]

These efforts to predict the likelihood of clinical outcomes and the expected success of endovascular treatment mark an effort towards EBR in PAD patients. However, there is only a limited role in the aforementioned classifications for peripheral calcifications, which are considered a characteristic feature of atherosclerosis and have been associated with a poor prognosis in vascular disease [11,12]. In the GLASS classification, the within-segment grade of the FP or IP segment is increased by one point in the presence of severe calcification (such as calcification spanning >50% of circumference, or diffuse, bulky or “coral reef” plaques); this is judged subjectively, based solely on visual inspection and the treating physician’s experience [2]. The ‘Patient Risk’ and ‘Limb severity’ steps do not involve any measure of vessel calcification.

Table 1: The Society for Vascular Surgery Wound, Ischemia and foot Infection (SVS WIfI) classification. [9,13]

Wound		
Grade	**Ulcer**	**Gangrene**
0	No ulcer	No gangrene
	Clinical description: ischemic rest pain (requires typical symptoms + ischemia grade 3); no wound.	
1	Small, shallow ulcer on distal leg or foot; no exposed bone, unless limited to distal phalanx	No gangrene
	Clinical description: minor tissue loss. Salvageable with simple digital amputation (1 or 2 digits) or skin coverage.	
2	Deeper ulcer with exposed bone, joint, or tendon; generally not involving the heel; shallow hell ulcer, without calcaneal involvement	Gangrenous changes limited to digits
	Major tissue loss salvageable with multiple (≥3) digital amputation or standard TMA ± skin coverage.	
3	Extensive, deep ulcer involving forefoot and/or midfoot; deep, full-thickness heel ulcer ± calcaneal involvement	Extensive gangrene involving the forefoot/midfoot; full-thickness heel necrosis ± calcaneal involvement
	Clinical description: extensive tissue loss salvageable only with a complex foot reconstruction (nontraditional TMA, Chopart, or Lisfranc amputation); flap coverage or complex wound management needed for large soft tissue defect.	

Ischemia			
Grade	**ABI**	**Ankle systolic pressure**	**TP, $TcPO_2$**
0	≥ 0.80	> 100 mm Hg	≥ 60 mm Hg
1	0.60 – 0.79	70 – 100 mm Hg	40 – 59 mm Hg
2	0.40 – 0.59	50 – 70 mm Hg	30 – 39 mm Hg
3	≤ 0.39	< 50 mm Hg	< 30 mm Hg

foot Infection	
Grade	**Clinical manifestation of infection**
0	No symptoms or signs of infection
1	Local infection involving only the skin and subcutaneous tissue, no signs of SIRS, erythema >0.5 cm to ≤2 cm
2	Local infection with erythema >2 cm or involving structures deeper than skin and subcutaneous tissue, without signs of SIRS
3	Local infection with signs of SIRS

Abbreviations: TMA, transmetatarsal amputation; ABI, ankle brachial index; TP, toe pressure; $TcPO_2$, transcutaneous oximetry; SIRS, systemic inflammatory response syndrome; Pa_{CO2}, partial pressure of carbon dioxide.

Table 2: Assignment of Global Limb Anatomic Staging System (GLASS) Stage based on individual femoropopliteal (FP) and infrapopliteal (IP) [2].

FP Grade	**IP Grade**				
	0	**1**	**2**	**3**	**4**
4	III	III	III	III	III
3	II	II	II	III	III
2	I	II	II	II	III
1	I	I	II	II	III
0	NA	I	I	II	III

Abbreviation: NA, not applicable.

Table 3: Description of Global Limb Anatomic Staging System (GLASS) stages and its implications for the expected success of peripheral (endo)vascular intervention [2].

GLASS Stage	**Technical Failure**	**1-year LBP**	**Anatomic pattern**
I	<10%	>70%	Short- to intermediate-length FP disease and/or short-length IP disease; no or minimal popliteal disease
II	<20%	50-70%	Intermediate- to long-length FP disease; may include popliteal stenosis and/or short- to intermediate-length FP disease.
III	>20%	<50%	Extensive FP or IP occlusions, alone or in combination with any disease in the other segment; popliteal CTO

Abbreviations: LBP, limb-based patency; FP, femoropopliteal; IP, infrapopliteal; CTO, chronic total occlusion.

In symptomatic coronary artery patients, on the other hand, quantitative scoring of coronary artery calcium has been used successfully to quantify the extent of atherosclerotic disease and predict the risk of adverse events [14,15]. The coronary artery calcium score has been shown to surpass traditional cardiovascular risk factors as a predictor of cardiovascular events and mortality, which has lead to its widespread application for risk stratification in clinical practice [15,16]. Furthermore, aortic calcification has been correlated with cardiovascular events and mortality in the general population [17]. Based on these results, a similar correlation may be predicted to exist between peripheral artery calcification and late clinical outcomes. Moreover, severe calcification of target vessels represents a challenge to revascularization approaches, which may suggest a relationship between calcification and technical success of endovascular intervention [18].

However, there is a lack of reliable evidence on the clinical implications of peripheral arterial calcification, which may be partly due to the frequent exclusion of severely calcified lesions from clinical trials in this patient group [18]. As such, there is a need for further research into methods to quantify the peripheral arterial calcium burden and its implications for clinical practice; this thesis will make an effort towards this aim.

Research objectives

The research objectives and questions of this study can be summarized as follows:

1. To synthesize the available evidence on peripheral arterial calcium scoring in a systematic review.
    a. Which methods are currently used to quantify peripheral arterial calcification?
    b. What is the prognostic value of peripheral arterial calcification scoring?
2. To develop a standard, image-based peripheral arterial calcium score;
    a. Validation of dual-energy computed tomography (CT) imaging;
        i. To what extent can virtual non-contrast scans, with a suppression profile adequate for calcification scoring, be reconstructed based on dual-energy CT angiography (CTA) scans?
        ii. To what extent can dual-energy CT imaging accurately quantify calcification in terms of volume and density?
    b. Development of a workflow for segmentation of peripheral arterial calcifications;
        i. What are the required specifications for the segmentation workflow in terms of speed, reproducibility and accuracy/precision based on clinical practice?
        ii. To what extent can peripheral arterial calcifications be segmented based on dual-energy CTA imaging and do these segmentations meet the clinical requirements?
    c. Calculation of a peripheral arterial calcium score;
        i. Which components of peripheral artery calcification exhibit the largest predictive value?
        ii. How should the aspects of calcification predictive of clinical outcomes be combined into a peripheral arterial calcium score?
3. Investigation of the association between the developed calcium score and clinical outcomes;
    a. What is the association between increasing peripheral arterial calcium scores and clinical outcomes?

Chapter 1 – A systematic review into the association between calcification and clinical outcomes in peripheral arterial disease patients.

Abstract

Peripheral arterial disease (PAD) is associated with significant morbidity and mortality. Patients may develop chronic limb-threatening ischemia, which carries a high risk of amputation. This causes significant disability and further increases the mortality. Identification of patients at high risk of adverse events remains challenging. Calcification of both the coronary arteries and the aorta have previously been shown to predict cardiovascular events and mortality. Therefore, a similar association between peripheral artery calcifications and clinical events might exist. The objective of this study is to review the available evidence on the association between peripheral artery calcification, quantified using medical imaging, and clinical outcomes, including major adverse limb events (MALE; including amputation rate and target lesion revascularization rate (TLR)), major adverse cardiovascular events (MACE; including myocardial infarction, stroke and all-cause mortality) and technical success of endovascular treatment in patients with PAD. The different methods by which calcifications were scored were explored as well.

A systematic literature search conducted in PubMed and Embase yielded 1,282 records which were screened on title and abstract. Studies were included if they (1) reported original data, (2) recruited symptomatic PAD patients, (3) assessed arterial calcification with a quantitative or semi-quantitative calcium score based on imaging and (4) compared clinical outcomes between patients with a range of calcification scores. Twenty studies satisfied the inclusion criteria, of which four were found by cross-referencing included articles.

A significant association was found between calcium scores and severity of ischemia, technical success and patency, suggesting that imaging-based calcium scoring may be used to inform a tailor-made treatment strategy for each individual patient. The included studies also showed a trend towards increased risk of amputation, TLR, MALE, MACE and all-cause mortality in patients with higher calcium scores. However, this result should be interpreted cautiously in light of relatively low sample sizes and study limitations. Further research in large cohorts should confirm these associations. Further research should also focus on determining which calcium score is the best predictor of these clinical outcomes and on developing prediction models to estimate the risk of clinical outcomes in individual patients.

Introduction

Peripheral arterial disease (PAD) may cause ischemia of the lower extremity and is associated with significant morbidity and mortality[1,2]. Symptomatic PAD leads to loss of function of the affected limbs, which manifests through significantly reduced walking distance and leads to a reduced quality of life and an increased rate of depression[3]. Additionally, PAD has been linked to an increased risk of coronary artery disease and vice versa, and overall mortality[1,2]. Furthermore, an estimated 5 to 21% of patients who are asymptomatic or present with intermittent claudication go on to develop chronic limb-threatening ischemia (CLTI) within five years[2]. CLTI has been associated with high rates of amputation, even in patients who successfully undergo revascularization, leading to significant disability and further increasing the mortality rate, which has been estimated to be as high as 50% within five years after amputation[1,2].

Identifying which patients are at risk of these far-reaching consequences remains challenging. Considering the rise in prevalence of PAD due to aging of the general population and the increasing collective burden of cardiovascular risk factors, particularly diabetes, there is a growing need for prognostic markers to identify high-risk patients. After all, early detection may provide opportunities for patient education, lifestyle interventions and vascular treatment strategies, thus averting or deferring adverse events such as amputation[1]. In an effort to improve risk stratification in PAD patients, several systems have been proposed over the last years. This includes the Society of Vascular Surgery Wound, Ischemia and foot Infection classification (SVS WIfI), which is used to grade limb severity, and the Global Limb Anatomic Staging System (GLASS), which scores the anatomic pattern of PAD[2]. While these classifications mark an effort towards evidence-based revascularization (EBR), there is only a limited role for calcification scoring within these risk stratification systems.

Contrarily, in symptomatic coronary artery patients, quantitative coronary artery calcium scores have been established as a robust predictor of adverse events, surpassing traditional cardiovascular risk factors, which has lead to its widespread application in risk stratification[4–6]. Furthermore, a similar association has been shown between aortic calcification and cardiovascular events and mortality in the general population[7]. Based on these findings, a similar relationship may be predicted to exist for peripheral artery calcification.

Therefore, the objective of this literature study is to review the available evidence on the association between peripheral arterial calcification, quantified by means of a calcium score, and clinical outcomes. First, the methods used to quantify calcifications in the peripheral arteries will be explored in this review. Secondly, the correlation between quantified calcification and the clinical presentation (severity of ischemia), peri-procedural outcomes (technical success) and late clinical outcomes such as major adverse limb events (MALE) and major adverse cardiovascular events (MACE), will be studied.

Methods

Search strategy

A systematic literature search was conducted in PubMed and Embase, from inception of the respective databases up until 7 June 2021. Keywords describing calcifications, scoring, the lower extremity, clinical outcomes and peripheral arterial disease were combined. The search was limited to articles written in English. The search string used for both databases can be found in Appendix A of this article. Additionally, the reference lists of included studies were searched manually for additional eligible articles, as described in the Preferred Reporting Items for Systematic Reviews and Meta-analyses (PRISMA) statement[8].

Study selection and quality assessment

Two authors (RW, *second reviewer to be determined*) independently screened records found in each database on title and abstract. The same two authors subsequently assessed relevant articles based on the full text to reach the final selection of included studies. Disagreements were resolved by discussion between the two reviewers; for disputable cases, a third author (CH) was consulted to reach consensus.

Articles were eligible if they (1) reported original data, (2) recruited symptomatic PAD patients, (3) quantified arterial calcification in a calcium score based on imaging and (4) compared clinical outcomes between patients with a range of quantitative or semiquantitative calcification assessments.

This study investigated the reported correlation of calcification with clinical presentation, periprocedural outcomes and late clinical outcomes. Severity of ischemia at clinical presentation was defined according to the system by Rutherford et al.[9] Periprocedural technical success was defined as successful crossing of the stenosis or occlusion to be treated and restoration of in-line flow with <30% residual stenosis after treatment. Late clinical outcome was defined by MALE, target lesion revascularization (TLR), primary patency, late lumen loss and MACE. MALE was defined as the composite of major (above-the-ankle) amputation and endovascular or surgical revascularization of the ipsilateral limb. Target lesion revascularization was defined as a secondary procedure performed for >50% restenosis of the target vessel combined with recurrent PAD symptoms. Primary patency was defined as the target vessel remaining patent after a specified period of follow-up without secondary intervention; the criteria by which primary patency was determined differed per included study and included peak systolic velocity ratio >2.4, lack of flow or >50% restenosis on duplex ultrasound, computed tomography (CT) or angiography or a >0.15 decrease in the resting ankle brachial index. Late lumen loss (LLL) was defined as the minimum lumen diameter (MLD) post-intervention minus the MLD after a defined period of follow-up. MACE was the composite of non-fatal myocardial infarction, non-fatal stroke and all-cause mortality (ACM).

Assessment of risk of bias was performed independently by two authors (RW, *second reviewer to be determined*) using the QUIPS tool, which was developed specifically for appraisal of prognostic factor studies[10]. In case of disagreement between the two authors, a third author (CH) was consulted to reach consensus.

Results

Search string results

The study selection process is visualized in Figure 1. The search strategy yielded 401 records in PubMed and 881 in Embase. Furthermore, four additional articles were identified at a later stage by manually searching the references of included articles. As such, 1286 records, including duplicates present in both databases, were screened on title and abstract. Of these, 1259 articles were found not to be relevant to the research question and were excluded. The full text of the remaining 28 articles was screened for eligibility. Eight studies did not meet the aforementioned inclusion criteria and were excluded, leaving 20 studies to be included in this review. The main characteristics of these studies are shown in Table 1. The risk of bias in each included study, assessed according to the QUIPS method, is reported in Table 2. All tables can be found in Appendix B of this article.

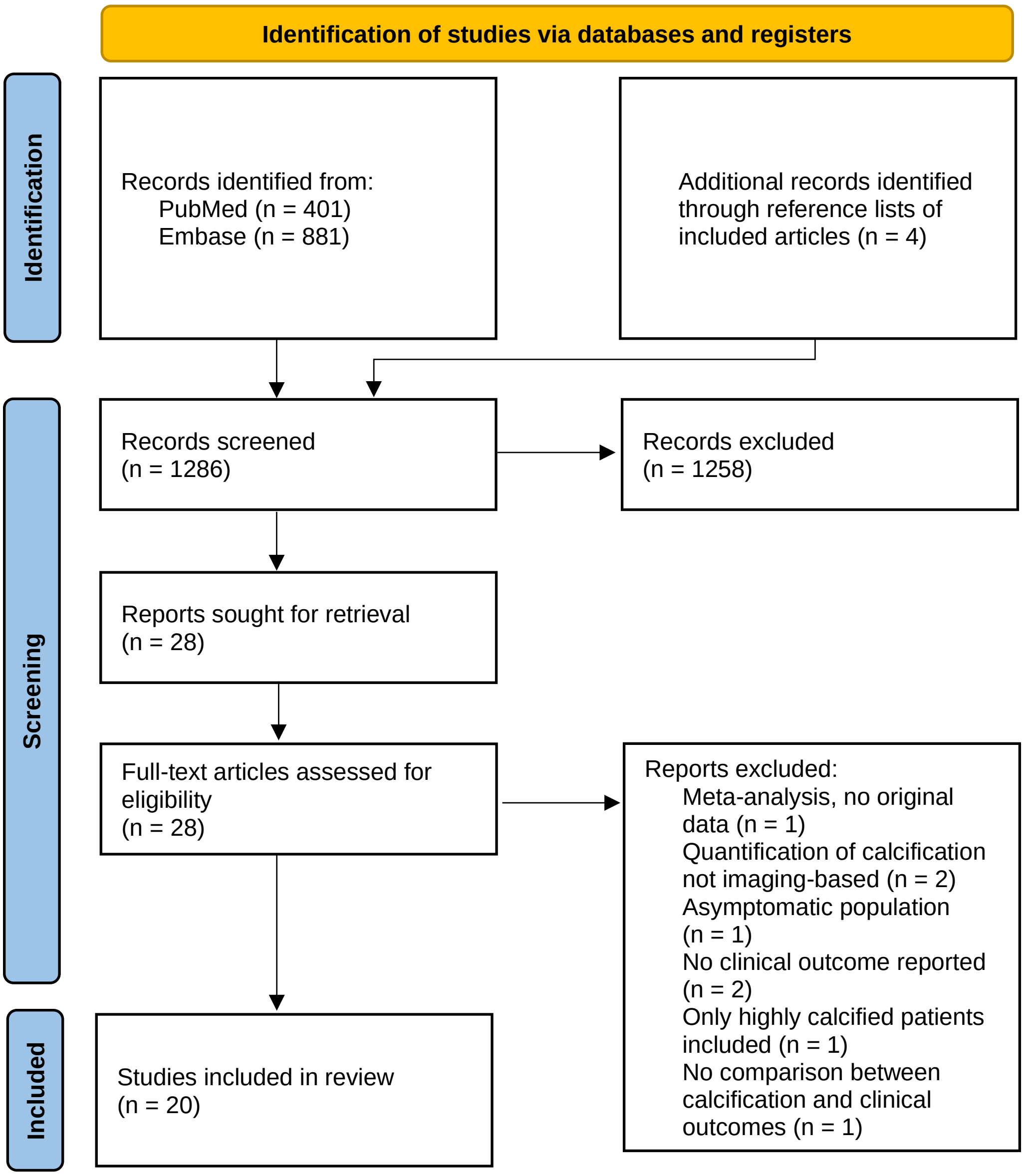

Figure 1: PRISMA flowchart describing the study selection process.[8]

Calcification scores

The different methods used to assess calcification in the included studies will be described in this section. Out of the 20 studies included in this review, seven studies used a quantitative scoring method solely, nine studies used a semiquantitative method solely, two studies used both a quantitative and a semiquantitative method and two studies assessed calcification as a dichotomous outcome.

Quantitative

Nine studies used a quantitative score, in which the total calcium burden was calculated for one or more arterial segments[11–19]. These quantitative calcium scores were calculated on non-contrast-enhanced computed tomography (CT) images based on the method described by Agatston et al., which was developed to quantify coronary artery calcification[4]. In this method, calcification is evaluated sequentially in every slice containing an artery of interest. Areas of calcification with a density >130

Hounsfield Units (HU) and a cross-sectional area >1 mm^2 are identified automatically. Kang et al. instead used a threshold of 250 HU since maximum intensity projections (MIP) of CT angiography (CTA) images were used in this study[15]. Next, regions of interest (ROI) corresponding to areas of calcification along the investigated arteries are selected and labelled manually. Subsequently, a lesion score is assigned to each ROI according to the highest density value in the ROI: 1 = 130-199, 2 = 200-299, 3 = 300-399 and 4 ≥ 400 HU, after which the score for each ROI is calculated by multiplying this lesion score with the area of the ROI. The scores are summed for every lesion in every slice to compute a segment score, which can then be summed with other segment scores into a total lower extremity score.[4]

The arterial segments for which a quantitative calcium score was calculated differed per study, as is shown in Table 1. Five studies reported that the distribution of the calculated calcium score was skewed and therefore used log-transformed values for the statistical analyses to normalize the distribution[11–13,15,19].

Semiquantitative

Of the eleven studies which used a semiquantitative score (9 solely, 2 both semi- and quantitative), four studies used the angiographic peripheral arterial calcium scoring system (PACSS)[16,20–22], one of which compared PACSS with another angiographic calcium score (ACS)[22]. Two studies graded medial arterial calcification (MAC) on foot radiography[23,24]. The remaining five studies each used different systems.

With PACSS, patients are assigned to one of five grades depending on the length and unilateral or bilateral presence of calcification, with grade 0 corresponding to no visible calcification, grade 1 to unilateral calcification with length < 5 cm, grade 2 to unilateral calcification with length > 5 cm, grade 3 to bilateral calcification < 5 cm and grade 4 to bilateral calcification with length ≥ 5 cm[25].

The ACS is similar to the PACSS in the sense that patients are assigned to grade 0-4 based on circumferentiality and length of calcifications. However, unlike PACSS, the cutoff for calcification length is 50% of the total lesion length instead of 5 cm[22].

Ferraresi et al. evaluated MAC at 5 vascular sites, as shown in Table 1, on laterolateral, anteroposterior and 45° oblique foot radiographic projections. One point was scored for each location containing 'rail-track' calcification – contiguous, bilateral calcification, resembling tram rails –with ≥1 cm or ≥2 cm length (depending on the location). The scores for every location were summed, yielding a 6-level scale from 0 to 5. For statistical analysis, patients were assigned to three groups: group 0 – no MAC (0-1 positive location), group 1 – moderate MAC (2-3 positive locations) and group 2 – severe MAC (4-5 positive locations).[23]

Skolnik et al. used a similar system, in which a severity score was assigned to calcification at each of 6 locations (shown in Table 1): absent (0 points), discontinuous and mild (1 point), continuous (2 points) or continuous with associated intimal calcification (3 points). The score for each of the 6 sites was added, yielding an 18-point MAC scale.[24]

Dake et al. also used a semiquantitative grading system, scoring calcification as 'none', 'mild/moderate' or 'severe' based on angiography or radiography. However, the method by which the calcium grades were determined was not reported, neither in the article itself nor in publications of the trials this post-hoc analysis was based on.[26]

Konijn et al. examined several characteristics of calcifications on CT: severity (categorized as absent, mild, moderate or severe), annularity (categorized as absent, dots, <90°, 90-270° or 270-360°), thickness (categorized as absent, <1.5 mm or ≥1.5 mm) and continuity (indistinguishable, irregular/patchy or continuous). However, the variables were converted into dichotomous variables for statistical analyses due to low patient counts in the less severe categories.[27]

Fanelli et al. have classified patients into eight groups (1a through 4b) based on the circumferentiality of calcifications on CTA and the length of calcifications on digital subtraction angiography. A grade for circumferentiality was assigned based on the presence of calcifications in one or multiple 90° sectors of the vessel wall: grade 1 (0-90°), grade 2 (0-180°), grade 3 (0-270°) and grade 4 (0-360°). Furthermore, patients were divided into two groups based on the length of calcifications: group A (<3 cm) and group B (>3 cm).[28]

Itoga et al. assessed the extent of calcifications in patients with occlusions by measuring the percentage of the vessel cross-sectional area occupied by calcifications on CTA.[29]

Aside from calculating a quantitative tibial artery calcification (TAC) score, Kang et al. also categorized patients into three TAC score groups, based on semiquantitative analysis of the CTA MIP images; patients were assigned to the 'minimal calcification' (MC) group if there was spotty calcification of the target tibial artery with a calcium mass ≤10 mm and the total extent of calcification comprised <10% of the target vessel; patients were scored as having 'extensive calcification' (EC) in the presence of linear calcification with a length >50 mm or diffuse calcification comprising >50% of the target vessel; patients in between these two categories were assigned to the 'intermediate calcification' (IC) group.[15]

Tokuda et al. also used both types of scores, comparing a quantitative score with the semiquantitative PACSS.[16]

Finally, two studies, which aimed to develop a prediction model using several patient and lesion characteristics, including age, DM, lesion length and lesion calcification, did not use a quantitative or semiquantitative measure of calcification. Instead, these studies used the presence or absence of calcium as a dichotomous variable. These studies did not clearly describe whether judgement of the presence of calcification was subjective or objective and which cutoff was used.[30,31]

Clinical presentation and periprocedural outcomes

Six studies have investigated the relationship between the level of calcification and the severity of ischemia at presentation; the results are shown in Table 3[12–15,18,19]. Significantly higher quantitative calcium scores were observed for groups with increasing severity of ischemia. This association was maintained on multivariate analysis in the two studies which conducted this analysis[12,13]. Additionally, Kang et al. observed significantly higher prevalence of Rutherford categories 5 and 6 in the semiquantitative EC and IC groups than in the MC group[15]. These results indicate a significant relationship between increasing calcification scores and more severe ischemia at clinical presentation.

Chang et al. investigated the relationship between the quantitative lower limb arterial calcification (LLAC) score and the occurrence of acute thrombosis in 201 patients presenting with symptomatic PAD. The LLAC score was found to be a significant predictor of lower acute thrombosis rate at presentation on multivariate analysis (OR 0.60; 95% CI [0.37 – 0.98]; p = 0.01).[11]

Four studies examined the association between calcification and technical success of endovascular treatment, the results of which are shown in Table 4[15,23,29,30]. All studies found a significant association between increasing calcification scores and lower technical success rates, which was largely maintained after correction for confounders on multivariate analysis. Kang et al. compared quantitative and semiquantitative TAC scores, using two multivariate models to avoid redundancy between these parameters. In this study, the semiquantitative TAC groups were significant, whereas the quantitative TAC score only showed a trend towards significance[15]. Furthermore, Itoga et al. found a significantly lower technical success with 100% vessel calcification, but only observed a trend towards significance for increasing percentage of vessel calcification[29].

Late clinical outcomes

Five studies assessed the association between calcification and MALE; the results are shown in Table 5[15,23,24,28,31]. Three studies have observed a significant association between calcification and MALE. Skolnik et al. included PAD patients with diabetic foot ulcer (DFU) and therefore stratified for SVS wound grade on multivariate analysis[24]. In this analysis, continuous MAC score was significantly associated with MALE for wound grade 1; however, at higher wound grades (not shown in Table 5), this association was no longer significant[24].

Six studies reported on the association between calcification and amputation rate (MALE related), the results of which are shown in Table 5[12,14–16,23,27]. Five studies observed a significant association between calcification and amputation. In the study of Ferraresi et al., this association was no longer significant after correction for confounders on multivariate analysis[23]. Kang et al. found a significant association for any amputation and unplanned amputation, but not for major amputation[15]. Finally, in the study by Konijn et al., only annularity of calcifications in the crural arteries was shown to be an independent predictor of amputation rate on multivariate analysis, whereas other parameters were not[27].

Six studies investigated the rate of TLR after initial endovascular treatment (Table 6)[15,16,21,23,26,28]. Three of these studies found a significant association between calcification and TLR. Ferraresi et al. additionally observed a significant association between MAC score and unscheduled podiatric surgical reintervention[23].

Five studies investigated the association between calcification and primary patency or late lumen loss (Table 6)[16,20–22,28]. All studies found a significant association between primary patency or late lumen loss and some measure of calcification, although not all calcium scores were significant.

Two studies studied the association between calcification and MACE or the related outcome of cardiac morbidity and mortality (CM/M) (Table 7); the results were not corrected for confounders on multivariate analysis.[15,17]

Finally, five studies investigated the relationship between calcification and ACM (Table 7)[14,16,17,21,27]. Four found a significant association; two of these studies performed multivariate analysis to correct for confounders. Konijn et al. found a significant association between ACM and calcification annularity, but not for calcification severity[27].

Discussion

The results of this review demonstrate the association between calcification and several clinical outcomes. Firstly, all studies investigating the relationship between the severity of ischemia at baseline and calcification found a significant, positive association. This result is not surprising, as the role of calcification in the pathogenesis of atherosclerosis is well-established and more extensive calcification has previously been associated with more significant stenosis of the coronary arteries[32]. The results of this review indicate a similar connection between peripheral artery calcification and the severity of PAD.

Interestingly, Chang et al. found that presentation with acute thrombosis was more likely in PAD patients with lower LLAC scores. This finding can be attributed to the observation that plaque calcification typically supports stability of the plaque. As such, patients with acute thrombosis secondary to plaque rupture are more likely to have limited calcification, while patients with more extensive calcification tend to exhibit chronic limb ischemia. Therefore, the patients with acute thrombosis studied by Chang et al. most likely represent a population distinct from those investigated in other studies in this review, explaining this result.[11]

This review also found a significant association between increasing calcium scores and a lower rate of technical success of endovascular intervention. All four studies investigating this outcome present significantly lower technical success rates with higher semiquantitative TAC groups, MAC score, 100% vessel calcification or dichotomous presence of calcification; quantitative TAC score and increasing percentage of vessel calcification indicate a trend.[15,23,29,30]
Severe – particularly circumferential – calcification has been reported to lead to difficult lesion crossing and incomplete stent expansion or suboptimal positioning [15,16,20,22,28]. Additionally, increased rates of stent fracturing, flow-limiting dissection and vessel recoil have been reported, as well as decreased penetration of paclitaxel with drug-eluting devices[15,16,20,22,28]. The decreased rate of technical success and significantly lower primary patency found in this review might be attributed to these effects.

With regard to MALE, its subindices of amputation rate and TLR, MACE and ACM, a clear trend towards significant association with increasing calcium scores was observed as well in this review. The increased risk of MACE and ACM observed are in line with previous studies showing a similar relationship between coronary and aortic calcification and cardiovascular morbidity and mortality[5,7]. Furthermore, the results of this review with regard to amputation rate reflect the results of a meta-analysis by Losurdo et al., who assessed the association between infrapopliteal MAC, either diagnosed directly with medical imaging or inferred indirectly from the ankle-brachial index, and lower limb amputations, in patients with diabetes or PAD[33]. In this meta-analysis, a significantly higher rate of amputation was found in patients with higher MAC indices, both in the complete cohort as well as on subanalysis for patients with PAD[33]. Aside from the study by Losurdo et al., this review presents, to the best of our knowledge, the first systematic review into the relationship between calcification and several clinical outcomes in patients with PAD.
Of course, this review and the included studies have several limitations as well. First, several of the included studies had relatively small sample sizes and short durations of follow-up, as can be appreciated from Table 1, which may have resulted in low event rates for rarer outcomes. This is reflected by the broad confidence intervals observed for amputation rate and ACM, even in studies which showed a significant association between more severe calcification and these outcomes. Secondly, there was considerable clinical heterogeneity between studies in terms of the patients included (as reflected by high risk of bias in the 'Study Participation' column in Table 2), arterial segments investigated and calcium scores used. Third, there are potential limitations to semiquantitative and dichotomous calcium scoring methods, which may not have been adequately validated. This is reflected by the column 'Prognostic Factor Measurement' in Table 2, which reveals high risk of bias. For instance, Konijn et al. collapsed their semiquantitative variables due to low incidence of the 'less severe' categories[27]. This may indicate that the semiquantitative scoring system used did not adequately describe the distribution of calcification parameters within the population of PAD patients. Additionally, several other studies did not describe the methods by which calcium scoring was performed, which makes it difficult to assess the validity of these calcium scores[26,30,31]; this may have contributed to the lack of a significant association between calcification and TLR in the study by Dake et al., for instance, despite the large series of patients investigated.
These limitations may have attributed to the lack of a significant association found by several studies for outcomes such as MALE, amputation rate and TLR. Unfortunately, the aforementioned clinical heterogeneity between studies precluded pooling of the data in the form of a meta-analysis to increase the statistical power for these outcomes. Finally, many results presented in this review were not corrected for confounders, as is reflected by the high risk of bias in the column 'Study Confounding' in Table 2. As such, while this review suggests a significant association between calcification scores and late clinical outcomes, these results should be interpreted with caution and further research should be conducted to confirm these associations.

While both quantitative and semiquantitative calcium scores were found to be significantly correlated with clinical outcomes, the aforementioned heterogeneity made direct comparison between results difficult and as such, no single calcium score stood out as superior. The study by Tokuda et al. was the only one to directly compare a quantitative and semiquantitative score within the same multivariate model[16]. In this study, the quantitative score maintained its predictive value, while the semiquantitative PACSS did not; this might indicate superior predictive for quantitative scores, although this cannot be concluded based on one study. On the other hand, several aspects of calcification incorporated in the semiquantitative scores, such as circumferentiality, were shown to be predictive of clinical outcomes as well. As such, the value of these different types of calcium scoring should be investigated further in future research. Development of a standardized peripheral arterial calcium score would facilitate comparison between research results, pooling of research data and application of calcium scoring into clinical practice. Therefore, this should be a focus for future research. Ideally, such a standardized calcium score would incorporate aspects of both quantitative and semiquantitative scores reported in this review.

Nevertheless, the results of this review underline the predictive value of calcium scoring in patients with PAD; it may help identify patients at high risk for adverse events, allowing targeted preventative measures, or guide towards other treatment strategies, such as bypass surgery or atherectomy, when successful endovascular treatment is unlikely. Therefore, imaging-based calcium scoring should be added to the 'three-dimensional' model for evidence-based revascularization proposed in the Global Vascular Guidelines, which includes the SVS WIfI and GLASS classifications. The results by Skolnik et al., who found that calcium scores predicted MALE in DFU patients at low wound grade, but not at higher wound grades, emphasize the additional value of each of these predictors, which may work in synergy within the heterogeneous PAD population[24]. Development of prediction models, such as those reported by Dake et al. and Qiu et al., may prove helpful in combining individual predictors and translating these into patient-tailored treatment strategies[26,30].

Conclusion

The results of this review show a convincing correlation between peripheral arterial calcification and the severity of ischemia at presentation, lower technical success, worse primary patency, an increased risk of TLR, amputation, MALE, MACE and all-cause mortality in patients with PAD. As a result, peripheral arterial calcium scoring may be useful for estimating the success of endovascular treatment and guiding treatment strategy. However, this association should be confirmed in more homogeneous PAD populations and larger follow-up studies. Further research is also needed to determine which calcium score is the best predictor of these clinical outcomes for a more precise estimation of the risk of these clinical outcomes in individual patients.

References

1 Walker CM, Bunch FT, Cavros NG, Dippel EJ. Multidisciplinary approach to the diagnosis and management of patients with peripheral arterial disease. *Clinical Interventions in Aging* 2015;**10**:1147–53. Doi: 10.2147/CIA.S79355.

2 Conte MS, Bradbury AW, Kolh P, White J v, Dick F, Fitridge R, et al. Global Vascular Guidelines on the Management of Chronic Limb-Threatening Ischemia. *European Journal of Vascular and Endovascular Surgery : The Official Journal of the European Society for Vascular Surgery* 2019;**58**(1S):S1-S109.e33. Doi: 10.1016/j.ejvs.2019.05.006.

3 Norgren L, Hiatt WR, Dormandy JA, Nehler MR, Harris KA, Fowkes FGR. Inter-Society Consensus for the Management of Peripheral Arterial Disease (TASC II). *Journal of Vascular Surgery* 2007;**45 Suppl S**:S5-67. Doi: 10.1016/j.jvs.2006.12.037.

4 Agatston AS, Janowitz WR, Hildner FJ, Zusmer NR, Viamonte M, Detrano R. Quantification of coronary artery calcium using ultrafast computed tomography. *Journal of the American College of Cardiology* 1990;**15**(4):827–32. Doi: https://doi.org/10.1016/0735-1097(90)90282-T.

5 Greenland P, Bonow RO, Brundage BH, Budoff MJ, Eisenberg MJ, Grundy SM, et al. ACCF/AHA 2007 Clinical Expert Consensus Document on Coronary Artery Calcium Scoring By Computed Tomography in Global Cardiovascular Risk Assessment and in Evaluation of Patients With Chest Pain: A Report of the American College of Cardiology Foundation Cl. *Journal of the American College of Cardiology* 2007;**49**(3):378–402. Doi: https://doi.org/10.1016/j.jacc.2006.10.001.

6 Adelhoefer S, Uddin SMI, Osei AD, Obisesan OH, Blaha MJ, Dzaye O. Coronary Artery Calcium Scoring: New Insights into Clinical Interpretation-Lessons from the CAC Consortium. *Radiology Cardiothoracic Imaging* 2020;**2**(6):e200281–e200281. Doi: 10.1148/ryct.2020200281.

7 Bastos Gonçalves F, Voûte MT, Hoeks SE, Chonchol MB, Boersma EE, Stolker RJ, et al. Calcification of the abdominal aorta as an independent predictor of cardiovascular events: a meta-analysis. *Heart (British Cardiac Society)* 2012;**98**(13):988–94. Doi: 10.1136/heartjnl-2011-301464.

8 Page MJ, McKenzie JE, Bossuyt PM, Boutron I, Hoffmann TC, Mulrow CD, et al. The PRISMA 2020 statement: an updated guideline for reporting systematic reviews. *BMJ* 2021;**372**:n71. Doi: 10.1136/bmj.n71.

9 Rutherford RB, Baker JD, Ernst C, Johnston KW, Porter JM, Ahn S, et al. Recommended standards for reports dealing with lower extremity ischemia: revised version. *Journal of Vascular Surgery* 1997;**26**(3):517–38. Doi: 10.1016/s0741-5214(97)70045-4.

10 Hayden JA, van der Windt DA, Cartwright JL, Côté P, Bombardier C. Assessing Bias in Studies of Prognostic Factors. *Annals of Internal Medicine* 2013;**158**(4):280–6. Doi: 10.7326/0003-4819-158-4-201302190-00009.

11 Chang Z, Yan H, Zhen Y, Zheng J, Liu Z. Lower Limb Arterial Calcification and Acute Thrombosis Risk in Patients with Peripheral Artery Disease. *Annals of Vascular Surgery* 2020;**63**:227–33. Doi: 10.1016/j.avsg.2019.06.043.

12 Guzman RJ, Brinkley DM, Schumacher PM, Donahue RMJ, Beavers H, Qin X. Tibial artery calcification as a marker of amputation risk in patients with peripheral arterial disease. *Journal of the American College of Cardiology* 2008;**51**(20):1967–74. Doi: 10.1016/j.jacc.2007.12.058.

13 Zettervall SL, Marshall AP, Fleser P, Guzman RJ. Association of arterial calcification with chronic limb ischemia in patients with peripheral artery disease. *Journal of Vascular Surgery* 2018;**67**(2):507–13. Doi: 10.1016/j.jvs.2017.06.086.

14 Huang C-L, Wu I-H, Wu Y-W, Hwang J-J, Wang S-S, Chen W-J, et al. Association of lower extremity arterial calcification with amputation and mortality in patients with symptomatic peripheral artery disease. *PloS One* 2014;**9**(2):e90201. Doi: 10.1371/journal.pone.0090201.

15 Kang IS, Lee W, Choi BW, Choi D, Hong M-K, Jang Y, et al. Semiquantitative assessment of tibial artery calcification by computed tomography angiography and its ability to predict infrapopliteal angioplasty outcomes. *Journal of Vascular Surgery* 2016;**64**(5):1335–43. Doi: 10.1016/j.jvs.2016.04.047.

16 Tokuda T, Oba Y, Koshida R, Suzuki Y, Murata A, Ito T. The Impact of Femoropopliteal Artery Calcium Score after Endovascular Treatment. *Annals of Vascular Surgery* 2020;**66**:543–53. Doi: 10.1016/j.avsg.2019.10.081.

17 Chowdhury MM, Makris GC, Tarkin JM, Joshi FR, Hayes PD, Rudd JHF, et al. Lower limb arterial calcification (LLAC) scores in patients with symptomatic peripheral arterial disease are associated with increased cardiac mortality and morbidity. *PloS One* 2017;**12**(9):e0182952. Doi: 10.1371/journal.pone.0182952.

18 Jeremias Z, Rat N, Benedek I, Rapolti E, Ratiu M, Muresan A, et al. High iliac calcium score is associated with increased severity and complexity of peripheral arterial disease and predicts global atherosclerotic burden. *Vasa - European Journal of Vascular Medicine* 2018;**47**(5):377–86. Doi: 10.1024/0301-1526/a000718.

19 Ohtake T, Oka M, Ikee R, Mochida Y, Ishioka K, Moriya H, et al. Impact of lower limbs' arterial calcification on the prevalence and severity of PAD in patients on hemodialysis. *Journal of Vascular Surgery* 2011;**53**(3):676–83. Doi: 10.1016/j.jvs.2010.09.070.

20 Ichihashi S, Shibata T, Fujimura N, Nagatomi S, Yamamoto H, Kyuragi R, et al. Vessel Calcification as a Risk Factor for In-Stent Restenosis in Complex Femoropopliteal Lesions After Zilver PTX Paclitaxel-Coated Stent Placement. *Journal of Endovascular Therapy : An Official Journal of the International Society of Endovascular Specialists* 2019;**26**(5):613–20. Doi: 10.1177/1526602819860124.

21 Okuno S, Iida O, Shiraki T, Fujita M, Masuda M, Okamoto S, et al. Impact of Calcification on Clinical Outcomes After Endovascular Therapy for Superficial Femoral Artery Disease: Assessment Using the Peripheral Artery Calcification Scoring System. *Journal of Endovascular Therapy : An Official Journal of the International Society of Endovascular Specialists* 2016;**23**(5):731–7. Doi: 10.1177/1526602816656612.

22 Tepe G, Beschorner U, Ruether C, Fischer I, Pfaffinger P, Noory E, et al. Drug-Eluting Balloon Therapy for Femoropopliteal Occlusive Disease: Predictors of Outcome With a Special Emphasis on Calcium. *Journal of Endovascular Therapy : An Official Journal of the International Society of Endovascular Specialists* 2015;**22**(5):727–33. Doi: 10.1177/1526602815600156.

23 Ferraresi R, Ucci A, Pizzuto A, Losurdo F, Caminiti M, Minnella D, et al. A Novel Scoring System for Small Artery Disease and Medial Arterial Calcification Is Strongly Associated With Major Adverse Limb Events in Patients With Chronic Limb-Threatening Ischemia. *Journal of Endovascular Therapy : An Official Journal of the International Society of Endovascular Specialists* 2021;**28**(2):194–207. Doi: 10.1177/1526602820966309.

24 Skolnik J, Weiss R, Meyr AJ, Dhanisetty R, Choi ET, Cunningham-Hill M, et al. Evaluating the Impact of Medial Arterial Calcification on Outcomes of Infrageniculate Endovascular Interventions for Treatment of Diabetic Foot Ulcers. *Vascular and Endovascular Surgery* 2021;**55**(4):382–8. Doi: 10.1177/1538574421993314.

25 Rocha-Singh KJ, Zeller T, Jaff MR. Peripheral arterial calcification: prevalence, mechanism, detection, and clinical implications. *Catheterization and Cardiovascular Interventions : Official Journal of the Society for Cardiac Angiography & Interventions* 2014;**83**(6):E212-20. Doi: 10.1002/ccd.25387.

26 Dake MD, Fanelli F, Lottes AE, O'Leary EE, Reichert H, Jiang X, et al. Prediction Model for Freedom from TLR from a Multi-study Analysis of Long-Term Results with the Zilver PTX Drug-Eluting Peripheral Stent. *Cardiovascular and Interventional Radiology* 2021;**44**(2):196–206. Doi: 10.1007/s00270-020-02648-6.

27 Konijn LCD, Takx RAP, de Jong PA, Spreen MI, Veger HTC, Mali WPTM, et al. Arterial calcification and long-term outcome in chronic limb-threatening ischemia patients. *European Journal of Radiology* 2020;**132**:109305. Doi: 10.1016/j.ejrad.2020.109305.

28 Fanelli F, Cannavale A, Gazzetti M, Lucatelli P, Wlderk A, Cirelli C, et al. Calcium burden assessment and impact on drug-eluting balloons in peripheral arterial disease. *Cardiovascular and Interventional Radiology* 2014;**37**(4):898–907. Doi: 10.1007/s00270-014-0904-3.

29 Itoga NK, Kim T, Sailer AM, Fleischmann D, Mell MW. Lower extremity computed tomography angiography can help predict technical success of endovascular revascularization in the superficial femoral and popliteal artery. *Journal of Vascular Surgery* 2017;**66**(3):835-843.e1. Doi: 10.1016/j.jvs.2017.02.031.

30 Qiu Y-H, Yu G-F, Zhou H-H, Xia H-W, Chen L, Chen H-T, et al. Determination of Risk Factors and Establishment of a Prediction Model for Immediate Technical Failure during Endovascular Treatment of Femoropopliteal Occlusive Disease. *Annals of Vascular Surgery* 2018;**48**:35–44. Doi: 10.1016/j.avsg.2017.09.024.

31 Iida O, Soga Y, Yamauchi Y, Hirano K, Kawasaki D, Tazaki J, et al. Anatomical predictors of major adverse limb events after infrapopliteal angioplasty for patients with critical limb ischaemia due to pure isolated infrapopliteal lesions. *European Journal of Vascular and Endovascular Surgery : The Official Journal of the European Society for Vascular Surgery* 2012;**44**(3):318–24. Doi: 10.1016/j.ejvs.2012.05.011.

32 Frink RJ, Achor RWP, Brown AL, Kincaid OW, Brandenburg RO. Significance of calcification of the coronary arteries. *The American Journal of Cardiology* 1970;**26**(3):241–7. Doi: https://doi.org/10.1016/0002-9149(70)90790-3.

33 Losurdo F, Ferraresi R, Ucci A, Zanetti A, Clerici G, Zambon A. Association of infrapopliteal medial arterial calcification with lower-limb amputations in high-risk patients: A systematic review and meta-analysis. *Vascular Medicine (London, England)* 2021;**26**(2):164–73. Doi: 10.1177/1358863X20979738.

Appendix 1-A – Search String

PubMed

((("microcalc*"[Title/Abstract] OR "calci*"[Title/Abstract] OR "Calcinosis"[MeSH Terms]) AND (("arterioscler*"[Title/Abstract] OR "Arteriosclerosis"[MeSH Terms:noexp] OR ("atheroscler*"[Title/Abstract] OR "peripheral arterial disease*"[Title/Abstract] OR "peripheral artery disease*"[Title/Abstract] OR "PAD"[Title/Abstract] OR "Atherosclerosis"[MeSH Terms])) AND ("Leg"[Title/Abstract] OR "Legs"[Title/Abstract] OR "lower extremit*"[Title/Abstract] OR "tibia*"[Title/Abstract] OR "femora*"[Title/Abstract] OR "poplitea*"[Title/Abstract] OR "Lower Extremity"[MeSH Terms] OR "lower limb"[Title/Abstract] OR "iliac"[Title/Abstract] OR "peronea*"[Title/Abstract] OR "crural"[Title/Abstract] OR "pedal"[Title/Abstract] OR "infragenicula*"[Title/Abstract] OR "infra genicula*"[Title/Abstract] OR "infrapoplitea*"[Title/Abstract] OR "infra poplitea*"[Title/Abstract] OR "below the knee"[Title/Abstract] OR "below knee"[Title/Abstract] OR "infrainguinal"[Title/Abstract] OR "infra-inguinal"[Title/Abstract] OR ("aort*"[Title/Abstract] AND "abdominal"[Title/Abstract])) AND ("embolectom*"[Title/Abstract] OR "Embolectomy"[MeSH Terms] OR "thrombectom*"[Title/Abstract] OR "Thrombectomy"[MeSH Terms] OR "Limb Salvage"[Title/Abstract] OR "Limb Salvage"[MeSH Terms] OR "angioplast*"[Title/Abstract] OR "Angioplasty"[MeSH Terms] OR "major adverse limb event*"[Title/Abstract] OR "amputat*"[Title/Abstract] OR "death"[Title/Abstract] OR "limb ischemia"[Title/Abstract] OR "limb ischaemia"[Title/Abstract] OR "interven*"[Title/Abstract] OR "cardiac event*"[Title/Abstract] OR "cardiovascular event*"[Title/Abstract] OR "major adverse event*"[Title/Abstract] OR "mortalit*"[Title/Abstract] OR "prognos*"[Title/Abstract] OR "predict*"[Title/Abstract] OR "patency"[Title/Abstract]) AND ("scor*"[Title/Abstract] OR "calculat*"[Title/Abstract] OR "measur*"[Title/Abstract] OR "model*"[Title/Abstract])) AND ("dutch"[Language] OR "english"[Language])))

Embase

((microcalc*:ti,ab,kw OR calci*:ti,ab,kw OR 'blood vessel calcification'/exp OR 'blood vessel calcification') AND (scor*:ti,ab,kw OR calculat*:ti,ab,kw OR measur*:ti,ab,kw OR model*:ti,ab,kw) AND (atheroscler*:ti,ab,kw OR 'peripheral arterial disease*':ti,ab,kw OR 'peripheral artery disease*':ti,ab,kw OR 'pad':ti,ab,kw OR 'peripheral occlusive artery disease'/exp OR 'arteriosclerosis'/de OR 'atherosclerosis'/de OR 'aortic atherosclerosis'/exp) AND (leg:ti,ab,kw OR legs:ti,ab,kw OR 'lower extremit*':ti,ab,kw OR 'lower limb':ti,ab,kw OR tibia*:ti,ab,kw OR femora*:ti,ab,kw OR poplitea*:ti,ab,kw OR iliac:ti,ab,kw OR peronea*:ti,ab,kw OR pedal:ti,ab,kw OR infragenicula*:ti,ab,kw OR 'infra-genicula*':ti,ab,kw OR infrapoplitea*:ti,ab,kw OR 'infra-poplitea*':ti,ab,kw OR 'below the knee':ti,ab,kw OR 'below knee':ti,ab,kw OR infrainguinal:ti,ab,kw OR 'infra-inguinal':ti,ab,kw OR (aort*:ti,ab,kw AND abdominal:ti,ab,kw) OR 'leg artery'/exp OR 'leg artery' OR 'abdominal aorta'/de OR 'leg blood vessel'/exp) AND (embolectom*:ti,ab,kw OR thrombectom*:ti,ab,kw OR 'limb salvage':ti,ab,kw OR angioplast*:ti,ab,kw OR amputat*:ti,ab,kw OR death:ti,ab,kw OR mortalit*:ti,ab,kw OR 'limb ischemia':ti,ab,kw OR 'limb ischaemia':ti,ab,kw OR interven*:ti,ab,kw OR 'cardiac event*':ti,ab,kw OR 'cardiovascular event*':ti,ab,kw OR 'major adverse event*':ti,ab,kw OR 'major adverse limb event*':ti,ab,kw OR prognos*:ti,ab,kw OR predict*:ti,ab,kw OR patency:ti,ab,kw OR 'thrombectomy'/exp OR 'embolectomy'/exp OR 'limb salvage'/exp OR 'revascularization'/exp OR 'endarterectomy'/de OR 'angioplasty'/exp OR 'endovascular surgery'/de OR 'leg amputation'/exp OR 'foot amputation'/de) AND ([embase]/lim))

Appendix 1-B – Tables

Table 1: Characteristics of the studies included in this review.

Study	Year	N*	Population	Rutherford category§	Regions of interest (target arteries)	Imaging modality	Calcium score	Follow-up (months¶)	Outcomes
Quantitative scores									
Chang[11]	2020	201	PAD patients	1-6	Aortoiliac, femoropopliteal, below-knee	CT	LLAC	-	Acute thrombosis
Guzman[12]	2008	118†	PAD patients	1-5, 0	Tibial arteries	CT	TAC	mean 13.8 ± 7.7	Ischemia severity, amputation rate
Zettervall[13]	2018	116	PAD patients	1-6	Superficial femoral, popliteal, anterior tibial, posterior tibial, peroneal	CT	PAC	-	Ischemia severity
Jeremias[18]	2018	84	PAD patients	1-6	Iliac arteries	CT	ICS	-	Ischemia severity
Ohtake[19]	2011	46†	Hemodialysis patients with PAD	1-6	Superficial femoral, below-knee	CT	SFACS, BKACS	-	Ischemia severity
Huang[14]	2014	82	PAD patients	1-6	Iliac-femoral, above-knee, below-knee	CT	CS	mean 21 ± 11	Amputation rate, ACM
Chowdhury[17]	2017	220	PAD patients	*Not explicitly reported*	Aorto-iliac, femoropopliteal, crural	CT	LLAC	median 46 (IQR 31 - 64)	CM/M, ACM
Semiquantitative scores									

Ichihashi[20]	2019	230	PAD patients undergoing Zilver® PTX™ DES treatment	1-6	Femoropopliteal	Angiography	PACSS	median 19 (IQR 1.1 - 70.9)	ISR, TLR
Okuno[21]	2016	394	PAD patients undergoing EVT	2-3	Superficial femoral	Angiography	PACSS	mean 26 ± 15	2-year primary patency, 2-year amputation rate
Tepe[22]	2015	90	FPOD patients, including stenosis and occlusion, undergoing DEB treatment	1-5	Superficial femoral artery, popliteal artery	Angiography	PACSS, ACS	mean 6 ± 1	LLL after 6 months
Ferraresi[23]	2021	259	CLTI patients	5-6	Dorsalis pedis, lateral plantar, first metatarsal, first digital artery, other digital arteries	Foot radiography	MAC	mean 19 ± 10.8	Unscheduled podiatric surgical reintervention, redo revascularization, amputation rate, MALE, survival
Skolnik[24]	2021	99	PAD patients with DFU undergoing infrageniculate EVT	5-6	Anterior tibial, posterior tibial, dorsalis pedis, plantar, metatarsal, digital arteries	Foot radiography	MAC	not *reported*	1-year MALE rate
Dake[26]	2021	2227‡	PAD patients undergoing Zilver® PTX™ DES treatment	1-6	Femoropopliteal	Angiography (3 studies), X-ray (4 studies)	Semiquantitative	median 23.9 (range 0.03 - 60.8)	ffTLR

Konijn[27]	2020	87	CLI patients	4-6	Femoropopliteal, crural	CT	Multiple aspects	7 years (amputation), 10 years (mortality)	Amputation rate, ACM
Fanelli[28]	2014	60	PAD patients with a SFA stenosis, undergoing DEB treatment	2-4	Superficial femoral artery	CTA, DSA	Calcium circumferentiality and length	12	LLL, TLR, primary and secondary patency, MAE, Rutherford shift
Itoga[29]	2017	74	Patients undergoing EVT for occlusion in the SFA-pop region	1-6	Superficial femoral artery, popliteal artery	CTA	Percentage of vessel calcification	median 15.8 (IQR 8.6 - 27.8)	Technical success, primary and cumulative patency (at 6 months and 1 year)
<u>Both types of scores</u>									
Kang[15]	2016	124	CLI patients undergoing angioplasty for tibial artery lesions	4-6	Anterior tibial, posterior tibial, peroneal	CTA (MIP)	TAC (quantitative, semiquantitative)	mean 25.5 ± 13.4	Technical success, MALE, amputation rate, target lesion revascularization, MACE
Tokuda[16]	2020	132	PAD patients undergoing EVT for femoropopliteal stenosis	2-6	Femoropopliteal	CT, angiography	CS (quantitative), PACSS (semiquantitative)	mean 816 ± 656 days	1-year primary patency, CD-TLR, major amputation, ACM
<u>Dichotomous scores</u>									
Qiu[30]	2018	1563	FPOD patients, including stenosis and occlusion, undergoing EVT	3-6	Femoropopliteal	CTA	Dichotomous	-	Immediate technical failure

Iida[31]	2012	1058	CLI patients undergoing angioplasty for isolated infrapopliteal lesion	4-6	Crural arteries	Angiography	Dichotomous	mean 18 ± 15	2-year freedom from MALE

Abbreviations: PAD, peripheral artery disease; CLI, critical limb ischemia; EVT, endovascular treatment; DES, drug-eluting stent; DEB, drug-eluting balloon; FPOD, femoropopliteal occlusive disease; CLTI, chronic limb-threatening ischemia; DFU, diabetic foot ulcer; SFA, superficial femoral artery; SFA-pop, superficial femoral artery – popliteal artery; CT, computed tomography; CTA, computed tomography angiography; MIP, maximum intensity projection; DSA, digital subtraction angiography; LLAC, lower limb arterial calcificiation; TAC, tibial artery calcification; PAC, peripheral artery calcification; ICS, iliac calcium score; SFACS, superior femoral artery calcium score; BKACS, below knee artery calcium score; CS, calcium score; PACSS, peripheral arterial calcium scoring system; ACS, angiographic calcium score; MAC, medial arterial calcification; IQR, interquartile range; ACM, all-cause mortality; MALE, major adverse limb events; MACE, major adverse cardiovascular events; CD-TLR, clinically-driven target lesion revascularization; CM/M, cardiac morbidity and mortality; ISR, in-stent restenosis; TLR, target lesion revascularization; LLL, late lumen loss; MAE, major adverse events; ffTLR, freedom from target lesion revascularization.

* 'N' reflects the number of lesions/occlusions, limbs or patients analyzed, depending on the study.

† This study also included participants without PAD; the data for these participants was not included in this review.

‡ Post hoc analysis of five clinical trials.

§ The Rutherford category reflects the severity of ischemia at baseline in included patients[9].

¶ Unless specified otherwise.

Table 2: Evaluation of risk of bias for each of the included studies according to the QUIPS method[10]. Cochrane RevMan 5.4.1 was used to generate this table.

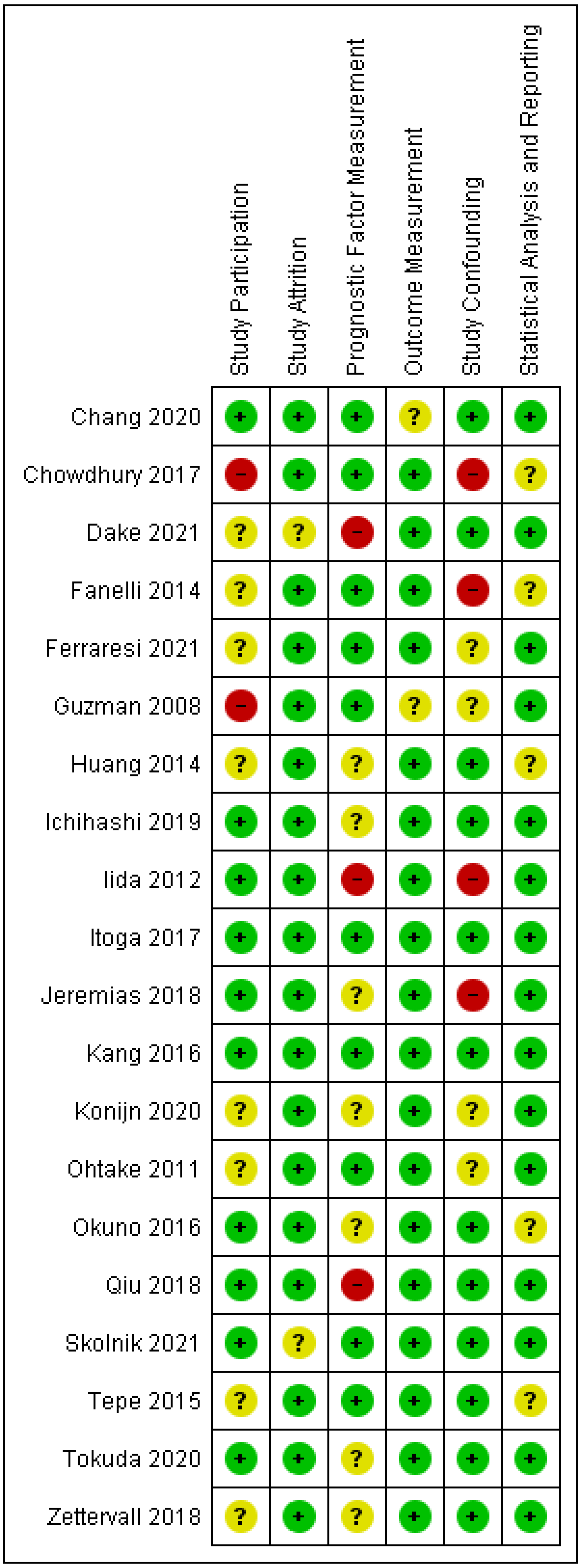

	Study Participation	Study Attrition	Prognostic Factor Measurement	Outcome Measurement	Study Confounding	Statistical Analysis and Reporting
Chang 2020	+	+	+	?	+	+
Chowdhury 2017	−	+	+	+	−	?
Dake 2021	?	?	−	+	+	+
Fanelli 2014	?	+	+	+	−	?
Ferraresi 2021	?	+	+	+	?	+
Guzman 2008	−	+	+	?	?	+
Huang 2014	?	+	?	+	+	?
Ichihashi 2019	+	+	?	+	+	+
Iida 2012	+	+	−	+	−	+
Itoga 2017	+	+	+	+	+	+
Jeremias 2018	+	+	?	+	−	+
Kang 2016	+	+	+	+	+	+
Konijn 2020	?	+	?	+	?	+
Ohtake 2011	?	+	+	+	?	+
Okuno 2016	+	+	?	+	+	?
Qiu 2018	+	+	−	+	+	+
Skolnik 2021	+	?	+	+	+	+
Tepe 2015	?	+	+	+	+	?
Tokuda 2020	+	+	?	+	+	+
Zettervall 2018	?	+	?	+	+	+

Table 3: Association between calcification scores and severity of ischemia at baseline reported by included studies, per method of calcium scoring.

			Statistical hypothesis testing			**Multivariate Cox regression analysis**	
Calcification score	**Study**	**N**	**Variable**	**Comparison**	**p-value**	**Estimator (95% CI)**	**p-value**
Quantitative	Guzman	229	TAC score*	CLI vs. CI	**<.01**	**HR 2.548 (1.945-3.340)**	**<.0001**
	Zettervall	116	PAC score	CLI vs. CI	**<.001**	**OR 1.9 (1.3 – 2.8)**	**.001**
	Huang	88	CS	Fontaine III vs. II	.44	*Not reported*	
				Fontaine IV vs. II	**.02**		
				trend	**.03**		
	Jeremias	84	ICS	Rutherford 1-2 vs. 3-4	**.2**	*Not reported*	
				Rutherford 3-4 vs. 5-6	**.5**		
				Rutherford 1-2 vs. 5-6	**.03**		
	Ohtake	46	SFACS*	Fontaine IV vs. I	**<.001**		
			BKACS*	Fontaine IV vs. I	**<.001**		
Semiquantitative	Kang	124	Rutherford category (4-6)	EC vs. IC vs. MC† (*trend*)	**.001**	*Not reported*	

Abbrevations: N, number of subjects; TAC, tibial artery calcification; PAC, peripheral artery calcification; CS, calcium score; CI, intermittent claudication; CLI, critical limb ischemia; EC, extensive calcification; IC, intermediate calcification; MC, minimal calcification; HR, hazard ratio; OR, odds ratio.

* Comparisons for patients vs. controls without PAD were omitted.

† Semiquantitative, categorized groups of TAC severity.

Table 4: Association between calcification scores and technical success of intervention reported by included studies, per method of calcium scoring.

				Statistical hypothesis testing			**Multivariate Cox regression analysis**		
Calcification score	**Study**	**N**	**Intervention**	**Variable/outcome**	**Comparison**	**p-value**	**Variable**	**Estimator (95% CI)**	**p-value**
Quantitative	Kang	124	Infrapopliteal EVT	Technical success	*Not reported*		2nd tertile of TAC score	HR 0.33 (0.03 – 3.67)	.37
							3rd tertile of TAC score	HR 0.07 (0.01 – 1.12)	.06
Semiquantitative	Kang	124	Infrapopliteal EVT	Technical success	EC vs. IC and MC*	**.001**	IC	HR 0.43 (0.03 – 6.43)	.543
							EC	**HR 0.02 (0.00 – 0.45)**	**.014**
	Ferraresi	246	EVT (92.7%), surgical (2.3%)	Successful revascularization	MAC groups 2 and 1 vs. group 0	**.017**	*Not reported*		
	Itoga	74	EVT for SFA-pop occlusions	Percentage of vessel calcification	Technical failure vs. success	.059	*Not reported*		
				100% vessel calcification	“	**.014**	**OR 9.0 (1.8 – 45.8)**		**.008**
Dichotomous	Qiu	1,563	Suprageniculate EVT	Lesion calcification	Technical failure vs. success	**<.001**	**OR 3.113 (1.882 – 5.150)**		**<.001**

Abbreviations: N, number of subjects; EVT, endovascular treatment; SFA-pop, superficial femoral or popliteal artery; EC, extensive calcification; IC, intermediate calcification; MC, minimal calcification; MAC, medial arterial calcification; TAC, tibial artery calcification; CI, confidence interval; HR, hazard ratio; OR, odds ratio.

* Semiquantitative, categorized groups of TAC severity.

Table 5: Association between calcification scores and MALE or amputation rate reported by included studies, per method of calcium scoring.

				Statistical hypothesis testing		**Multivariate Cox regression analysis**		
Calcification score	**Study**	**N**	**Outcome**	**Comparison**	**p-value**	**Predictor**	**Estimator (95% CI)**	**p-value**
MALE								
Semiquantitative	Ferraresi	259	MALE	MAC Group 1 vs. 0	**.007**	MAC group 1	**OR 1.87 (1.14 – 3.09)**	**.014**
				MAC Group 2 vs. 0	**.001**	MAC group 2	**OR 2.23 (1.33 – 3.74)**	**.002**
	Kang	124	MALE	EC vs IC vs MC* (*trend*)	.862	*Not reported*		
	Fanelli	60	MAE†	Group 1a through 4b (*trend)*	>.05	*Not reported*		
	Skolnik	99	MALE	*Not reported*		Continuous MAC score‡	**HR 1.16§**	**.032**
						2nd tertile of MAC score	HR 2.99	.136
						3rd tertile of MAC score	HR 2.59	.108
Dichotomous	Iida	1 058	MALE	Calcification + vs. –	**<.01**	Lesion calcification	**HR 1.38 (1.12 – 1.69)**	**.005**
Amputation rate								
Quantitative	Guzman	229	Major amputation	TAC > 400 vs. TAC < 400	**.0009**	TAC > 400	**HR 11.27 (1.353 – 93.842)**	**.025**
	Huang	82	Amputation	High vs. low CS groups	**.02**	2nd CS quartile	HR 4.32 (0.73 – 25.49)	.11
						3rd CS quartile	HR 4.69 (0.67 – 32.55)	.12
						4th CS quartile	**HR 12.25 (1.75 – 85.61)**	**.01**
						trend		**.01**
	Tokuda	132	Major amputation	High vs. low fem-pop CS groups	.86	*Not reported*		
	Kang	124	Unplanned amputation	*Not reported*		2nd tertile of TAC score	HR 2.04 (0.48 – 8.66)	.334
						3rd tertile of TAC score	**HR 7.39 (1.92 – 28.53)**	**.004**

Semiquantitative	Kang	124	Major amputation	EC vs. IC vs. MC* (*trend*)	.076	*Not reported*		
			Any amputation	“	**<.001**	*Not reported*		
			Unplanned amputation	“	**<.001**	IC	**HR 5.73 (1.15 – 28.54)**	**.033**
						EC	**HR 9.90 (2.05 – 47.75)**	**.004**
	Ferraresi	259	Major amputation	MAC Group 1 vs. 0	**.031**	MAC group 1	OR 3.03 (0.86 – 10.63)	.08
				MAC Group 2 vs. 0	**.007**	MAC group 2	OR 2.68 (0.75 – 9.65)	.13
	Konijn	87	Amputation	*Not reported*		Severity – fem-pop	HR 0.78 (0.34 – 1.77)	.50
						Severity – crural	HR 1.00 (0.47 – 2.15)	.99
						Annularity – fem-pop	HR 1.54 (0.88 – 2.71)	.13
						Annularity – crural	**HR 1.96 (1.05 – 3.65)**	**.03**

Abbreviations: N, number of subjects; MALE, major adverse limb events; MAE, major adverse events; MAC, medial arterial calcification; EC, extensive calcification; IC, intermediate calcification; MC, minimal calcification; TAC, tibial artery calcification; CS, calcium score; CI, confidence interval; HR, hazard ratio; OR, odds ratio.

* Semiquantitative, categorized groups of TAC severity.

† MAE was defined as the composite of thrombosis, amputation, TLR and mortality.

‡ Skolnik et al. performed multivariate analysis stratified by SVS wound grade, with separate models for both measures of MAC (continuous MAC score and MAC tertiles). The results for the wound grade 1 stratum are shown; no measure of MAC was significantly associated with MALE for wound grade 2 or 3[24].

§ No confidence intervals were reported for the hazard ratios obtained on multivariate analysis[24].

Table 6: Association between calcification scores and TLR or primary patency reported by included studies, per method of calcium scoring.

				Statistical hypothesis testing		**Cox regression analysis†**		
Calcification score	**Study**	**N**	**Outcome**	**Comparison**	**p-value**	**Predictor**	**Estimator (95% CI)**	**p-value**
TLR								
Quantitative	Tokuda	132	CD-TLR	High vs. low fem-pop CS groups	**<.01**	CS (per 100 increase)	**HR 1.05 (1.02 – 1.08)**	**<.01**
Semiquantitative	Tokuda	132	CD-TLR	*Not reported*		PACSS 4	HR 1.06 (0.33 – 3.36)	.92
	Ferraresi	259	Redo revascularization	MAC group 1 vs. 0	**.001**	MAC group 1	**OR 2.78 (1.47 – 5.25)**	**.002**
				MAC group 2 vs. 0	**.001**	MAC group 2	**OR 2.57 (1.33 – 4.97)**	**.005**
			Unscheduled podiatric surgical reintervention	MAC group 2 vs. 0	**.001**	MAC group 1	OR 1.82 (0.93 – 3.53)	.07
				MAC group 2 vs. 1	**.013**	MAC group 2	**OR 2.96 (1.53 – 5.73)**	**.001**
	Okuno	394	CD-TLR	PACSS 4 vs. 0	**.048**	*Not reported*		
	Kang	124	(CD-)TLR	EC vs IC vs MC* (*trend)*	.632	*Not reported*		
	Fanelli	60	(CD-)TLR	Group 1a through 4b (*trend)*	>.05	*Not reported*		
	Dake	2 227	CD-TLR	No vs. mild/moderate vs. severe calcification	.752	*Not reported*		
Primary patency								
Quantitative	Tokuda	132	Primary patency (1 year)	High vs. low fem-pop CS groups	**<.01**	*Not reported*		
Semiquantitative	Okuno	394	Primary patency (2 years)	Bilateral vs. unilateral calcification	**<.001**	PACSS 4	**HR 2.74 (1.56 – 4.83)**	**<.001**

				Long vs. short calcification	.140	Bilateral calcification (PACSS 3/4)	**HR 2.23 (1.49 – 3.34)**	**<.001**
						Long calcification (PACSS (2/4)	*Not reported*	.201
	Tepe	90	Late lumen loss (6 months)	ACS - Severe or moderately severe vs. mild, moderate or none	**.014**	ACS – Severe or moderately severe vs. mild/moderate or none	**HR 1.772 (1.113 – 2.822)**	**.016**
				PACSS – Bilateral vs. unilateral or none	.072	PACSS 3 or 4 (bilateral)	HR 1.710 (0.986 – 2.967) ‡	.056
				PACSS – Long vs. short or none	.256			
	Ichihashi	220	Primary patency (1, 2 and 5 years)	PACSS 3/4 vs. PACSS 0/1/2	**.020**	PACSS 3 or 4	**HR 1.718 (1.035 – 2.851)**	**.036**
	Fanelli	60	Late lumen loss (1 year)	Group 1a through 4b (*trend*)	.05	*Not reported*		
			Primary patency (1 year)	Group 1a through 4b (*trend*)	**<.05**	*Not reported*		

Abbreviations: N, number of subjects; CD-TLR, clinically-driven target lesion revascularization; CS, calcium score; MAC, medial arterial calcification; ACS, angiographic calcium score; PACSS, peripheral arterial calcium scoring system; CI, confidence interval; HR, hazard ratio; OR, odds ratio.

* Semiquantitative, categorized groups of TAC severity.

† Results of multivariate Cox regression analysis are shown, unless specified otherwise.

‡ The results of univariate Cox regression analysis are shown, as results of multivariate analysis were not provided for this outcome[22].

Table 7: Association between calcification scores and MACE or ACM reported by included studies, per method of calcium scoring.

				Statistical hypothesis testing		**Multivariate Cox regression analysis**		
Calcification score	**Study**	**N**	**Outcome**	**Comparison**	**p-value**	**Predictor**	**Estimator (95% CI)**	**p-value**
Quantitative	Chowdhury	220	CM/M*	Increasing LLAC quartiles (*trend)*	**<.001**	*Not reported*		
			ACM	Increasing LLAC quartiles (*trend)*	**.012**	*Not reported*		
	Huang	82	ACM	High vs. low CS group	**.01**	2nd CS quartile vs. 1st	HR 5.23 (0.43 – 63.11)	.19
						3rd CS quartile vs. 1st	**HR 14.36 (1.24 – 164.60)**	**.03**
						4th CS quartile vs. 1st	**HR 10.29 (0.85 – 124.71)**	**.07**
						trend		**.046**
	Tokuda	132	ACM (1 year)	High vs. low fem-pop CS group	.12	*Not reported*		
Semiquantitative	Kang	124	MACE (2 years)	EC vs IC vs MC† (*trend*)	**.028**	*Not reported*		
	Okuno	394	ACM (2 years)	PACSS 4 vs. 0	**.011**	*Not reported*		
	Konijn	87	ACM (10 years)	*Not reported*		Severity – fem-pop	HR 2.03 (0.79 – 5.13)	.14
						Severity – crural	HR 1.55 (0.71 – 3.35)	.26
						Annularity – fem-pop	**HR 1.68 (1.01 – 2.80)**	**.04**
						Annularity – crural	**HR 2.29 (1.28 – 4.13)**	**.006**

Abbreviations: N, number of subjects; CM/M, cardiac morbidity and mortality; MACE, major adverse cardiovascular events; ACM, all-cause mortality; LLAC, lower limb arterial calcification; CS, calcium score; EC, extensive calcification; IC, intermediate calcification; MC, minimal calcification; PACSS, peripheral arterial calcium scoring system; CI, confidence interval; HR, hazard ratio; OR, odds ratio.

* CM/M was defined as the composite of either death or hospitalization with evidence of a coronary event.

† Semiquantitative, categorized groups of TAC severity.

Chapter 2 – Validation of dual-energy CT imaging

Current calcification scoring methods – limitations

The results of the systematic review reported in the previous chapter suggest an association between increasing peripheral arterial calcification scores and the severity of clinical presentation, periprocedural outcomes and late clinical outcomes. However, there were several limitations to the methods of the included studies.

First of all, the studies included in the systematic review used various imaging modalities to visualize and score the extent of calcification, with most studies using non-contrast CT or angiography. However, both the Dutch and European guidelines for PAD recommend CTA or magnetic resonance angiography for non-invasive visualization of the extent of stenotic disease, with CTA providing superior visualization of calcifications [19,20]. The addition of a non-contrast CT scan, which is currently not routinely made in PAD patients, to the scanning protocol would expose patients to higher doses of radiation, which is in conflict with the ALARA ("as low as reasonably achievable") principle of radiation hygiene. A study by Hong et al. demonstrated the carcinogenic effect of CT imaging in 12 million youths, with an incidence rate ratio for malignancy of 1.54 [95% CI, 1.45-1.63; $p < 0.001$] in the exposed group [21]. Naturally, the risk of stochastic effects associated with the additional non-contrast CT scan would be lower in the predominantly elderly PAD population and one might argue the potential morbidity and mortality due to PAD outweigh these risks. Nevertheless, the addition of a non-contrast scan to the protocol would lead to a large number of additional CT scans in light of the high prevalence of PAD [6] and therefore some stochastic effects might be expected despite a low individual risk. Consequently, it would be preferable if the extent of calcification could be scored on CTA scans. CTA has been found to have good diagnostic accuracy in visualizing (the absence of) stenoses and occlusions in PAD patients when compared with the reference standard, digital subtraction angiography (DSA) [2,22]. However, potential limitations to this imaging modality have been reported with regard to calcium scoring [2,22]. For instance, the visualization of calcifications may be subject to blooming or partial volume artifacts, leading to over- or underestimation of the size of calcium deposits [22–25]. Furthermore, similarity in Hounsfield Units between calcifications and the iodine contrast agent may impede discrimination between these materials, especially if automatic calcium identification methods are considered [26,27]. This may, in turn, prevent accurate detection and measurement of calcifications [26,27]; Mühlenbruch et al. found that quantitative coronary calcium scores were erroneously increased on contrast-enhanced CT series [27]. Furthermore, several studies found that increasing the threshold to >350 HU to compensate for this effect may lead to underestimation of the calcification burden [26,27]. Dual-energy CT (DECT), in which two image sets are made using high- and low-energy X-rays respectively, may be a promising solution to this problem [28–30]. DECT imaging operates on the principle that different materials attenuate X-rays photons of different energies at different rates, which allows for materials to be differentiated based on their unique attenuation profile [28–30]. As such, dual energy CT angiography (DECTA) may be used to separate calcifications and the iodine contrast agent [28–30]. This allows for the generation of a virtual non-contrast scan, facilitating detection of calcification and the calculation of various quantitative and semiquantitative calcium scores, as described in Chapter 1, thus eliminating the need for a standard non-contrast CT scan [31]. Calcium scoring based on virtual non-contrast scans has previously been shown to be feasible for the coronary arteries [32,33].

Secondly, there are limitations to the quantitative calcium scoring method according to Agatston et al. which was used by nine studies included in the review [14]. As Demer et al. point out, the Agatston method contains three processing steps which decrease the robustness and reproducibility of the algorithm [34]. First, the voxel values (in Hounsfield units) are truncated, with only the first number remaining as the value for each voxel; this introduces random noise as 0 to 99 HU are deducted from the voxel value. An upper threshold of 4 (corresponding to >400 HU) is then applied, which causes non-linearity. Finally, the volume of the lesion (defined as all contiguous voxels with density >130 HU) is multiplied by the peak density value, which introduces false homogeneity as well as high sensitivity to noise. Demer et al. argue that while these simplifying steps may have saved computational power when the algorithm was introduced in 1990, this should not be a consideration nowadays in light of the technical advancements of computers; the authors advocate the use of calcium mineral density and volume as predictors over the Agatston-based score, as these parameters do not have the aforementioned limitations. [34] Moreover, several studies found that coronary calcium mineral mass measurements were less susceptible to interscan variability than Agatston scores [35,36]. Such interscan variability, which occurs due to partial volume effects and variations in scan parameters and starting position, may cause changes in risk stratification [35,36]. In light of these advantages, it seems preferable to use calcium mass measurements over the traditional Agatston score. Nevertheless, calculation of calcium mineral mass based on 'regular' multidetector CT scans, using a calibration phantom to relate Hounsfield units to calcium concentration, may still be susceptible to partial volume effects that are pronounced with small calcifications [35]. Dual-energy CT can be used to quantify the density of calcifications within the vascular wall as well [37]: the high- and low-energy projections can be used to decompose the image into two or three materials, yielding material-specific images which provide concentration information [37,38]. As DECT allows for the calculation of the partial calcium content of any voxel, it may be less susceptible to variability caused by partial volume effects [39].

Finally, the included studies exhibited significant heterogeneity in terms of the calcium scores which were used. Among the employed scores were quantitative scores based on the method by Agatston et al., semiquantitative scores employing various calcification parameters including length, circumferentiality or percentage of vessel calcification, and dichotomous measures [14]. Several scores exhibited predictive value with regard to clinical outcomes; however, the aforementioned heterogeneity made direct comparison of different scores impossible and, as such, no single calcium score stood out as superior for the prediction of clinical events. For this reason, further research should investigate which calcification measurements provide the best predictive value and should develop a standardized method for the calculation of a peripheral calcium score based on these findings. Standardization of peripheral calcium scoring will facilitate adoption of this score in further research, which in turn could allow comparison of results between different studies by means of meta-analysis. Furthermore, such a standardized, image-based peripheral artery calcium score might be a promising tool for use in clinical practice as well. After all, assessment of the degree of calcification is highly subjective in current clinical practice, as is highlighted by the operationalization of calcification within the GLASS system [2].

A first step towards such a standardized calcification score can be to (semi)automatically segment (i.e. detect and label) calcifications. This may allow for automatic calculation of quantitative calcium scores and parameters included in semiquantitative scores. This would, in turn, facilitate rapid application of the new, standardized calcium score to large data sets, allowing further research to confirm (or disprove) the associations found in the aforementioned systematic review. Dual-energy CTA may be a potential solution for this as well; segmentation of calcifications may be possible either through generation of a virtual non-contrast scan or by means of material decomposition.

Therefore, this research project aimed to improve on the limitations of current calcification scoring methods by investigating the potential of dual-energy CTA imaging, specifically virtual non-contrast scan generation and material decomposition, for the quantification of calcium mass and segmentation of calcifications. As a first step towards this aim, a phantom experiment was conducted to validate the performance of DECTA with respect to these functions, the methods and results of which will be reported in this chapter. To provide context to the methods of this phantom experiment, the technical background of dual-energy CT will first be described in the next section.

Technical background

Dual-energy CT imaging

In dual-energy CT imaging, attenuation data is obtained with two source spectra at different peak energies, which provides more information on the energy-dependent attenuation characteristics of different tissues and materials [29,38]. Several technical approaches exist for acquiring the two datasets, each of which has its own advantages and disadvantages. The three methods which are currently most prevalent in clinical practice are dual source dual-energy CT, single source dual-energy CT with fast kVp (peak kilovoltage) switching and dual-layer detector dual energy CT [37]. These methods are visualized in figure 2.1.

In dual-source DECT, two x-ray tubes and detectors are mounted on the gantry at an angle of approximately 90-95°, depending on the scanner generation, and both sets are acquired simultaneously. An advantage of this method is the ability to optimize the filtration for each of the X-ray tubes separately, which improves spectral separation [29,40]. Disadvantages include cross scattering between the two source-detector systems, which requires a special scattering correction algorithm, and a limited field of view [29,40]. Furthermore, because the two data sets are approximately 90° out of phase, reconstruction is performed in the image space instead of the projection space (as in single-source and dual-layer detector DECT). This limits some clinical applications of DECT imaging using this method, including artifact reduction and quantification of material density [37,40].

In single source DECT with fast kVp switching, the tube potential is rapidly alternated between a high and low voltage (typically 140 and 80 kVp respectively). This results in near-simultaneous acquisition of two data sets at different energies, allowing for projection-based reconstruction. An downside to this technique, however, is the inability to optimize tube filtration for both energies, resulting in relatively high spectral overlap; this decreases the accuracy of material differentiation. [37,40]

Finally, dual-layer detector spectral CT uses a single high-potential beam and two layered (”sandwich”) scintillator detectors [37,40]. The top layer detects low-energy photons, whereas the bottom layer measures the high-energy photons [40]. Downsides to this method are relatively high spectral overlap and different noise levels between the high- and low-energy data set, although the latter is partially prevented by using different detector thicknesses [40]. A major advantage, however, is the fact that spectral CT information is collected for every patient regardless of protocol [29]. This allows for retrospective analysis of dual-energy images, whereas for the other methods dual-energy protocols must be selected prospectively. This is especially useful within the context of this research project, as the ability to retrospectively collect dual-energy data may allow for rapid application of a standardized calcium score to large data sets. Therefore, the dual-layer detector technique for spectral CT imaging will be used to acquire all data sets in this project.

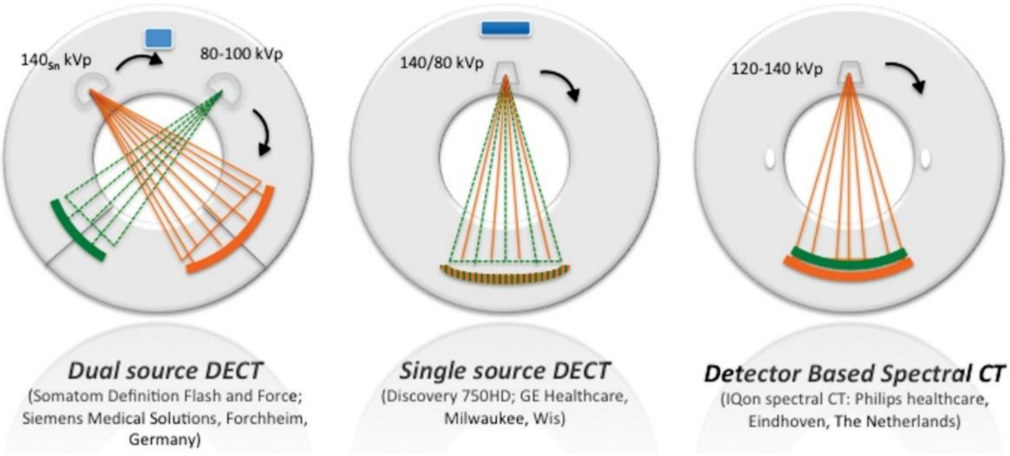

Figure 2.1: Visual representation of the main types of dual-energy CT (DECT) scanners currently used in clinical practice. Image reprinted from Patino et al. [37]

The dual-energy CT data may be reconstructed into various types of images, such as virtual monoenergetic (VME) images and material-specific images [37,38,40]. VME images visualize an object as if it was scanned with a single photon energy, instead of the polyenergetic x-ray beam which is actually used. Low-energy VME images (e.g. 40 keV) may be used to boost iodine contrast agent, improving vascular visualization at lower contrast agent doses [28,38]. The increased noise observed for such low energy projections can be compensated for to some extent by applying energy domain noise reduction, which DECT enables [40]. Conversely, VME images at higher energies may be used to reduce beam hardening and blooming artifacts associated with metallic stents and severe calcification [37,38].

Material-specific images (also known as material density images; MDIs) can be generated through two-material decomposition analysis in the projection domain [37,38]. Two-material decomposition algorithms assume that the volume consists of two chosen materials. From the attenuation measurements at both energy levels the volume fraction of the two materials is calculated, based on the known attenuation properties of the chosen materials at different energies [37,38]. Any two materials may be selected as the basis materials, although the best results are obtained when materials with different densities are chosen; in practice, iodine and water are the most common basis pair [38]. One component may then be subtracted from the other, yielding an iodine/water MDI in which vessels are boosted or a water/iodine MDI in which the iodine contrast agent is suppressed; the latter can be used as a virtual non-contrast image (VNC) [37,38]. Iodine/calcium MDIs may be used to remove bone and calcified plaques from an image to improve vascular delineation (e.g. near the skull base) [28,37,40]. The basis for material decomposition will be examined in more detail in the next section.

With the dual-layer detector CT scanner, the spatially and temporally aligned projections measured by each of the two detector layers can be summed and weighted to generate a conventional CT reconstruction as well [29,37]. This is beneficial, as spectral CT data is collected for all patients scanned with this scanner, but only a conventional CT scan may be desired. Van Ommen et al. showed that the use of two detector layers does not incur a penalty to image quality [29]. The dual-layer detector scanner exhibited similar CT number linearity, spatial linearity, slice thickness and spacing as conventional scanners, as well as slightly improved contrast and spatial resolution in spite of slightly increased noise compared to the conventional scanner [29].

Material decomposition

In 'regular', single-energy CT imaging, the linear attenuation coefficient $\mu(x, y, z)$ at a single average energy $\bar{E}$ is reconstructed throughout an object from measurements of the intensity of X-ray beams that pass through the object at various projections. The intensity of a monoenergetic x-ray beam after passing through a homogeneous object can be described with the following equation [41]:

$$I = I_0 \, e^{-\mu x} \tag{1}$$

Where I is the intensity after passing through the object, I_0 is the initial intensity of the beam, μ is the linear attenuation coefficient of the object and x is the distance the beam has to travel through the object. Of course, this formula is a simplification of the reality of medical imaging, as the beam produced by an x-ray tube is polyenergetic and the human body is not homogeneous. As such, the contribution of each voxel to the total attenuation and the contribution of every photon energy must be summed, leading to the introduction of two integrals in the formula shown above. The intensity of the exiting X-ray beam as it passes through an object can be described with the following line integral [42(p.461–502),43]:

$$I = \int S(E) \, e^{-\int \mu(x,y;E) ds} dE \tag{2}$$

Where S is the source spectrum as a function of photon energy E and s is the distance along the line traveled by the beam.

Discrimination between different tissues and materials based on these images may be difficult [37,40]. Different materials may have very similar CT numbers in an image, despite having different elemental compositions [37,40]. After all, the linear attenuation coefficient $\mu(E)$, on which the CT numbers are based, is not only dependent on material composition (more specifically, the average atomic number within a voxel $\bar{Z}$), but also on the energies of the photons within the X-ray beam and the mass density of the material; as such, this linear attenuation coefficient is not unique for every material. [40]

The acquisition of attenuation measurements with a different energy spectrum, as in dual-energy CT, may allow differentiation between two materials. After all, if two voxels with a different elemental composition, such as calcium and iodine, have a similar attenuation coefficient at one average energy, they will have different attenuation coefficients at another energy level. Dual-energy CT uses attenuation measurements acquired with two different energy spectra, as well as known differences in attenuation between different materials for these spectra, to discriminate between and quantify material composition. [40]

Differences in attenuation at different energies occur due to differences in the relative contribution of the photoelectric effect and Compton scatter, the two dominant phenomena that cause X-ray attenuation at diagnostic X-ray energy levels ($E < 150 \; keV$) [37,40]. These interactions are shown in figure 2.2 below.

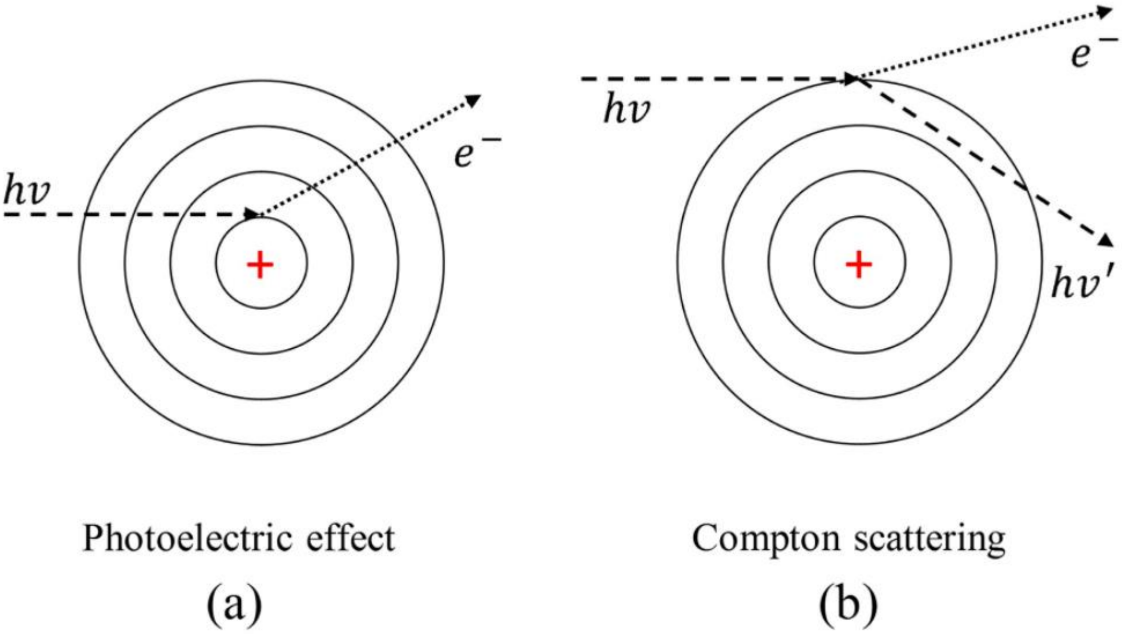

Figure 2.2: Schematic visualization of the photoelectric effect (a) and Compton scattering (b) interactions, the two dominant photon interactions in the diagnostic X-ray energy range. The red plus sign denotes the atom's nucleus, while the concentric circles represents its electron shells. $h\nu$ and $h\nu'$ denote the photon energy before and after the interaction, respectively; e^{-} indicates an ejected electron. Image adapted from Shahmohammadi Beni et al. [44]

In the photoelectric effect, the X-ray photon is absorbed by the atom it interacts with and a single photo-electron is ejected from the atom [42(p.425–59)]. The kinetic energy of the photo-electron is equal to the kinetic energy of the initial photon minus the binding energy of the electron [42(p.425–59)]. Generally, the cross section of the photoelectric effect (i.e. the probability of this interaction occurring) increases strongly with increasing atomic number and with decreasing x-ray energy [37,42(p.425–59)]. However, abrupt increases in the cross section also occur as the energy increases beyond an 'edge', which corresponds to the binding energy of an electron shell and is therefore named after this shell [37,42(p.425–59)]. As the photon energy increases beyond this edge, the photon can also dislodge electrons in the corresponding shell, increasing the probability of the photoelectric interaction occurring [37,42(p.425–59)].

In Compton scattering, an electron is ejected from the atom and the photon scatters at an angle θ to its original trajectory, with its energy reduced depending on this scattering angle [42(p.425–59)]. The energy of the electron and new photon can be calculated by considering quantum mechanics [42(p.425–59)]. However, this is not relevant to the following discussion, so these formulas will not be given here. Compton scattering is proportional to the atomic number, but is relatively independent of the energy of the X-rays in the diagnostic X-ray range [37,42(p.425–59)]; it tends to be the most important interaction at higher X-ray energies due to the photoelectric effect decreasing [42(p.425–59)].

The linear attenuation coefficient is a monotonic and smoothly variation function, as long as a material has no K- or L-edges within the diagnostic x-ray energy range [43]. As a result, the linear attenuation coefficient can be modeled as a linear combination of the photoelectric interaction and Compton scattering, as was shown by Alvarez and Macovski [43]. As a formula [43,45]:

$$\mu(E) = a_p f_p(E) + a_c f_c(E) \tag{3}$$

In this formula, a_p and a_c are material-specific constants and f_p and f_c are basis functions describing the energy dependencies of the photoelectric absorption and Compton scattering, respectively [45]. These basis functions were chosen empirically by fitting potential functions to experimental data [43]. Alvarez and Macovski used the following basis functions, reporting favorable results when these were fitted to experimental data [43]:

$$\mu(E) = a_p E^{-3} + a_c f_{KN}(E) \tag{4}$$

Where $f_{KN}(E)$ is the Klein-Nishina formula (not shown for the sake of brevity) and the material-specific constants a_p and a_c are given by the following formulas [43]:

$$a_p \approx K_p \frac{\rho}{A} Z^n, \qquad n \approx 4 \tag{5}$$

$$a_c \approx K_c \frac{\rho}{Z} \tag{6}$$

Where K_p and K_c are constants, ρ is mass density, A is atomic weight and Z is the atomic number.
Conveniently, these basis functions – $f_p(E) = E^{-3}$ and $f_c(E) = f_{KN}(E)$ – describe the energy dependency of the photoelectric and Compton cross section, respectively: Hobbie and Roth report that the photoelectric cross section τ can be approximated by:

$$\tau \propto Z^4 E^{-3} \tag{7}$$

and the Compton scattering cross section is described by the Klein-Nishina function [42(p.425–59)]. Furthermore, the relationship between the constants a_p and a_c and material characteristics becomes apparent from the inclusion of the mass density ρ, atomic weight A and atomic number Z. As such, while these functions were originally fit empirically, they do have physical meaning [43].
As was mentioned previously, the measurements made with CT are line integrals of the attenuation function that should be reconstructed. Since formula (2) holds true, measuring the line integral of μ is equivalent to measuring the line integrals of the coefficients a_p and a_c [43]:

$$\int \mu(x, y; E)\, ds = A_1\, E^{-3} + A_2\, f_{KN}(E) \tag{8}$$

With

$$A_1 = \int a_p(x, y)\, ds \qquad \text{and} \qquad A_2 = \int a_c(x, y)\, ds \tag{9}$$

To reconstruct $a_p(x, y)$ and $a_c(x, y)$, from which the material composition can be determined, the line integrals A_1 and A_2 must be measured at every point in the projections of the object [43]. Thus, there are two unknown variables which must be solved for; therefore, two independent information sources are required. These can be acquired by performing intensity measurements with two different source spectra [43]. In formula [43]:

$$I_1(A_1, A_2) = T \int S_1(E)\, e^{-A_1/E^3 - A_2\, f_{KN}(E)} dE \tag{10}$$

$$I_2(A_1, A_2) = T \int S_2(E)\, e^{-A_1/E^3 - A_2\, f_{KN}(E)} dE \tag{11}$$

where I_1 and I_2 are the two intensity measurements, S_1 and S_2 are the two source spectra and T is the measurement time [43]. This is where dual-energy CT comes in: each of the dual-energy methods described in the previous section can be used to apply the two source spectra and obtain the two intensity measurements.

The experiments described in this thesis were performed on a dual-layer detector spectral CT scanner. For these experiments, two virtual mono-energetic images (100 and 50 keV respectively) were used as the two intensity measurements I_1 and I_2. Using these images ensured the assumption was met that no K- or L-edges were present within the selected energy range for the materials of interest: the K-edge for iodine can be found at 33.1694 keV [46]. The K-edge for calcium and L-edges of both elements have considerably lower binding energies and thus are not relevant [46].

Using this method, the relative contribution of the photoelectric and Compton scatter interactions can be calculated for every voxel; these contributions can then be plotted against one another in a so-called ρZ-map [40,43]. By comparing the voxel values with the known attenuation contribution of the photoelectric effect and Compton scattering for increasing densities of basis materials, the material composition of voxels as the sum of these basis materials can be differentiated and quantified; this is done through three-material decomposition analysis [38,40,43]. This process is visualized schematically in figure 2.3. A triangular diagram is drawn between three basis materials, of which the attenuation characteristics – and thus the corresponding place on the graph – are known. Using the two-material decomposition method described in the previous section, the densities of two basis materials can be calculated from the two dual-energy data sets, after which the fraction of the third basis material follows from the assumption of mass or volume conservation ('the completeness assumption') [37,38,40]. The contribution of any of these three basis materials can then be eliminated by mapping each voxel onto the calibration diagram based on its relative position in the triangle [37,38,40]. It should be noted that the mass fractions calculated through this method are only valid if the investigated volume can reasonably be assumed to consist of these three materials.

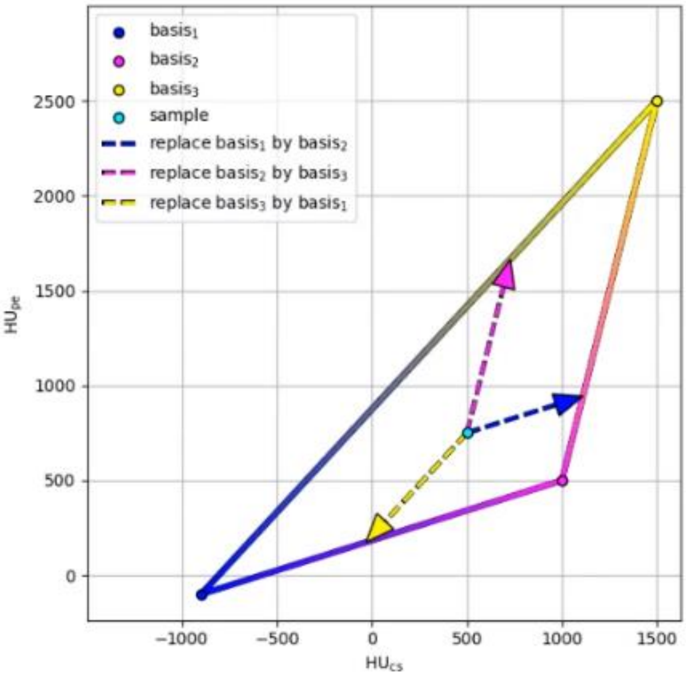

Figure 2.3: Schematic visualization of the three-material decomposition method. The attenuation in Hounsfield Units attributed to the photoelectric effect (HU_{pe}) and Compton scattering (HU_{cs}) are shown on the Y-axis and X-axis respectively. A calibration triangle is drawn based on known attenuation data for three basis materials, after which every voxel may be decomposed into mass fractions for each of these basis materials. Reprinted with permission from Schilham et al. [47].

Phantom experiment

Methods

Approach and set-up

The objectives of this phantom experiment were twofold: (1) to investigate the performance of the dual-energy system in generating a virtual non-contrast scan and (2) to validate the quantification of calcification density based on dual-energy CT data.

In order to allow accurate calcium scoring, ideally the VNC reconstruction should completely suppress the iodine contrast agent, but not the calcifications. This can be validated by measuring the Hounsfield units in regions corresponding to iodine contrast agent and calcifications on CTA images before and after iodine suppression and comparing these values to a true non-contrast CT scan [33,48].

For this purpose, a vascular phantom was used, which is shown in figure 2.4. This phantom was previously manufactured for and used in a similar phantom experiment investigating the use of dual-energy imaging for calcification quantification [49]. The phantom has a central tube, which can be filled with iodine contrast agent to represent a vessel. Around the tube are concentric rings, which consist of mixtures of synthetic calcium hydroxyapatite powder ($Ca_5(OH)(PO_4)_3$; Sigma-Aldrich, Burlington, MA, USA), the same compound which forms vascular calcifications in vivo [50], and Ecoflex 00-50 silicone rubber (Smooth-On, Inc., Macungie, PA, USA). The rings were designed to have increasing, predefined densities of hydroxyapatite – 0 mg/ml, 75 mg/ml (two rings), 100 mg/ml and 150 mg/ml respectively – to test the performance of the DECT system with regard to calcium quantification and VNC scan generation with increasing density [49]. The final density of the rings varied slightly from the designed density due to minor inaccuracies in the production process, as is shown in Table 2.1. As the vascular phantom contains calcium hydroxyapatite rings in close proximity to the contrast-filled vessel, it was hypothesized to serve as a good test for the DECT system's ability to separate these components in the generation of a VNC scan. However, the x-ray attenuation of the Ecoflex silicone rubber, which was used to manufacture the hydroxyapatite rings, has not been validated to be comparable to water. Therefore, a commercial bone density calibration phantom (BDC-3; QRM GmbH, Möhrendorf, Germany), shown in figure 2.5, was scanned as well. This phantom consists of three cylindrical inserts in a housing with soft tissue-equivalent attenuation at 120 kV. The inserts have a diameter of 18 millimeters and consist of CT_{WATER}, a solid water-equivalent plastic that exhibits the same X-ray attenuation as water, with increasing concentrations of hydroxyapatite (0 mg/ml, 100 mg/ml and 200 mg/ml respectively). [51] Aside from allowing assessment of VNC scan generation performance, these two phantoms also support validation of calcification quantification, as the phantoms contain several known calcium densities.

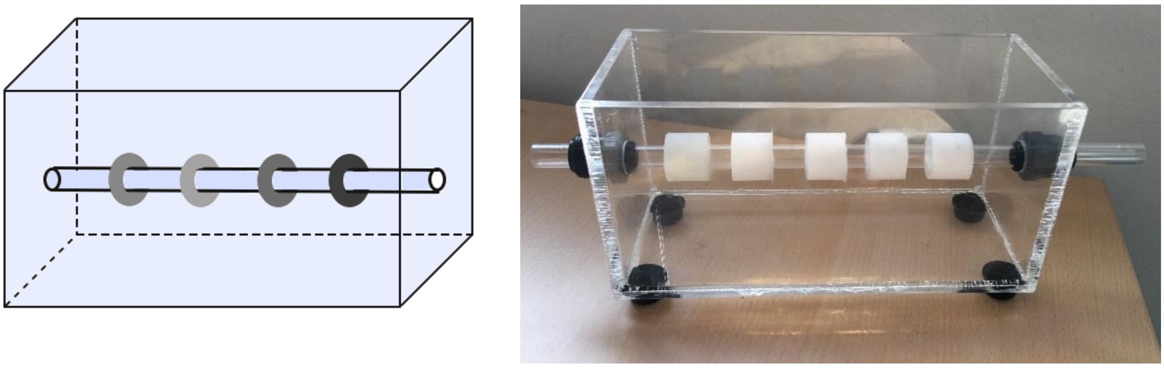

Figure 2.4: The vascular calcification phantom used for validation of dual-energy CTA. Left: Schematic overview showing the central tube, which represents a vessel, with concentric hydroxyapatite rings,

which represent calcifications. Right: Photo of the phantom, showing the hydroxyapatite rings with increasing density from left to right. Reprinted with permission from Simons [49].

Table 2.1: Designed and actual density and volume of the hydroxyapatite rings in the phantom shown in figure 2.4; reprinted with permission from Simons [49].

Ring number	Designed density of CaHA (mg/ml)	Actual density of CaHA (mg/ml)	Ring volume (ml)
1	0	0	6.89
2	75	71.4	6.69
3	75	69.6	6.70
4	100	102	6.44
5	150	141	7.02

Abbreviation: CaHA, calcium hydroxyapatite; mg/ml, milligrams per milliliter.

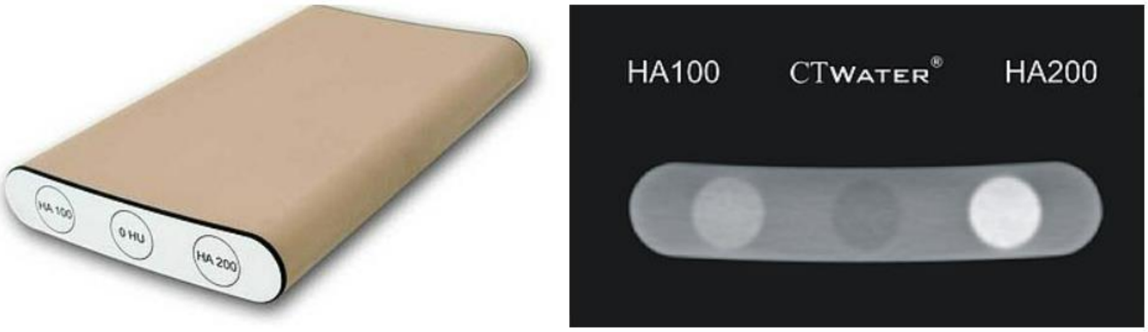

Figure 2.5: The commercial bone density calibration phantom used for the phantom experiment. Left: three-dimensional model of the phantom. Right: Axial CT slice of the phantom, showing the inserts with different concentrations of hydroxyapatite (HA). The CT_{WATER} insert corresponds with a HA density of 0 mg/ml. The attenuation can be noted to increase as the HA density increases. [51]

For the phantom experiment, the open container of the vascular phantom was filled with water to approach the physiological situation in terms of scattering. In the previous phantom experiment described by Simons, some image distortion was observed at sharp attenuation transitions between the hydroxyapatite rings and air bubbles trapped on the surface of these rings [49]. In this experiment, the filled phantom was left to settle for an hour to allow any air bubbles to dissolve as much as possible. Ultravist-300 contrast agent (Bayer Pharmaceuticals, Leverkusen, Germany) – 0.623 g/ml iopromide ($C_{18}H_{24}I_3N_3O_8$]), equivalent to 300 mg iodine (I) / ml– was diluted with water at a 1:29 ratio to a concentration of 10 mg I / ml [52]. This concentration was chosen as target values between 200 and 300 HU have been reported for aortic enhancement and Bae found that the attenuation of iodine contrast agent was 25-30 HU per milligram per milliliter at 120 kVp [53–55]. For the contrast-enhanced scans, the central tube of the phantom was filled as much as possible with the diluted contrast agent by injection with a syringe. For the unenhanced scans, the tube was filled with water instead. The tube was subsequently closed with a plug. The phantom was placed in the CT scanner with the central tube oriented along the axial scan direction. Finally, the commercial BDC phantom was placed on top of the first phantom, with the cylindrical inserts oriented along the axial scan direction as well.

Scan protocol

The phantoms were scanned on a Philips IQon spectral CT scanner (Philips Healthcare, Best, The Netherlands) with varying scanning parameters. The vascular phantom was scanned both with and without contrast agent to allow comparison of the virtual non-contrast scan with the actual non-contrast scan. The time interval between injection of the contrast agent and the CT scans was minimized to prevent sedimentation of the iodine. The scanning parameters used are summarized in Table 2.2. The CT dose index (CTDI) was set to standardize the dose output by the scanner, in order to facilitate comparison with other scanners; for any given value set for the CTDI, the scanner automatically adapted the tube current to yield this dose. Scans were reconstructed with a field of view of 300 millimeters and the reconstruction matrix was 512 x 512 pixels.

Table 2.2: Scan parameter settings for the phantom experiment

Scan parameters	Setting(s)	No. of settings applied
Scan direction	Craniocaudal	1
Scan option	Helical	1
Tube potential (kV)	120	1
CTDI	3 / 6 / 26.5*	3
Tube current (mAs)†	40 / 79 / 350	
Pitch	0.797	1
Rotation time (s)	0.75	1
Reconstruction	Axial 1/1; Axial 1/0.9 ‡	2
Resolution	Standard / High	2
Reconstruction kernel	Standard / Sharp	1 / 2 §
Reconstruction algorithm	iDose(6) / IMR	2
Contrast agent	Yes / No	2
	Total number of scans	60

Abbreviations: kV, kilovolt; CTDI, CT dose index; mAs, milliampere-seconds; s, seconds; IMR, iterative model reconstruction.

* Highest possible value for this particular scanner.

† The CT dose index (CTDI) was set to allow comparison with other scanners; the tube current was adapted automatically by the scanner software to ensure constant CDTI. As such, the tube current varied slightly with the chosen resolution; shown are the values for standard resolution.

‡ These parameters denote slice thickness and slice interval, respectively.

§ The 'Sharp' reconstruction kernel was only tried for the contrast-enhanced scan with high resolution.

Because of temporal and logistic constraints, not all of these different scans were analyzed within the scope of this thesis. For the VNC scan generation and material decomposition analysis, the scans with the following parameters were used:

- CTDI: 6;
- Tube current: 79 mAs;
- Reconstruction: Axial 1/0.9;
- Resolution: standard;

- Reconstruction kernel: standard;
- Reconstruction algorithm: iterative model reconstruction (IMR);

Additionally, the scans with the same parameters as above, except for reconstruction with the iDose algorithm (level 6) instead of IMR, were examined to compare the quality of these phantom scans to those performed in the previous phantom experiments; after all, iDose reconstruction was used in these experiments as well.

Analysis

Virtual non-contrast scans were generated using Philips IntelliSpace Portal software version 12.1 (Philips Healthcare, Best, The Netherlands). The average Hounsfield Units were measured for several areas of interest within the phantom image, including the contrast agent-filled tube and hydroxyapatite rings of the vascular phantom, the inserts of the BDC phantom and the water in the container of the vascular phantom. This was done by drawing three to five ROIs per structure using the 'Circle' or 'Ellipse' tool available in IntelliSpace and averaging the results. These measurements were performed both before and after iodine suppression, to calculate the absolute and relative difference in Hounsfield Units due to the iodine suppression.

Material decomposition analysis was performed according to the method by Alvarez and Macovski, as described in the section 'Material decomposition' [43]. An implementation of this method in the open source programming language Python (Python Software Foundation), written by A. Schilham, clinical physicist at the UMC Utrecht, was used [47].

As part of the material decomposition analysis, the contribution of the photoelectric effect and Compton scattering interactions were calculated for each voxel based on the dual-energy CT data, after which these contributions were plotted. The known photoelectric and Compton attenuation coefficients for increasing densities of pure iodine and calcium hydroxyapatite (CaHA), based on data from the U.S. National Institute of Standards and Technology (NIST), were plotted into this figure as well [56]. Three-material decomposition was used to calculate the calcium density for each the of hydroxyapatite rings in the vascular phantom, as well as for each of the inserts in the BDC phantom.

Results

Scan quality

Figure 2.6 shows a sagittal reconstruction of the previous phantom experiment, as reported by Simons, as well as a sagittal reconstruction from this phantom experiment [49]. As can be appreciated from the bottom panel of this figure, the vascular phantom still contains some air bubbles in the current experiment, especially around the hydroxyapatite rings, despite being left to settle for an hour prior to scanning. However, these air bubbles are significantly fewer in number than in the images from the previous experiment, as seen in the top panel of figure 2.6. Consequently, the bottom image in figure 2.6 appears to remain relatively free from the distortion caused by the bubbles in the top image.

In the bottom image, however, some streak artifacts can be seen (indicated by the white arrowheads). These artifacts are most likely caused by beam hardening due to the BDC phantom's positioning on the vertical sides of the vascular phantom container [57]. Both these streak artifacts and the air bubbles were avoided as much as possible while placing the ROIs for measurement of the mean attenuation.

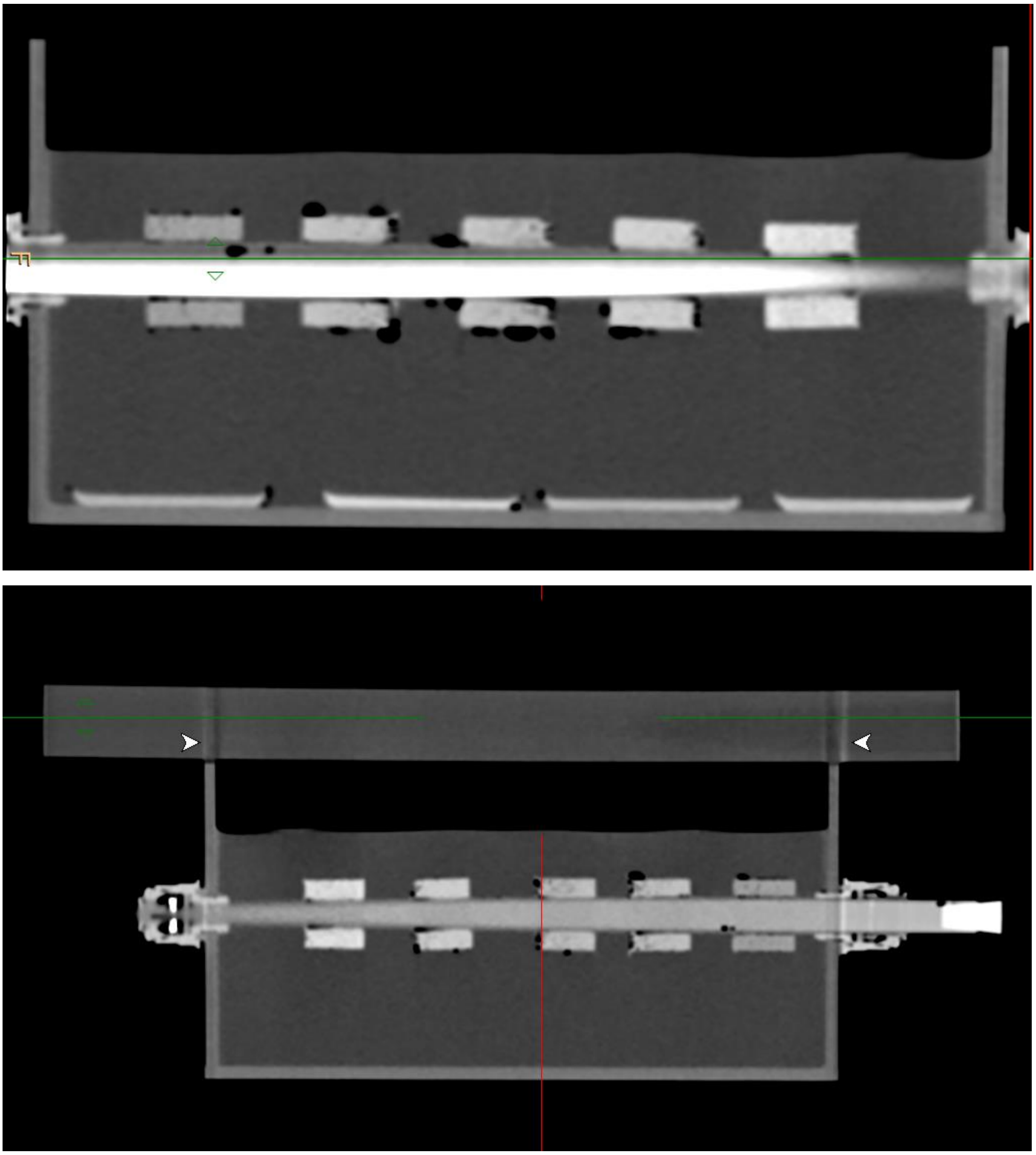

Figure 2.6: Sagittal reconstruction of the previous phantom experiment (top panel), as reported by Simons, as well as the current phantom experiment (bottom panel). The bottom image can be observed to contain fewer bubbles than the top image. However, in the bottom panel some streak artifacts are seen in the BDC phantom, as indicated by the white arrowheads.

Virtual non-contrast scan

The result of virtual non-contrast scan generation is shown in figure 2.7; an axial slice, taken at the level of hydroxyapatite ring 5 (~150 mg CaHA / ml), is shown before and after contrast suppression. As can be appreciated from this figure, the contrast agent is indeed suppressed and appears to have the same attenuation as the water surrounding the hydroxyapatite ring and central lumen. However, the hydroxyapatite ring of the vascular phantom and hydroxyapatite inserts of the BDC phantom are suppressed to some extent as well. The mean attenuation (in Hounsfield Units) was measured for various areas of interest before and after iodine suppression, the results of which are shown in Table 2.3. The mean attenuation of the same areas was measured on a true non-contrast scan as well, to serve as comparison.

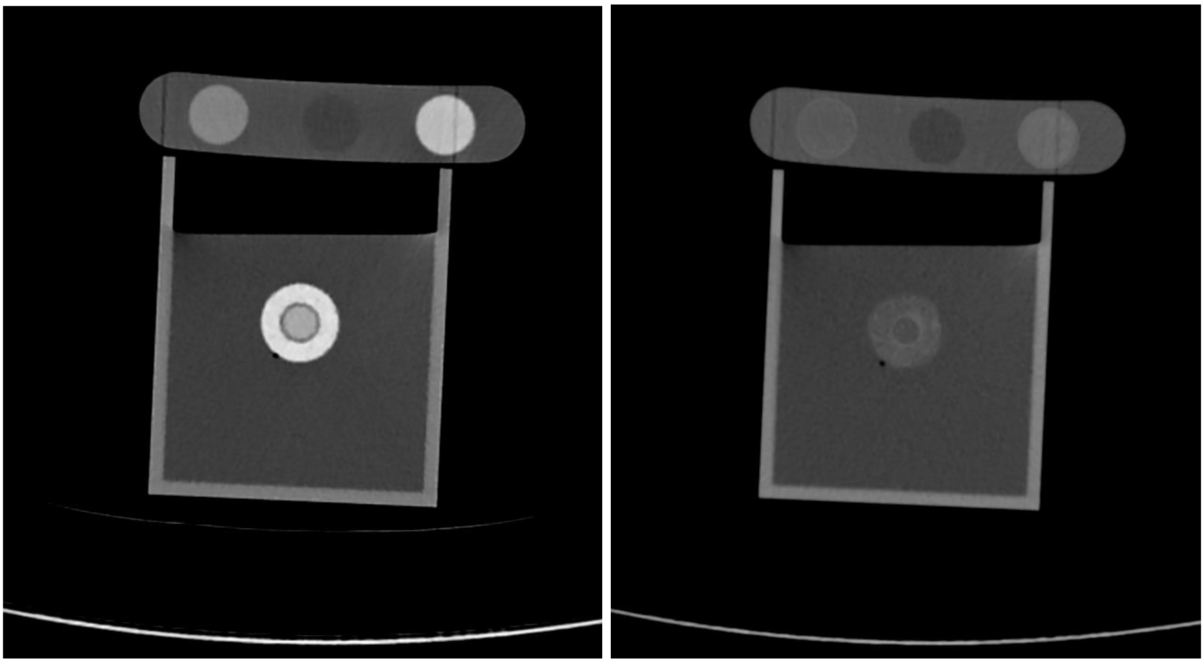

Figure 2.7: Axial slice of the phantom CTA scan, taken at the level of hydroxyapatite ring 5 (~150 mg/ml CaHA). Left: conventional CTA reconstruction. Right: The corresponding VNC reconstruction.

Table 2.3: The effect of iodine suppression, as in the VNC algorithm, on the mean attenuation in several regions of interest within the phantom image. Note that IntelliSpace denotes the attenuation on the VNC scan with HU* instead of HU, to indicate that the Hounsfield Units are modified by the algorithm. The mean attenuation values in the true unenhanced scan are given as well for comparison.

Regions of interest		**Contrast scan**		**VNC scan**		**Suppression (difference in HU)**		**True unenhanced scan**	
		Mean HU	**SD**	**Mean HU***	**SD**	**Absolute (HU)**	**Relative (%)**	**Mean HU**	**SD**
Vascular lumen		248.7	4.8	22.3	5.4	-226.3	-91.0%	-3.8	4.9
Vascular phantom rings	Ring 1	221.1	10.2	0.7	6.7	-220.4	-99.7%	212.7	6.6
	Ring 2	298.1	6.8	18.9	4.2	-279.2	-93.7%	295.3	7.2
	Ring 3	290.6	7.1	25.1	5.4	-265.6	-91.4%	297.5	7.2
	Ring 4	328.6	6.1	33.5	5.7	-295.1	-89.8%	325.6	7.1
	Ring 5	381.3	9.8	61.8	6.3	-319.5	-83.8%	360.6	16.8
BDC phantom inserts	0 HA	-1.4	4.7	-1.1	4.4	0.2	+17.1%	1.0	5.3
	100 HA	149.3	4.8	53.1	5.0	-96.3	-64.5%	150.7	5.7
	200 HA	294.7	5.5	93.0	5.0	-201.7	-68.4%	246.6	5.7
Water		-2.8	4.9	-0.6	4.8	2.2	+79.4%	-2.7	5.1

Abbreviations: VNC, virtual non-contrast; HU, Hounsfield Units; SD, standard deviation; HA, hydroxyapatite.

Material decomposition

The results of material decomposition are shown in figure 2.8, which is a map showing the contributions of the photoelectric effect (on the Y axis) and Compton scattering (on the X axis) to the total attenuation for every voxel in the phantom image. Figure 2.9 highlights a frame from this plot, zooming in on the relevant data. In both figures, the reference data for increasing concentrations of iodine in water and calcium hydroxyapatite (CaHA) in water are shown as an orange and a purple line, respectively; a third line could be drawn between the endpoints of the orange and purple line to complete a calibration triangle as shown in figure 2.3. The yellow, pink and cyan circular markers on the purple line indicate the expected location on the plot for 0, 100 and 200 mg/ml of calcium hydroxyapatite respectively. The point clouds below each of these markers (indicated in figure 2.9 with the red arrowheads) were confirmed to correspond to the inserts of the BDC phantom by drawing an ellipse around these point clouds and examining the segmentation in the original image. The average calcium density was calculated for each of these point clouds, both with calcium hydroxyapatite and water as basis materials, as well as calcium hydroxyapatite and a hand-selected area for water-equivalent plastic; the results are shown in Table 2.4. The red, magenta, pink, purple and blue point clouds (indicated in figure 2.9 with the white arrows) that mapped close to the orange water-iodine line correspond to the hydroxyapatite rings in the vascular phantom; this was confirmed by placing a region of interest in the phantom image, which highlighted the pixels on these point clouds in the ρZ-map. The colored, circular markers close to these point clouds show the expected points on the ρZ-map for the measured densities of each of the rings, after decomposition with calcium hydroxyapatite and Ecoflex silicone gel as basis materials; the value for Ecoflex was based on a hand-selected area in the diagram. The pink marker was omitted for the sake of clarity, as it was very close to the cyan marker on the diagram.

As the point clouds corresponding to the hydroxyapatite rings in the vascular phantom were located far from the water-calcium hydroxyapatite line, no average calcium density was calculated for these rings.

Table 2.4: The average calcium density of the point clouds corresponding to the bone densitometry calibration phantom inserts, calculated based on three-material decomposition analysis using two different combinations of basis materials.

Basis materials	**Calculated calcium density**		
	Insert 1 (0 mg/ml CaHA)	**Insert 2 (100 mg/ml CaHA)**	**Insert 3 (200 mg/ml CaHA)**
CaHA and water	-11.6 mg/ml	90.3 mg/ml	190.7 mg/ml
CaHA and water-equivalent plastic	-0.8 mg/ml	100.6 mg/ml	200.7 mg/ml

Abbreviations: mg/ml, milligrams per milliliter; CaHA, calcium hydroxyapatite.

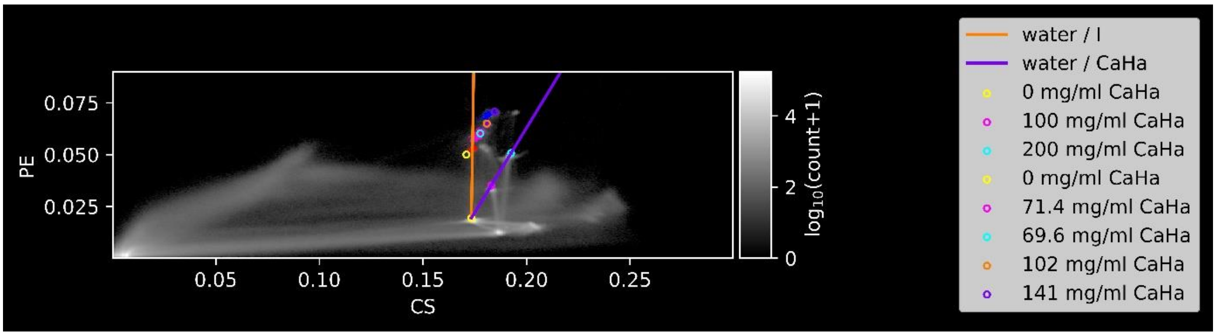

Figure 2.8: Plot showing the relative contribution of the photoelectric effect (PE; on the Y axis) and Compton scattering (CS; on the X axis) for every voxel in the phantom image. Lighter pixels indicate a higher voxel count for any given combination of PE and CS, as is visualized by the grayscale next to the graph. A zoomed-in frame from this plot, containing the most relevant data, is shown in figure 2.9.

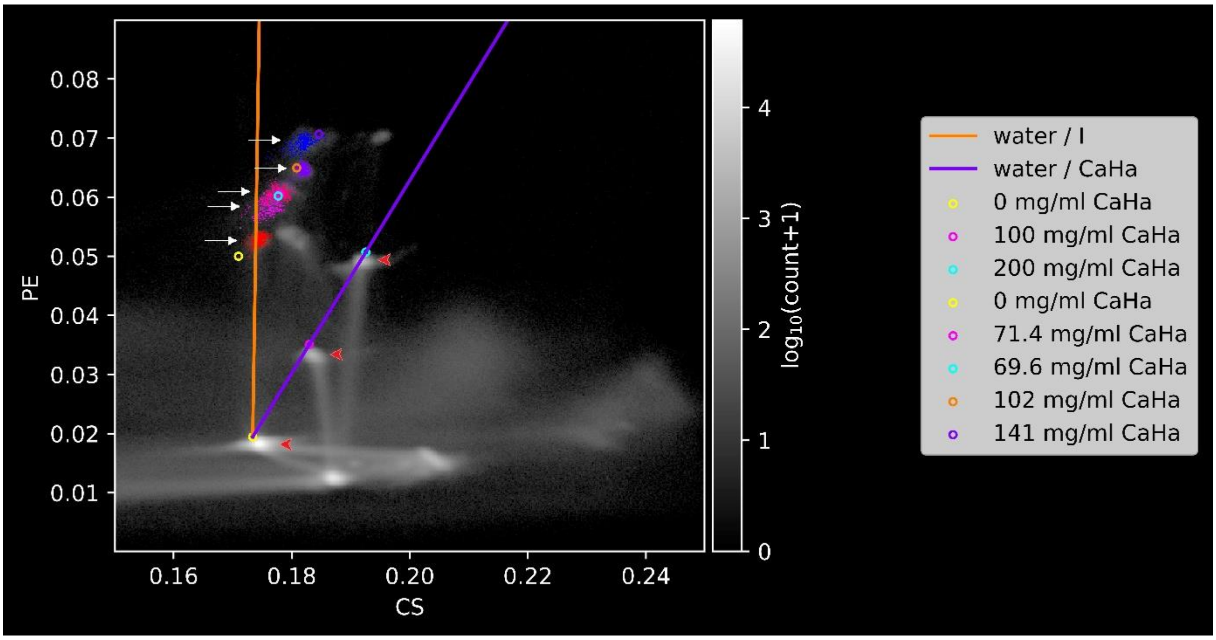

Figure 2.9: Zoomed-in frame from the material decomposition plot shown in figure 2.8, visualizing the relevant data. The orange and purple lines show reference data for increasing concentrations of iodine (I) in water and calcium hydroxyapatite (CaHA) in water, respectively. The colored markers on the purple line indicate the expected place on the plot for the calcium densities of the BDC phantom inserts after decomposition with water and CaHA as basis materials. The red arrowheads below these markers show point clouds corresponding to these inserts. The colored point clouds close to the orange line, denoted with white arrows, correspond to the hydroxyapatite rings of the vascular phantom. The colored markers near to these point clouds show the expected place on the plot for the calcium densities of these rings, after decomposition with calcium hydroxyapatite and the Ecoflex silicone rubber; the parameters for the Ecoflex silicone rubbers were obtained by means of a hand-selected area in the plot.

Discussion

The objective of this phantom experiment was to investigate the performance of virtual non-contrast scan generation and calcification quantification by means of material decomposition analysis using dual-energy CTA. The VNC reconstruction should ideally suppress the iodine contrast agent completely, but not the calcifications. The results of the VNC algorithm for this phantom experiment did not meet these requirements: aside from the iodine contrast agent, the hydroxyapatite rings of the vascular phantom and – to a lesser extent – the hydroxyapatite inserts of the BDC phantom were suppressed as well. The hydroxyapatite rings of the vascular phantom were suppressed by 83.8–93.7%, the same order of magnitude as the suppression of the iodine contrast agent. Apparently, the attenuation profile of the hydroxyapatite rings is similar to that of iodine; this hypothesis is supported by the observation that ring 1, which consists solely of the Ecoflex silicone rubber, was suppressed by 99.7%. Although the molecular composition of the silicone rubber is unknown, this is not unlikely, seeing as how the manufacturer reports that Ecoflex is a platinum-cured silicone rubber [58]. After all, virtual non-contrast scans are typically based on two-material decomposition algorithms with water and iodine as basis materials and as such, heavier elements may be more similar to iodine than to water in terms of attenuation. This hypothesis is supported further by the observation that the attenuation of ring 1, which contained no CaHA, was over 200 HU prior to suppression, whereas the attenuation of water is 0 HU by definition.

The hydroxyapatite inserts of the BDC phantom were suppressed by 64.5 and 68.5% respectively. This can also be attributed to the fact that a two-material decomposition algorithm is used to generate the VNC scan. In using this algorithm, a fraction of the attenuation will be due to iodine and a fraction due to water; the iodine fraction is then subtracted, leading to partial suppression of the inserts. After suppression, the mean attenuation level of the 100 HA and 200 HA inserts is 53.1 and 93.0 HU respectively. These levels fall below the threshold of 130 HU used for scoring calcifications on non-contrast-enhanced CT scans according to the method by Agatston et al. [14]. Therefore, the VNC image of the phantom would have a quantitative calcium score of zero, which is clearly not representative of the hydroxyapatite present in the phantom. As such, further research should be conducted to investigate whether VNC scans can be used to reliably score the degree of calcification in PAD patients. The performance of VNC scan generation might be expected to be better for patient data. After all, calcifications in vivo have been reported to be denser than the densities used in the BDC phantom and the accuracy of material decomposition algorithms has been reported to increase with increasing densities of the basis materials [30]; Arnold et al. stated that calcifications in vivo may form focal deposits approaching the density of pure CaHA [59]. Furthermore, the feasibility of calcium scoring based on virtual non-contrast scans has previously been demonstrated for the coronary arteries [32,33].

The material decomposition analysis showed relatively good results for the BDC phantom: the calculated calcium density reflected the true density relatively well, especially after applying a slight correction by using the water-equivalent plastic as a basis material in the decomposition analysis instead of water. Presumably, whereas the CT_{WATER} represents the total attenuation of water well, the relative contribution of the photoelectric effect and Compton scattering differ slightly from real water, which would explain why the calcium density needs to be corrected.

The relatively poor performance of the VNC algorithm for the vascular phantom may be caused in part by the results of the material decomposition. As can be appreciated from figure 2.9, the hydroxyapatite rings mapped closer to the water/iodine line than to the water/CaHA line; this appears to confirm the hypothesis that the attenuation of the Ecoflex silicone rubber is similar to that of iodine. This may explain why the VNC algorithm failed to distinguish between the hydroxyapatite rings and iodine contrast agent, leading to both regions getting suppressed in the VNC image. Apparently, the attenuation profile of the Ecoflex silicone rubber is not representative of the attenuation profile of water, contrary to the water-equivalent plastic in the BDC phantom.

The results of the decomposition analysis for the vascular phantom may also have implications for the reliability of this method for calcium quantification in clinical practice. After all, the performance of this decomposition method relies on the assumption that the image volume can be expected to consist of water, iodine and CaHA. When this assumption does not hold true, the results obtained through the decomposition analysis may not be valid, as the results for the vascular phantom illustrate. Atherosclerotic plaques in vivo do not merely consist of water, calcification and iodine, but may also contain lipid, fibrous and hemorrhagic components [60,61]. These different plaque components may distort the calculated calcium density on application of this method to patient data, although the magnitude of this distortion may be smaller than that seen for the Ecoflex. After all, the volume of the atherosclerotic plaques is smaller than the volume of the hydroxyapatite rings in the phantom and calcifications in vivo typically appear as relatively isolated masses, whereas the hydroxyapatite was mixed with the Ecoflex in the phantom. Nevertheless, the accuracy of this method for calculating calcification density in vivo should be validated in further experiments by comparing calculated calcium densities to reference values obtained through histopathologic analysis. Samples which could be considered for such analysis include atherosclerotic plaques obtained at endarterectomy surgery, such as in the Athero-Express study, or cadaveric samples [61]. Such comparison between calculated calcium density values and reference values obtained through histopathological analysis may allow for calibration of the three-material decomposition algorithm. Replacing water with a specific material representing atherosclerotic plaques based on this comparison, should this prove necessary, may yield more accurate results for the calculated calcification density. This was observed in the decomposition analysis of this phantom experiment, where slight correction of the calcium density calculated for the BDC phantom yielded more representative values. However, histopathologic analysis of calcification density can be time-consuming and laborious; as such, it remains to be seen whether such analysis is feasible or other validation strategies should be employed.

Conclusion

The objective of this phantom experiment was to investigate the performance of VNC scan generation and the quantification of calcification density based on dual-energy data. The VNC algorithm adequately suppressed the iodine contrast agent to the same attenuation as water. The hydroxyapatite inserts of the validated BDC phantom were also suppressed to some extent, falling below the threshold of 130 HU used for calcium scoring. Further research should therefore investigate whether VNC scans can be used to reliably score the degree of calcification in patient data.

The calcium density of the hydroxyapatite inserts of the BDC phantom was accurately calculated using material decomposition analysis, especially after slight correction for CT_{WATER}, the phantom's base material. The hydroxyapatite rings of the vascular phantom were found not to be representative of CaHA in water, mapping closer to the reference data for iodine. This may have implications for calcium density quantification in vivo, as atherosclerotic plaques consists of several components other than blood, iodine and CaHA. Further research should validate the performance of calcium density quantification in patient data, preferably by comparison to histopathologic data. If necessary, the material decomposition algorithm should be calibrated to account for these plaque components.

Chapter 3 – Segmentation of calcifications based on dual-energy CTA

Introduction

In the preceding chapters, the case was made that standardization of calcium scoring methods is desired to facilitate comparison between research results as well as application in clinical practice. An automatic calcium scoring algorithm may be preferable, to increase reproducibility and limit the time required for the work-up of a single patient. To achieve this, segmentation of calcifications is a necessary first step. After all, before calcium scores can be calculated, the calcifications must be distinguished from surrounding tissues and materials, particularly the iodine contrast agent. As was mentioned in the introduction to the previous chapter, dual-energy CTA may be used to separate calcifications and iodine contrast agent based on differences in energy-dependent attenuation characteristics, either by means of generating a virtual non-contrast scan or through material decomposition algorithms. The results of the phantom experiment reported in Chapter 2 provided a first indication of the performance of these functions with regard to separation of calcification and iodine.

The results of the material decomposition algorithm appeared to be promising with regard to the ability of this algorithm to differentiate between calcifications and the iodine contrast agent: as can be seen from figure 2.9, the hydroxyapatite inserts of the BDC phantom can be readily distinguished from the iodine contrast agent, which mapped close to the iodine/water line. As was mentioned previously, the hydroxyapatite rings of the vascular phantom were not representative of a mixture of calcium hydroxyapatite and water and therefore, these should not be taken into consideration. However, while the hydroxyapatite inserts and contrast agent may be separated quite easily for the phantom experiment, it should be noted that the phantom represents a significant simplification of reality and that separation of calcifications and iodine on patient data may be more challenging. After all, calcifications in vivo typically present as focal deposits with varying densities and much smaller dimensions than the hydroxyapatite inserts in the phantom [59,62]. As a result, calcifications in patient data are likely to be more dispersed in the decomposition map, as opposed to the relatively localized point clouds seen for the phantom inserts. Moreover, because of the small dimensions of the calcifications and close proximity to the iodine contrast agent, partial volume effects may be expected to occur as well. This would result in some voxels containing both calcium and iodine, blurring the separation between these materials. Therefore, the performance of the aforementioned material decomposition with regard to segmentation of calcifications in patient data must be investigated further; this was another objective of this research project.

As an additional challenge, vascular calcifications in patient data must not only be separated from the iodine contrast agent, but also from other calcified tissues, of which bones are the most ubiquitous. Vascular calcifications are formed from calcium hydroxyapatite, the same compound that forms the mineralized component of bone [50]; as such, these structures cannot be separated based on energy-dependent attenuation characteristics alone. In addition to the material decomposition analysis, anatomical information is required to achieve an accurate segmentation of the vascular calcifications. This anatomical information can be integrated with the dual-energy data by segmenting the arteries, including the vascular wall with calcifications, prior to the material decomposition analysis. In this way, the vascular calcifications can first be separated from the bones of the vertebral column, pelvic girdle and lower extremities in the segmentation step, after which material decomposition analysis may be used to separate the calcifications from the iodine contrast agent.

Therefore, before the performance of material decomposition analysis with regard to segmentation of calcifications can be investigated in patient data, a method must be developed to segment the arteries, which this research project made an effort towards.

The VNC scan image generated for the phantom exhibited suppression of the contrast agent, but to some extent also of the hydroxyapatite inserts of the BDC phantom. This led to the mean attenuation of the inserts falling below 130 HU, the cutoff for calcifications in the quantitative scoring system according to Agatston et al. [14]. As a result, the phantom would have a quantitative calcium score of zero based on the VNC scan, which is clearly erroneous considering the hydroxyapatite present in the phantom. Although the VNC scan generation might be expected to yield better results for patient data, as was argued in the 'Discussion' section of Chapter 2, the value of this algorithm for calcium scoring in patient data must be investigated as well.

In summary, the objective of the patient data analysis, that will be described in this chapter, was twofold. The first aim was to develop a workflow for segmentation of the major arteries to serve as a preparatory step to the material decomposition analysis, thus integrating information on the patient anatomy and energy-dependent attenuation characteristics of different materials. The second objective was to evaluate the accuracy of two distinct methods, i.e. the material decomposition analysis and VNC scan generation, with regard to segmentation of calcifications.

The contents of this chapter will be as follows. First, the design considerations and performance requirements of the artery segmentation workflow and subsequent dual-energy analysis – the material decomposition analysis or VNC scan generation, respectively – will be discussed. Subsequently, the function of the artery segmentation workflow will be described, followed by the methods of the patient data analysis, which includes a description of the patient characteristics. The results of the individual steps will subsequently be reported, after which the strengths and limitations of the various workflow components and analyses will be discussed.

Methods

Design considerations

There are several performance requirements with regard to the artery segmentation workflow. First, the workflow should segment all patent arteries along a target arterial path, from the distal aorta up until the ankle, ideally while not including any bone into the segmentation. Within this context, the algorithm should be flexible to a wide range of variations in patient anatomy and peripheral arterial disease patterns. For instance, the predominantly elderly PAD patients might exhibit degenerative changes to the vertebral column, such as spondylolisthesis, potentially leading to close proximity between vascular calcifications in the aorta and any protruding vertebrae. Furthermore, PAD patients may present with different peripheral arterial disease patterns, including stenosis, occlusions and severe calcification; patients may also have received previous treatment for PAD, such as stenting or bypass surgery. Ideally, the segmentation algorithm would still be able to segment the target arterial path up to the ankle in spite of these diverse anatomic variations; in other words, the workflow should be robust.

Application of the workflow for risk stratification in clinical practice imposes several requirements on the algorithm as well. The time available for the work-up of a single patient is limited and therefore, the entire workflow leading to the segmentation of calcifications – i.e. segmentation of the arteries followed by material decomposition, or VNC scan generation – should be relatively fast; as a somewhat arbitrary goal, 15 to 30 minutes seems like a reasonable target. To achieve this, a (semi)automatic segmentation algorithm would be preferable. Furthermore, as the planning of interventions for PAD is performed by clinicians, who may not necessarily be trained in medical image analysis, the workflow should be as reproducible as possible while requiring as little user interaction as possible. This further underlines the preference for a (semi)automatic algorithm.

Finally, there are requirements to the accuracy of the calcification segmentation in terms of size and distribution. Although the size at which individual calcification deposits become clinically relevant, e.g. in terms of periprocedural outcomes, is not exactly known, the results of the systematic review did show several aspects of calcification associated with poor outcomes. Bilateral calcification of target vessels was shown to be associated with lower rates of technical success and primary patency after endovascular treatment. As such, the calcification segmentation should be able to visualize this for any artery, if present. The crural arteries, which are the most distal and therefore the smallest arteries along the target arterial path, have been reported to have diameters between 2 and 4 millimeters [63]. Therefore, for the workflow to discern bilateral calcification, it should have a minimal resolving power of about 2 millimeters. As such, this will be the target accuracy for the complete segmentation workflow. Of course, statistical analysis in future research should reveal whether calcification scores calculated with such accuracy have adequate predictive value, or whether more strict targets are required. An as additional requirement to the workflow accuracy, the segmentation of calcifications should reflect the true distribution of calcifications across different arterial segments. In other words, calcifications within any individual should not be omitted from the segmentation due to their size or density. This may be especially important for the VNC scan generation, which has previously been shown to suppress calcification to values below the scoring threshold in the phantom experiment.

Artery segmentation workflow

The artery segmentation workflow was implemented in MATLAB R2021b (MathWorks, Natick, MA, USA) and is semiautomatic. The pseudonymized CTA DICOM files were read into MATLAB, after which the CT numbers were rescaled to Hounsfield Units using parameters saved with the DICOM information struct. Both a lower and an upper threshold were subsequently applied on the image volume: the attenuation of all voxels having values <130 HU or >400 HU was set to be equal to the minimum value found in the image, which corresponds to air. Vessel enhancement filtering according to the method by Frangi et al. was applied next, using an implementation by D-J. Kroon [64,65]. In using this filter, the scale range (denoted by sigma) was set between 1 and 6 to ensure all arteries were enhanced. Finally, Fast Marching Method (FMM) segmentation according to the method by J.A. Sethian was performed within the vessel-enhanced image volume to isolate the arteries from surrounding boosted structures [66]; the functions '`grayweightdiff`' and '`imsegfmm`', available within MATLAB's Image Processing Toolbox, were used for this. To initialize the algorithm, the user has to place a seed point within the aorta on the first axial slice in the CTA volume. The function '`grayweightdiff`' then computes a weight for every voxel, which is the difference between the voxel value and a reference value, which was defined as the value of the seed point voxel. The function '`imsegfmm`' then performs FMM segmentation starting from the seed point based on the voxel weight map. A threshold must be set for '`imsegfmm`', which is a value between 0 and 1 and can be seen as the sensitivity of the algorithm. After the FMM segmentation, the result is written to the NIfTI (Neuroimaging Informatics Technology Initiative) format to allow analysis with the material decomposition algorithm implemented in Python by A. Schilham [47].

The full MATLAB script, with comments, can be found in Appendix 3-A of this chapter.

Analysis

The performance of the artery segmentation workflow, material decomposition analysis and virtual non-contrast scan generation was tested on lower extremity CTA scans of six patients, which were available retrospectively. These scans were performed on the Philips IQon Spectral CT scanner (Philips Healthcare, Best, The Netherlands) using the standard protocol; the settings of this protocol are shown in Table 3.1. Automatic tube current modulation was applied; the tube current value given in table 3.1 represents the reference value. The images were reconstructed with 3 mm slice thickness and 3 mm slice spacing; these reconstruction parameters are also standard in the quantitative scoring method by Agatston et al. [14,15]. An attempt was made to analyze the thin-slice reconstructions (Axial 0.9/0.7) as well, as reconstructions with thinner slices may be less susceptible to partial volume effects. However, these scans could not be used, as MATLAB ran out of working memory on the vessel enhancement filtering operation.

Table 3.1: The scan parameter settings for the lower extremities' CTA protocol on the Philips IQon scanner, as used for the patients included in the analysis.

Scan parameter	**Setting**
Scan direction	Craniocaudal
Scan option	Helical
Tube potential (kV)	120
Tube current (mAs)	146*
Pitch	0.797
Rotation time (s)	0.75
Reconstruction	Axial 3/3 (CTA); Axial 1/1 (VNC) †
Resolution	Standard
Reconstruction kernel	B
Reconstruction algorithm	iDose (6)

Abbreviations: kV, kilovolt; mAs, milliampere-seconds; s, seconds.

* This is a reference value; as automatic tube current modulation was applied, the actual tube current varied per patient.

† These parameters denote slice thickness and slice interval, respectively.

Six patients with different characteristics were selected for the analysis, in order to investigate the robustness of the artery segmentation workflow. The investigated aspects included different levels of average contrast enhancement, peripheral arterial disease patterns and previous treatments for PAD. The patient characteristics are summarized in Table 3.2. The mean aortic attenuation shown in the table was determined in Philips IntelliSpace Portal by placing a circular region of interest within the aorta in five different slices and averaging the results. The number of crural vessels which can be discerned on visual inspection of the CTA images is also given, to serve as comparison for the arterial segmentation results. The artery segmentation workflow was developed using the CTA scan of patient 1, as this patient had relatively patent vessels, aside from an occlusion of the right superficial femoral artery. The workflow was then tested on the CTA scans of the other patients. The performance of the artery segmentation workflow was investigated through visual inspection.

Table 3.2: Characteristics of the patients included in the patient data analysis.

Patient number	**Sex & age**	**Patient characteristics**	**Mean aortic HU**	**Number of crural vessels visible (left/right)**
1	M45	Occlusion of right SFA; no significant atherosclerosis and limited calcification.	255	3/0*
2	F65	Suspected PAD. Extensive calcifications, no significant stenosis or occlusions.	349	3/3

3	F63	PAD F2b, left side. Occluded stent in CIA and patent aortoiliac bypass, both on the left side. No significant stenoses; moderate calcification.	268	2/2
4	F63	Previous PAD F2b, bilateral; treated with stents in both CIAs, both patent on this control CTA. No stenoses; moderate calcification.	574	3/3
5	M79	PAD F2b, bilateral. Extensive calcification; multiple short, significant and heavily calcified stenoses on both sides.	255	3/3
6	F75	PAD F2b, bilateral. Focal stenosis in the left CIA and right EIA; no stenosis otherwise. Moderate calcification.	492	3/3

Abbreviations: SFA, superficial femoral artery; PAD, peripheral arterial disease; CIA, common iliac artery; F2b, Fontaine 2b; EIA, external iliac artery; HU, Hounsfield Units.

* Because of proximal occlusion of the SFA.

Material decomposition analysis was performed on the voxels included in the artery segmentation mask, according to the aforementioned method by Alvarez and Macovski and using an implementation in Python written by A. Schilham [43,47]. Three-material decomposition analysis was performed for all voxels located within the blood-iodine-CaHA calibration triangle on the decomposition plot, yielding volume fractions for each of these three materials for every voxel. Voxels with CaHA volume fractions above a certain threshold were segmented as calcifications; thresholds of 0.01, 0.02, 0.03, 0.05 and 0.07 were attempted respectively. The resulting calcification segmentation was compared to the original CTA scan by means of visual analysis in the ITK-SNAP software package, which was developed by Yushkevich et al. [67]. Special attention was given to the performance of the algorithm around metallic implants such as stents. After all, these represent a violation of the assumption underlying the three-material decomposition analysis, that the image volume only consists of blood, iodine and CaHA.

VNC scans were generated for each of the five patients using Philips IntelliSpace Portal software version 12.1 (Philips Healthcare, Best, The Netherlands). The VNC scans were exported, after which calcifications were segmented semiautomatically based on the method described by Agatston et al. [14]. The VNC scans were first thresholded at an attenuation of 130 HU in MATLAB to yield a segmentation mask. The segmentation mask was then loaded into ITK-SNAP together with the VNC scan [67]. Voxels in the segmentation mask located over relevant arteries were assumed to correspond to vascular calcifications and were selected manually (i.e. converted to another segmentation label) using the 'brush' tool. Calcifications in arteries up to the ankle, consistent with the concept of the 'target arterial path', as defined in the GLASS system, were included [2]. This includes the aorta and the common iliac artery, external iliac artery, common femoral artery, superficial femoral artery, popliteal artery and crural arteries (anterior and posterior tibial artery and peroneal artery) in both limbs. Furthermore, calcifications in the internal iliac artery and deep femoral artery up until the first bifurcation in these respective arteries were also included. Conversely, calcifications in the visceral arteries, insofar these were visible on the CT scan, were not included, as these are not relevant within the context of PAD. To account for noise, only regions of interest with an area >1 mm^2 (two contiguous voxels within the axial plane, based on 8-connectivity) were included in the segmentation, in accordance with the method by Agatston et al. [14]. Metallic stents and operative clips were avoided as much as possible.

Arterial calcifications were segmented on the conventional CTA reconstruction as well, to serve as comparison for the dual-energy based segmentations. Calcifications were segmented in MATLAB and

ITK-SNAP using the same method described for the VNC scans, using, an alternate threshold of >350 HU to account for the contrast agent, as described by Mühlenbruch et al. [27] However, for patients 2, 4 and 6, who exhibited relatively high levels of contrast enhancement (as seen in Table 3.2), this led to considerable inclusion of voxels corresponding to contrast agent. Therefore, a higher threshold was used for these patients instead, set at 100 HU above the mean aortic attenuation shown in Table 3.2.

For each of the segmentations, calcium volume scores were determined. Additionally, the Dice similarity coefficient was calculated to compare the material decomposition and VNC segmentations with the segmentation based on conventional CTA [68]. It should be noted that the VNC scan was reconstructed by the Philips IntelliSpace Portal software with a different slice thickness and slice interval, as shown in Table 3.1. Therefore, the CTA segmentation was triplicated along the z-axis to reach the same matrix size as for the VNC scan, allowing comparison by means of the Dice similarity coefficient.

Results

Artery segmentation

All six CTA scans were segmented with the developed artery segmentation algorithm. Several parameter settings had to be varied slightly to achieve optimal results for every patient; the settings for each patient are shown in Table 3.3. Patients 4 and 6 exhibited mean contrast enhancement surpassing the default upper threshold of 400 HU, as shown in Table 3.2; as such, higher upper thresholds had to be chosen for these patients. For patient 6, an upper threshold of 600 HU was found to produce good results. For patient 4, the upper threshold had to be eliminated entirely, in part due to the stents in both common iliac arteries, which showed attenuation values as high as 2700 HU.

The vesselness constant C, which according to the help text for the vessel enhancement filter function written by D-J. Kroon denotes the threshold between the eigenvalues of noise and the vessel structure, had to be varied as well; after all, this threshold is dependent on the mean contrast enhancement of the vessels. Finally, the weight threshold of the FMM segmentation was varied as well, balancing pruning of the distal vessels with inclusion of structures other than the arteries.

Table 3.3: The segmentation parameters used for each of the patients included in the analysis.

Patient #	**Thresholding levels**	**Vessel enhancement filtering**	**Fast Marching Method**
		Vesselness constant C	Threshold
1	>130 & <400 HU	40	0.010
2	>130 & <400 HU	120	0.020
3	>130 & <400 HU	60	0.015
4	>130 HU	120	0.022
5	>130 & <400 HU	40	0.012
6	>130 & <600 HU	120	0.013

Abbreviation: HU, Hounsfield Units

The segmentation results for the six patients are shown in Figures 3.1 through 3.6. As can be appreciated from these figures, the algorithm successfully segmented most of the relevant arteries – i.e. the arteries along a TAP to the foot – for every patient. In patients 3 and 5, two and one crural arteries were missed respectively; in patients 1 and 6, two and one crural arteries respectively were shortened slightly in the segmentation. Aside from these cases, all crural arteries were segmented completely.

Figure 3.7 visualizes the segmentation for patient 5 as an overlay over the original CTA volume; the segmentation shown as an isosurface in figure 3.5 can be observed to correspond to the arteries. The segmentation is shown to be quite wide, including a significant margin of soft tissue around the arteries. This was observed for all patients and appeared to be especially pronounced in areas where the arteries run more or less horizontally.

As can be inferred from the results for patients 3 and 4, the algorithm also adequately segmented the vascular system in the presence of a bypass or patent stents; these structures were included in the segmentation. The occluded stent located dorsomedial to the aortoiliac bypass in patient 3 was partially included in the segmentation. The algorithm also segmented past severe calcification, as in patient 5, or significant stenoses, as in patient 6; the segmentation relative to the most significant stenosis is highlighted in figure 3.8. However, as can be seen from the result for patient 1, the algorithm did stop at occlusions.

Although the arteries up to the ankle are segmented in every case, some differences can be observed between different patients. In patients 2 and 4, some leakage of the FMM region growing algorithm into bony structures such as the spine, hip and distal femur occurred. The segmentations for patients 4 through 6 include several side branches not relevant to the clinical practice of PAD; in patient 6, side branches as high as the superior mesenteric artery and renal arteries were included.

Material decomposition analysis and VNC scan generation

Patient 1 had to be excluded from the dual-energy analyses, as there were no spectral data files available for this patient; the remaining five patients were analyzed successfully.

Figure 3.9 contains an example of a material decomposition plot, which was generated by including the voxels in the artery segmentation mask of patient 4. Relatively distinct point clouds can be discerned for soft tissue (indicated with a white arrow), iodine contrast agent (around the orange line) and calcifications (around the purple line). Additionally, there are numerous points dispersed around and between the blood-I and blood-CaHA lines, the location of which is roughly indicated by the red polyon.

Figure 3.10 illustrates the segmentation of calcifications using three-material decomposition and different CaHA volume fractions, based on the same decomposition plot for patient 4 as shown in figure 3.9. The points shown in red for any given threshold are segmented as calcifications.

A montage of the material decomposition segmentation result for patient 5 is shown in figure 3.11. The segmentation can be observed to follow the vascular calcifications quite well. However, the denser core of several calcifications can be observed to be excluded from the segmentation, an effect that was observed to some extent for every patient analyzed.

The performance of the material decomposition segmentation around stents was analyzed in patient 4, who had received bilateral stents in the common iliac arteries, the results of which are shown in figure 3.12. As can be appreciated from the frames of this figure, the stents are correctly excluded from the segmentation. Some voxels within the stents are shown to be included in the segmentation; it is unclear whether these voxels correspond to calcification or contrast agent.

An example of VNC scan generation, using data from patient 5, is shown in figure 3.13. Examining the aorta, which is indicated with the red arrowhead, the VNC algorithm can be observed to suppress the iodine contrast agent. Vascular calcifications and bone tissue are not visibly suppressed.

Volume scores of the conventional CTA, material decomposition and VNC calcification segmentations are given in Table 3.4. The material decomposition and VNC segmentations were compared to semiautomatic segmentation of the conventional CTA scans using Dice similarity coefficients; these results are shown in Table 3.5.

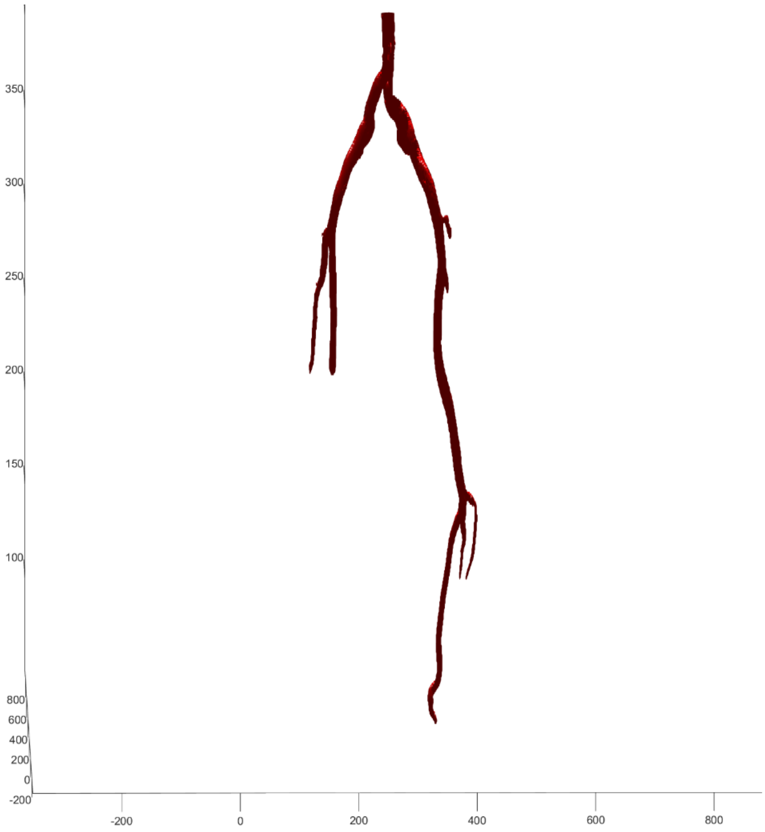

Figure 3.1: Isosurface showing the arterial segmentation for patient 1.

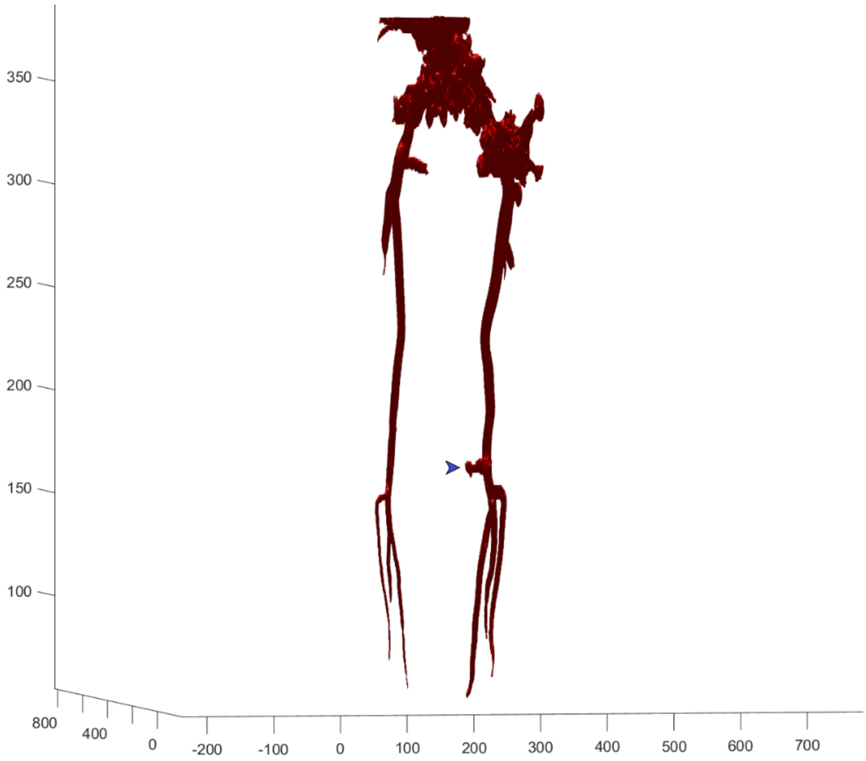

Figure 3.2: Isosurface showing the arterial segmentation for patient 2. Parts of the spine and hip are included in the segmentation, as well as a bit of the distal femur, which is indicated with the blue arrowhead.

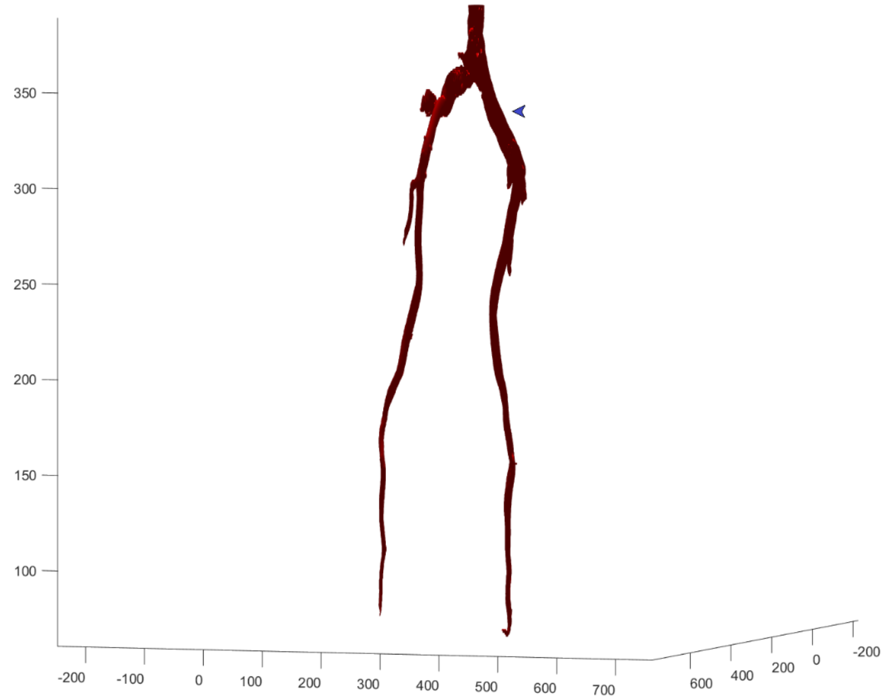

Figure 3.3: The arterial segmentation for patient 3. The aortoiliac bypass, indicated by the blue arrowhead, was included in the segmentation. The occluded stent in the left common iliac artery, which was located immediately dorsomedial to the bypass, was partially included.

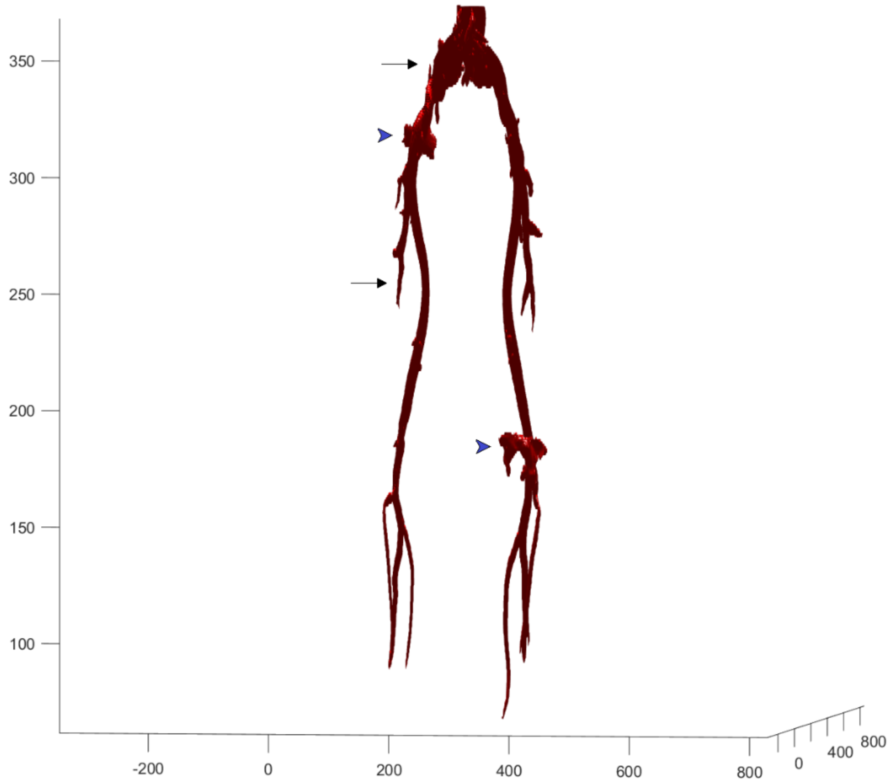

Figure 3.4: The arterial segmentation result for patient 4. All visible arteries along the TAP are included. However, there was some leakage into the hip and distal femur (blue arrowheads). Several side branches not on the TAP, such as the internal iliac artery and deep femoral artery (shown with black arrows), were also included.

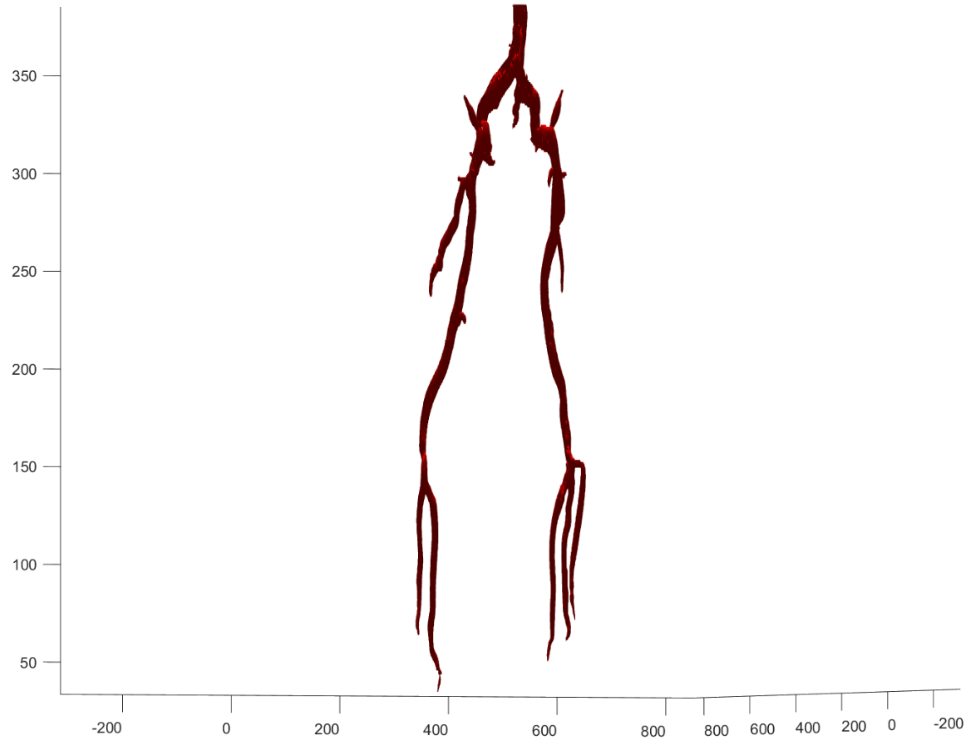

Figure 3.5: The arterial segmentation for patient 5. The arteries are segmented nicely without any leakage into surrounding structures. However, one crural vessel in the right leg was missed.

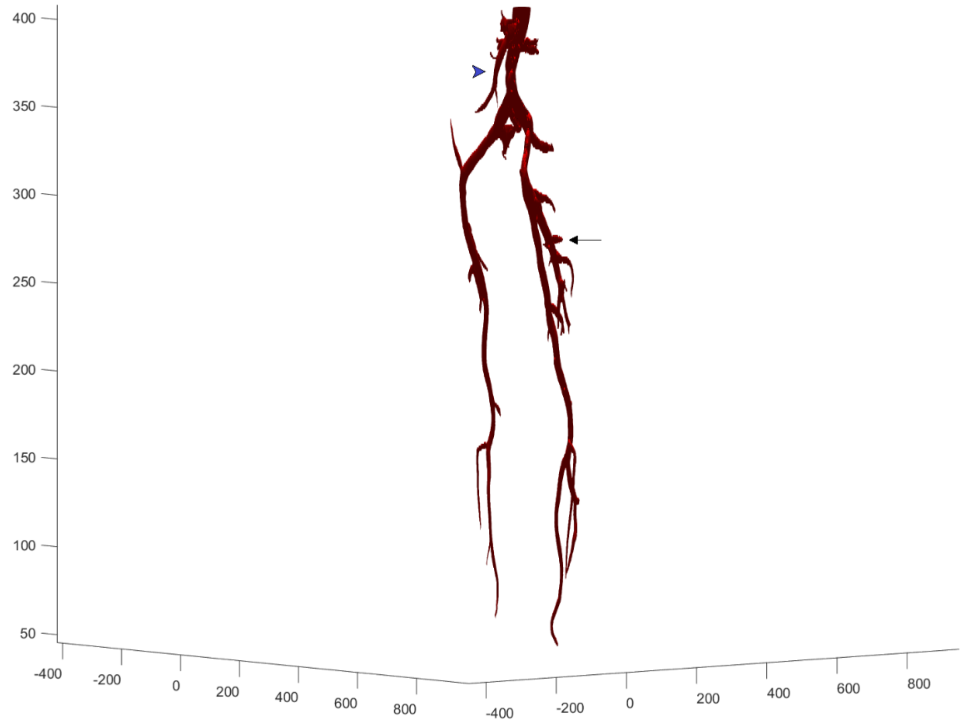

Figure 3.6: The arterial segmentation for patient 6. Several side branches were included in the segmentation, including the renal arteries, superior mesenteric artery (blue arrowhead) and profundal femoral artery (black arrow). Although not well visible in this view, some leakage into the sacrum from the right internal iliac artery was also observed.

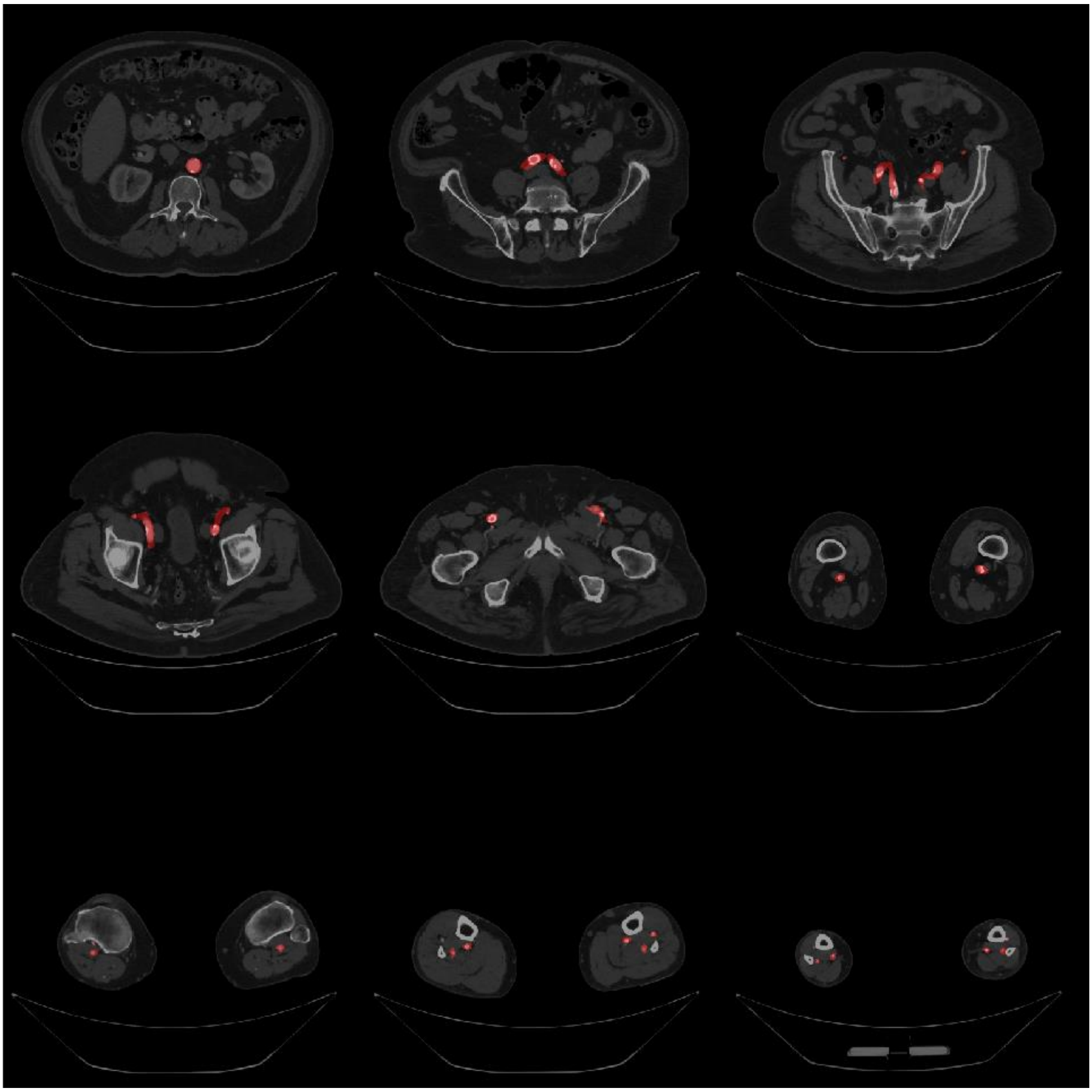

Figure 3.7: Montage of nine slices from the CTA scan of patient 5, with the segmentation shown as an overlay. The segmentation is shown to correspond to the arteries. A significant margin of soft tissue is included in the segmentation in some slices, such as the middle-left image.

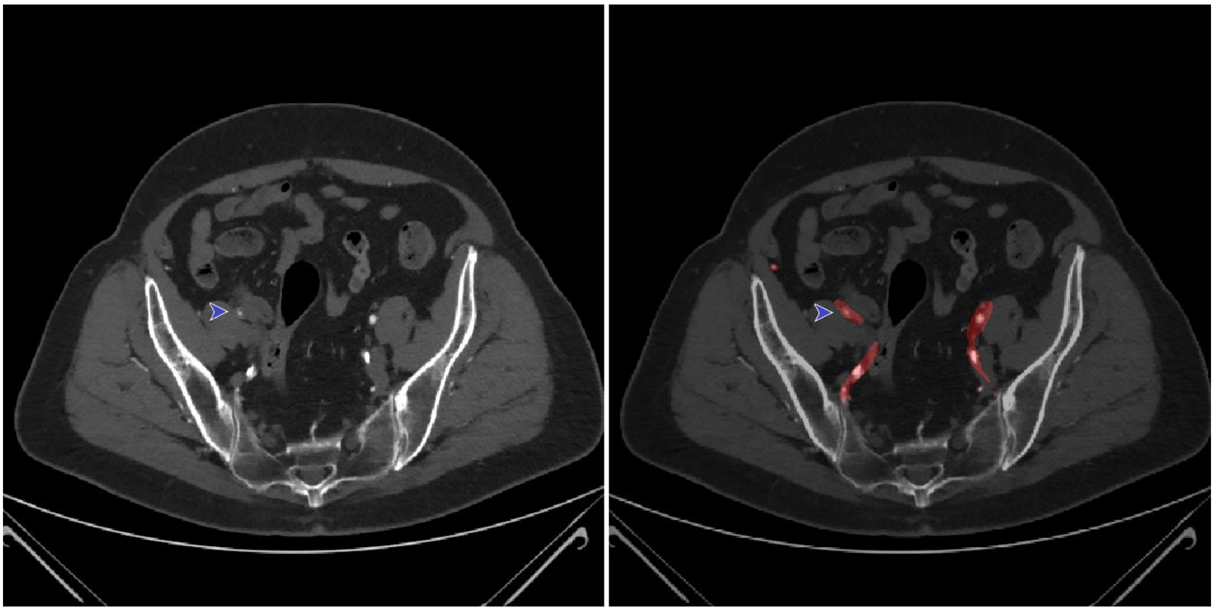

Figure 3.8: The performance of the artery segmentation algorithm with regard to significant stenosis. Left: An axial slice from the CTA of patient 6, showing a significant stenosis in the right external iliac artery (blue arrowhead). Right: The same axial slice with the arterial segmentation shown as an overlay. As can be seen, the algorithm manages to segment past the stenosis.

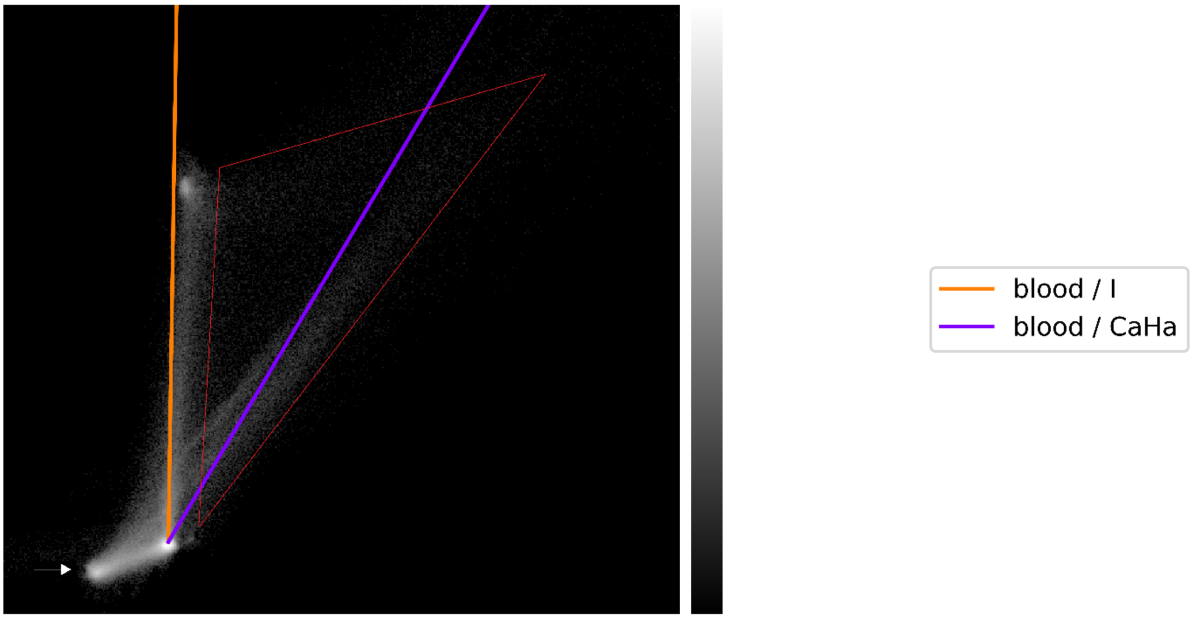

Figure 3.9: The material decomposition plot for patient 4, generated using the Python script written by A. Schilham [47]. The X-axis contains the Compton scattering contribution and the Y-axis contains the contribution of the photoelectric effect; the greyscale denotes the number of counts for any point in the diagram. The point cloud indicated by the white arrow corresponds to soft tissue around the arteries (e.g. fat and connective tissue). The orange and purple lines represent the reference values for increasing concentrations of iodine (I) in blood and calcium hydroxyapatite (CaHA) in blood, respectively [56]. In addition to the relatively distinct point clouds for soft tissue, iodine contrast agent and calcifications (the latter two around the respective reference lines), there are numerous points dispersed between the orange and purple lines. These points are difficult to observe with these window settings, but roughly fall within the area indicated by the red polygon.

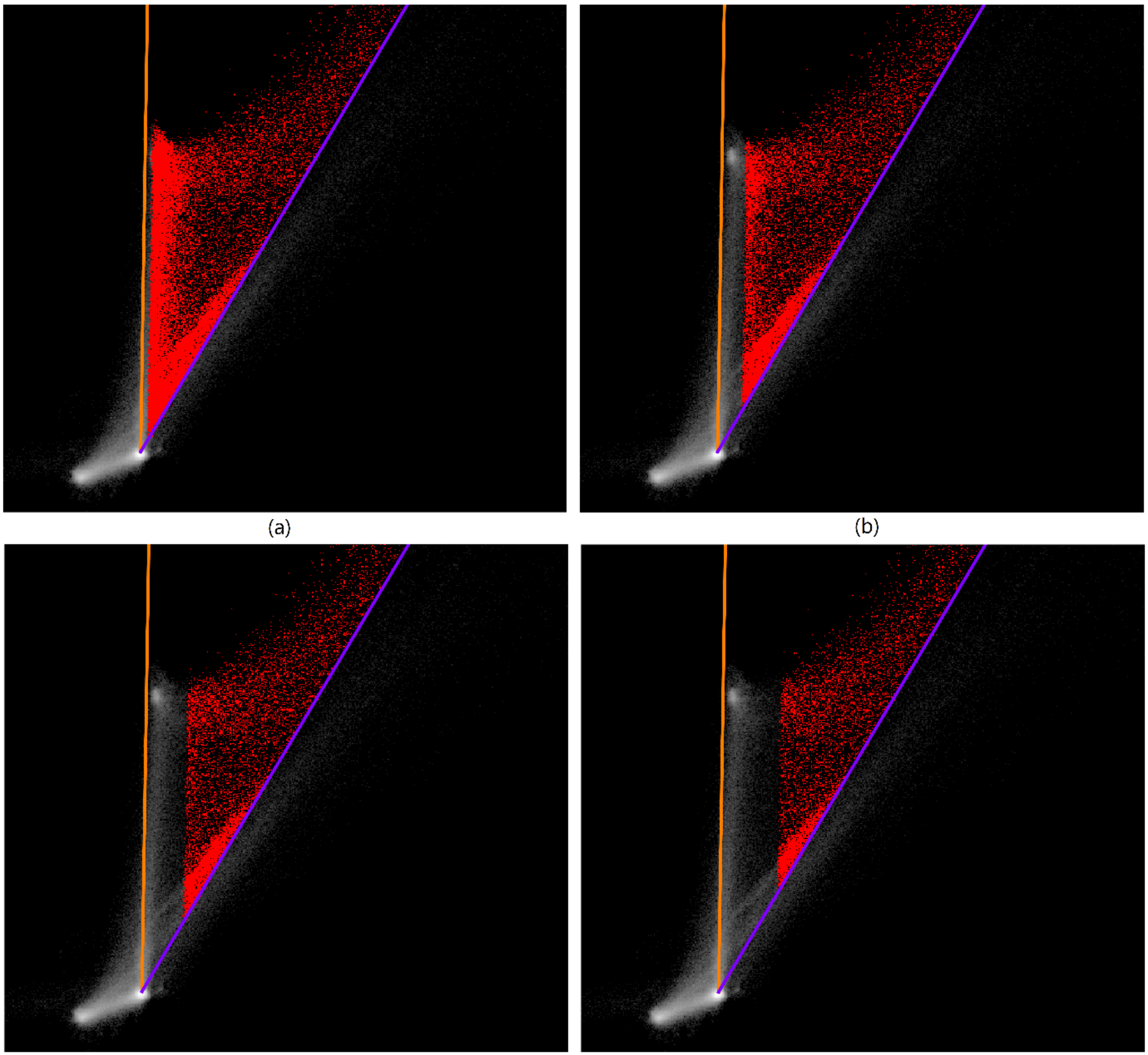

(a) (b) (c) (d)

Figure 3.10: Segmentation of calcifications based on material decomposition using the Python implementation written by A. Schilham [Schilham]. Three-material decomposition was performed on voxels within the blood-iodine-CaHA calibration triangle, formed by the orange and purple lines. Voxels with a CaHa volume fraction above a certain threshold were segmented as calcifications; these voxels are shown as red in the figures above. Shown are the results of patient 4 for thresholds of 0.01 (a), 0.03 (b), 0.05 (c) and 0.07 (d). The result for the threshold 0.02, which was also attempted, is not shown.

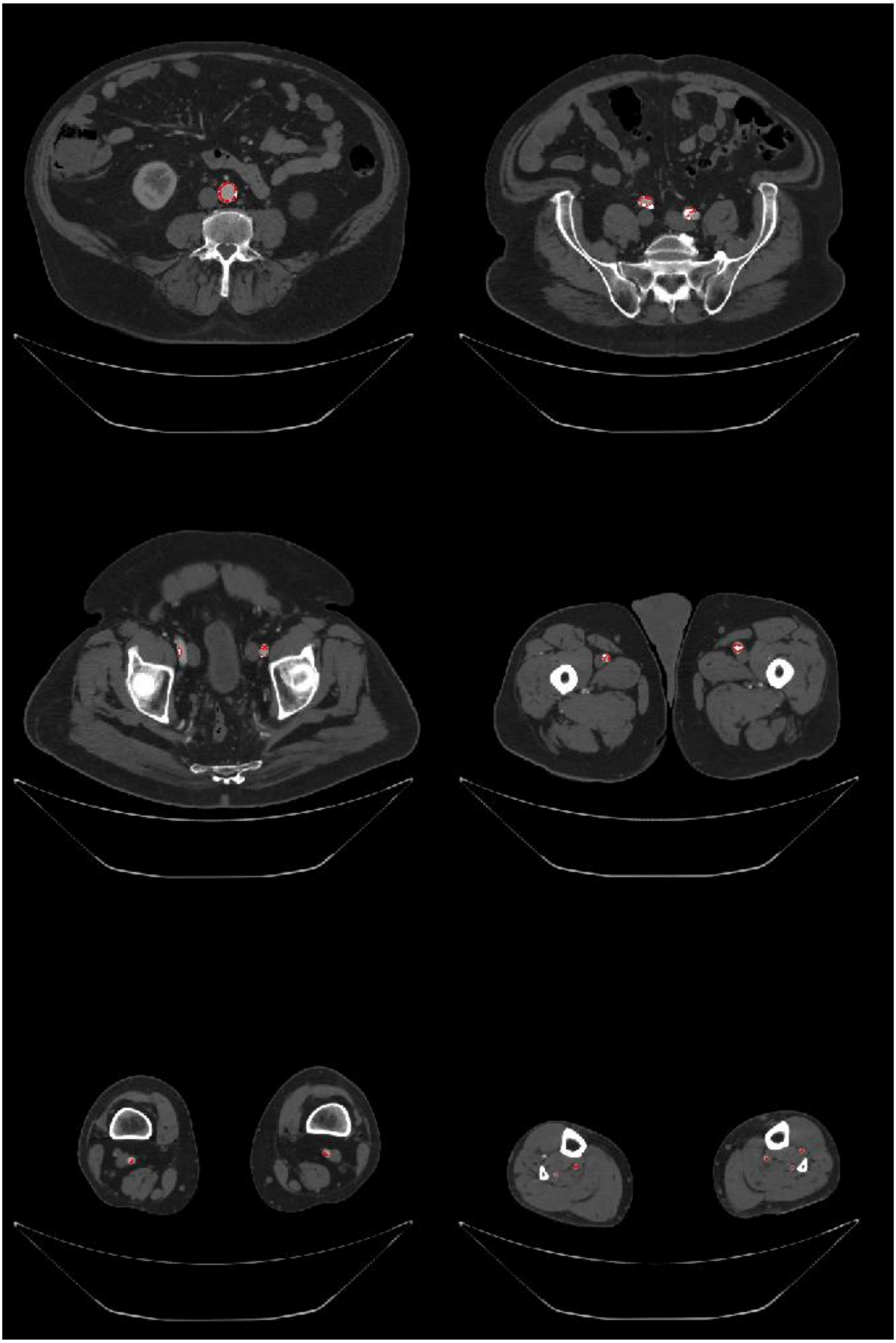

Figure 3.11: Montage of the result of calcification segmentation with the material decomposition algorithm for patient 5 [47]. The segmented calcifications are shown in red.

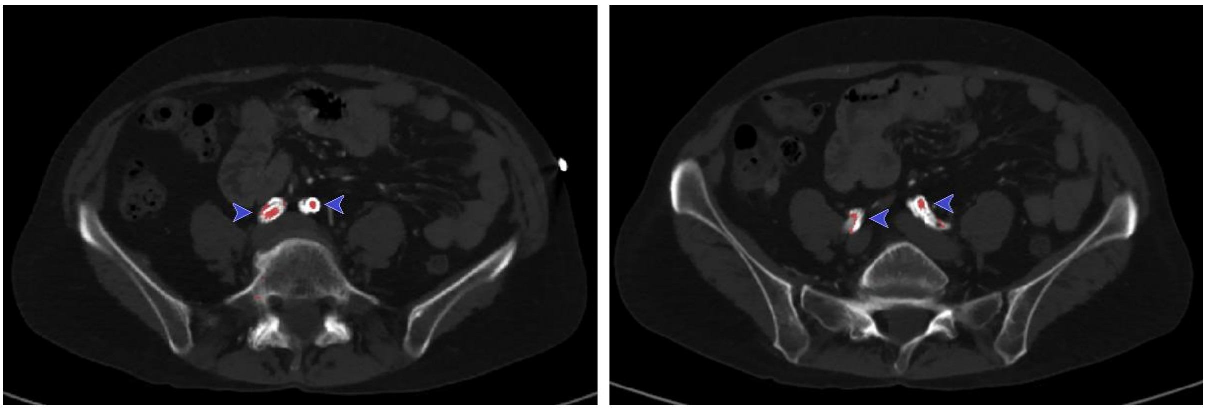

Figure 3.12: Two different axial frames of the CTA scan from patient 4, showing the performance of the material decomposition algorithm around bilateral stents in the common iliac arteries. The stents, which appear as white tubular structures and are indicated with blue arrowheads, can be observed to be excluded from the calcification segmentation, shown in red. Some voxels within the stents are shown to be included in the segmentation; it is unclear whether these voxels correspond to calcification or contrast agent.

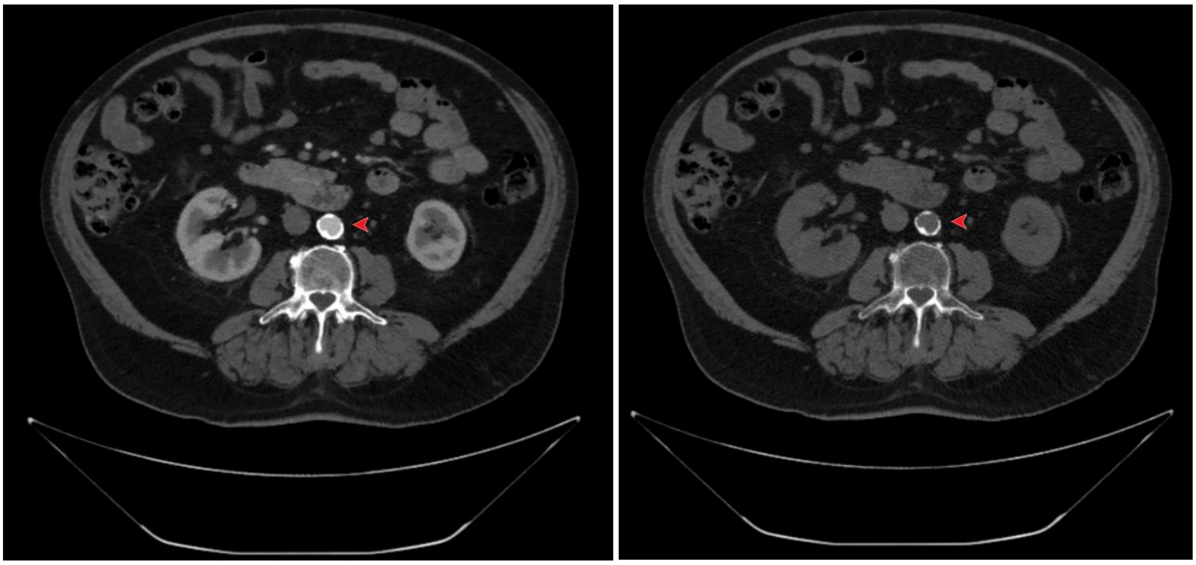

Figure 3.13: Example of VNC scan generation using the Philips IntelliSpace Portal software. One axial slice of the conventional CTA scan (left) and VNC scan (right) of patient 5 is shown. As can be seen from the aorta (indicated with the red arrowhead), the VNC algorithm suppresses the contrast agent, while calcified tissues such as vascular calcifications and bone tissue are not suppressed.

Table 3.4: Volume scores (in mm^3) of the conventional CTA, material decomposition and VNC scan calcification segmentations.

Patient #	**Conventional CTA**	**Material decomposition (CaHA fraction threshold)**					**VNC scan**
		0.01	**0.02**	**0.03**	**0.05**	**0.07**	
2	9444	73251	50981	37311	19700	9722	10058
3	14153	56909	26264	17358	10091	6595	12734
4	9514	67780	42783	31232	19664	13733	11696
5	52005	93100	64349	48602	30954	20073	51526
6	66208	80652	47113	31466	17680	12362	18962

Abbreviations: CTA, computed tomography angiography; CaHA, calcium hydroxyapatite; VNC, virtual non-contrast.

Table 3.5: Dice similarity coefficients comparing the segmentation results of the material decomposition algorithm (with different CaHA volume fraction thresholds) and the VNC scan respectively with the conventional CTA scan segmentation.

Patient #	**Conventional CTA threshold**	**Material decomposition (CaHA fraction threshold)**					**VNC scan**
		0.01	**0.02**	**0.03**	**0.05**	**0.07**	
2	**450 HU**	0.1861	0.2528	0.3198	0.4716	0.6267	0.7882
3	**350 HU**	0.2586	0.4530	0.5715	0.6285	0.5447	0.7227
4	**680 HU**	0.1939	0.2583	0.3012	0.3979	0.4849	0.6079
5	**350 HU**	0.4022	0.4992	0.5675	0.6146	0.5251	0.8198
6	**600 HU**	0.2060	0.3175	0.4115	0.5593	0.6402	0.7066

Abbreviations: CTA, computed tomography angiography; CaHA, calcium hydroxyapatite; VNC, virtual non-contrast; HU, Hounsfield Units.

Discussion

The objective of this patient data analysis was to develop a calcification segmentation workflow, using either material decomposition analysis or VNC scan generation, and to evaluate the accuracy of these methods for calcification segmentation; with regard to the former, an arterial segmentation algorithm was written as a preparatory step to the material decomposition analysis.

The arterial segmentation workflow was shown to adequately segment the vascular system for all patients; all arteries up to the ankle were segmented, with the exception of a few relatively gracile crural arteries that were missed for patients 3 and 5 and shortened for patients 1 and 6. Additionally, the algorithm was shown to be robust to a wide range of PAD patterns, such as stenosis and severe calcification, and previous interventions, including stenting and bypass surgery. The in-stent occlusion in patient 3 was only partially included in the segmentation, although this may be caused by the overlying bypass. Further testing of the algorithm should clarify whether the algorithm includes in-stent occlusion or restenosis in other patients. The algorithm was also observed to be relatively fast, requiring about 10 to 15 minutes to segment a single patient, including only a few minutes of user interaction.

Considering these results, the performance of the arterial segmentation workflow seems adequate in light of the clinical requirements. However, several limitations were observed as well, which might be addressed with further improvements to the algorithm.

First, the limited working memory of the hardware that was used required the use of the 'Axial 3/3' reconstruction; although this is also standard in coronary artery calcium scoring, as introduced by Agatston et al., this may be suboptimal [14]. After all, use of a CTA reconstruction with larger slice thickness may introduce partial volume effects, potentially introducing variability into the calcification quantification [35]. However, the use of thin-slice reconstructions also has disadvantages, as the increased noise levels on these reconstructions may also introduce inaccuracy. Further research should examine the effect of the reconstruction used on calcium scores and their relationship with clinical outcomes.

Secondly, although the semiautomatic segmentation algorithm was designed to require little user interaction, only calling for placement of a single seed point, in practice several parameters of the algorithm had to be fine-tuned considerably, as is reflected by Table 3.3. This was because a trade-off was observed between complete segmentation of the smallest vessels, particularly the crural vessels, and leakage into bony structures. Significant leakage into the spine, hip and distal femur was observed for patient 2 and – to a lesser extent – patients 4 and 6. The leakage may be explained by the observation that the vessel enhancement filter did not only boost the contrast-enhanced arteries, but also tubular structures within bones; as such, in cases where the arteries were located in close proximity to these bones and had similar intensities, the FMM algorithm included these structures as well, explaining the leakage. This seemed to occur more frequently in scans with higher mean contrast enhancement, as can be appreciated when comparing the segmentation results with Table 3.2. Such leakage into osseous structures was difficult to eliminate, as changes in the algorithm parameters to decrease such leakage inevitably lead to loss of small vessel structures from the segmentation. The leakage represents a problem for the subsequent material decomposition analysis, as the inclusion of the hydroxyapatite-containing bone tissue erroneously increases the calcium scores for these patients. As such, further development of the artery segmentation algorithm is warranted to diminish such leakage. This aspect of the workflow might be improved if the vessel enhancement filter is only applied to smaller vessels, by choosing a narrower range for the filter scale sigma. These settings might lead to less enhancement of the bones, which are larger than the arterial segments under consideration, while maintaining the performance for the crural vessels. Furthermore, this would also decrease the working memory the algorithm requires, which may allow thin-slice CTA reconstructions to be tested. In this case, the larger arteries, such as the aorta and iliac arteries, should be included in the segmentation by applying the FMM algorithm without the prior vessel enhancement step; inserting a morphological closing step with a large kernel before the FMM algorithm instead may ensure that the large arteries are separated from the spine and hip bones. As an alternative solution, the dual energy information could be used to obtain more accurate segmentations as well. Application of a calcium suppression algorithm, which dual-energy CT imaging enables, could remove the bones from the scans prior to segmentation and thus reduce leakage into other structures [37,38,40]. Unfortunately, this was not attempted due to limited access to the Philips IntelliSpace software; however, this solution may yield promising results as well. If the influence of bony structures on the segmentation could be diminished in this manner, the algorithm can be expected to become more robust and require less fine-tuning of the algorithm parameters; in turn, this would increase the reproducibility and decrease the amount of user interaction required.

As a third limitation, the algorithm was shown to stop at occlusions, as can be seen from the segmentation result for patient 1. This may not be a problem for cases where the blood flow stops at the occlusion, but it may prove suboptimal for patients where there is distal pick-up through collateral arteries; due to the discontinuation of in-line arterial blood flow, these distal vessels are currently not included in the segmentation. In theory, inclusion of vessels distal of the occlusion could be achieved by placing additional seed points in these vessels, but this would lead to more user interaction. Further attention should be given to the question whether inclusion of vessels distal of occlusions is clinically relevant; if this turns out to be the case, further development of automatic methods to include these vessels would be advantageous.

Several segmentations were found to include side branches not on the TAP. Inclusion of these side branches may lead to inclusion of any vascular calcifications in these vessels, which would increase the calcium scores although these arteries are not relevant within the clinical context of PAD. Therefore, it would be preferable if these side branches could be eliminated. A potential method to implement this might be to perform skeletonization of the segmentation, followed by detection of bifurcations and selection of the arteries leading to the ankle. Such bifurcation detection would have the additional benefit of (semi)automatically dividing the segmented volume into different arterial segments, which would facilitate subanalysis of the calcium burden in specific segments.

Finally, while patients with different scan characteristics and PAD patterns were selected to test the robustness of the arterial segmentation algorithm, it should be noted that the patients investigated do not necessarily represent the most affected subgroup of PAD patients. The patients investigated all had Fontaine stage 2b PAD, indicating moderate to severe intermittent claudication; no patients with CLTI (roughly corresponding to Fontaine 3 or 4) were tested. While the performance of the segmentation algorithm with respect to significant stenosis and severe calcification was shown to be good, this performance should be confirmed within this more difficult patient group as well.

In summary, the arterial segmentation algorithm could still be improved in several ways. Nevertheless, the algorithm exhibited satisfactory performance in segmenting the arterial system and segmentation of the arteries was shown to be a feasible preparatory step to material decomposition analysis.

In the second part of the patient data analysis, the performance of material decomposition analysis and VNC scan generation with respect to calcification segmentation was investigated. To this end, segmentations based on these methods were compared with segmentations based on conventional CTA. When considering the performance of these dual-energy-based segmentation methods, it should be noted that the reference standard is imperfect. After all, previous research has shown that segmentation of calcification based on conventional CTA scans may lead to under- or overestimation of the extent of calcification, depending on the threshold chosen [26,27]. Therefore, a Dice similarity coefficient below 1 – which would indicate perfect overlap – should not necessarily be attributed to failure of the dual-energy based method; this could also be caused in part by errors in the reference segmentation. Nevertheless, in the absence of a superior reference standard, comparison with segmentations based on conventional CTA should provide an initial indication on the performance of the dual-energy-based methods. Ideally, these methods based on DECT should be compared with the current golden standard – non-contrast-enhanced CT scans – in further research.

Judging from the Dice similarity coefficients shown in Table 3.5, the performance of the material decomposition algorithm with regard to calcification segmentation was moderate. Several factors may have contributed to the lack of overlap with the reference segmentations. First, the decomposition analysis was observed to exclude the core of denser calcifications. These excluded voxels are most likely represented by points to the right of the purple blood-CaHA line in figure 3.9, particularly near the top-right corner of the red polygon (at higher Hounsfield Units). After all, these points are close to the purple blood-CaHA line, but were not included as the decomposition analysis was limited to voxels within the blood-iodine-CaHA triangle between the orange and purple lines. The deviation of these points from the blood-CaHA line is most likely predominantly due to noise. Additionally, the composition of these voxels may differ somewhat from pure CaHA, as atherosclerotic plaques consist of different components [60,61]; this would lead to slight miscalibration of the blood-CaHA line with respect to these voxels. The material decomposition segmentation algorithm should be developed further in future research to achieve inclusion of these voxels in the core of calcifications. This should be feasible, either by including voxels outside of the calibration triangle by a certain margin or through recalibration of this triangle based on the data of multiple patients.

Secondly, suboptimal performance of the artery segmentation algorithm, which served as a preparatory step to the material decomposition analysis, may have led to poorer performance of the material decomposition analysis. After all, inclusion of osseous structures in the artery segmentation mask would lead to an erroneous increase in the calcification score. Improvements to this preparatory segmentation step, as were discussed earlier in this paragraph, may be expected to have a positive effect on the results of the material decomposition-based segmentation.

Despite these limitations, however, this method of calcification segmentation is rather promising. After all, the segmentation was found to reflect the pattern of calcification – in terms of distribution between different arterial segments – relatively well on visual inspection, as can be seen from figure 3.11. Additionally, the algorithm was able to separate the vascular calcifications from the iodine contrast agent and metallic endovascular devices relatively well. Furthermore, the algorithm was observed to include relatively small calcifications (several millimeters in size) in the segmentation as well, suggesting good accuracy. This is unsurprising, as this method of calcification segmentation does not rely on anatomic relationships of calcified voxels – i.e. the size of calcifications – but instead uses spectral information to segment these voxels. Finally, this method of calcification segmentation required much less user interaction than the semiautomatic segmentation of the conventional CTA and VNC scans. This may increase reproducibility and decrease the time required for the work-up of a single patient, and thus, this method may be more suitable for implementation in clinical practice. Before this could be achieved, however, further development of this analysis method with regard to the aforementioned limitations is necessary. Additionally, further research in larger patient series should be conducted to find the optimal cutoff point for the CaHA volume fraction, as this cannot be determined based on this analysis of five patients.

The Dice coefficients for the VNC segmentation were observed to be higher than those for the material decomposition segmentation. As was mentioned in the 'Methods' section, the VNC scans were based on a different reconstruction (1/1 mm) than the conventional CTA scan (3/3 mm), on which the other segmentations were based. As a result, the reference segmentation was triplicated to allow comparison by means of a Dice similarity coefficient, which requires equal matrix sizes. This is likely to have caused some discrepancies between these segmentations. Furthermore, the starting position of the two CT reconstructions was observed to differ slightly for several patients, which may have resulted in some degree of misregistration between the reconstructions. As such, the Dice similarity coefficient may be expected to be higher if these issues had been resolved; the effect on a quantitative calcium volume or mass score is likely less pronounced.

The superior agreement of the VNC segmentation with the reference segmentation as compared to the material decomposition segmentation is unsurprising. After all, the former was obtained with the same method as the reference segmentation and through a significant amount of user interaction. This user interaction requirement is also a major drawback of this method. Segmentation of calcifications on a single VNC scan, which typically had around 1100 slices, required the use of three separate software programs and was found to require about one hour of user interaction. Such a time requirement would be unacceptable for the work-up of a single patient in clinical practice. Therefore, the VNC segmentation workflow should be streamlined further to decrease this time requirement. This may be realized by using reconstructing VNC scans with 3 mm slice thickness and interval, which would also decrease noise levels, but may lead to less accurate calcium scores due to partial volume effects. The artery segmentation workflow may also be implemented as an alternative to manual selection of vascular calcifications, which would significantly decrease the amount of user interaction.

Conclusion

The objectives of this patient data analysis were to develop an artery segmentation workflow as a preparatory step to material decomposition analysis and to evaluate the accuracy of calcification segmentation based on material decomposition analysis and VNC scan generation.

The artery segmentation workflow was observed to adequately segment the arterial anatomy up to and including the crural vessels for all patients. As such, the workflow was found to be a feasible preparatory step to the material decomposition analysis. However, several improvements to the algorithm could be made, which should be addressed in further research. This includes decreasing leakage into osseous structures, decreasing the amount of user interaction in fine-tuning the algorithm parameters and only including the TAP by implementing some form of bifurcation detection.

The performance of the material decomposition segmentation was moderate, particularly due to the core of calcifications being excluded from the segmentation. Further development of this algorithm should aim to remedy this, as well as to find the optimal CaHA volume fraction cutoff in large patient series. Nevertheless, the results for this method were promising, indicating good accuracy and performance around metallic implants, as well as following the pattern of calcifications relatively well.

The performance of VNC algorithm in terms of the Dice similarity coefficient was superior to the material decomposition method. However, this method was laborious and time-consuming, making this method infeasible in clinical practice currently. Further streamlining of this method is therefore warranted.

It should be noted that the reference standard in this study, conventional CTA, was imperfect. Further research should also compare these methods to the current golden standard, non-contrast-enhanced CT scans, as well as to each other, to find the method with the best accuracy, reproducibility and speed.

Appendix 3-A – MATLAB script – artery segmentation

```
%% TM M3 Internship - Department of Vascular Surgery, UMC Utrecht - CTA Vessel Segmentation
%
% This script segments the major arteries, i.e. the distal aorta and all
% arteries distal from it up to the ankle, from a CTA image of the lower
% extremities.
%
% This script uses the following function, which must be downloaded from
% the MATLAB Central File Exchange in order for this script to work:
% - Dirk-Jan Kroon (2010). Hessian based Frangi Vesselness filter
% (https://www.mathworks.com/matlabcentral/fileexchange/24409-hessian-based-frangi-vesselness-filter)
%
% Robbert Wiggers, s1543784
% Technical Medicine, University of Twente

clear
close all
clc

%% Loading the CTA series
% Select a DICOM file within the image series:
[file,path] = uigetfile

% The corresponding DICOM series is loaded and the DICOM info is called
% into a struct
CTA = squeeze(dicomreadVolume(path));
info = dicominfo([path file]);

% The CTA volume is converted from uint16 to int16, then rescaled from
% CT-numbers to Hounsfield units using rescaling factors saved within the
% DICOM file information struct.
CTA2 = int16(CTA);
CTA_HU = CTA2*info.RescaleSlope+info.RescaleIntercept;

% The voxel size is saved to allow rescaling of visualizations
voxel_size=[info.PixelSpacing; info.SliceThickness]';
```

```
% The voxel size rescaling terms are remapped for 2D visualizations of coronal and sagittal slices:
voxel_size_proj = [voxel_size(3) voxel_size(1) voxel_size(2)];

%% Selection of a seed point within the aorta
% This seed point will be used as the starting point for the Fast Marching
% Method region growing algorithm

figure(1)
imshow(CTA_HU(:,:,size(CTA_HU,3)),[0 600])             % Shows the first axial slice in the original CTA volume.
annotation('textbox',[0 0.03 0.95 0.1],...             % Help text to instruct the user.
    'String','Select a point within the aorta',...
    'Color','k','EdgeColor','none',...
    'FontWeight','bold',...
    'HorizontalAlignment','center')
ch=drawcrosshair;                                      % Allows the user to click a point.
x=round(ch.Position(1));y=round(ch.Position(2));       % Saves the position of the crosshair.
close figure 1

%% Thresholding
% The image volume is thresholded to remove soft tissue pixels and to
% debulk bone structures.

% A threshold >130 HU and <400 HU works best for most CTA scans; if
% contrast enhancement is slightly higher than 400 HU (~600 HU), the upper
% threshold can be increased.
CTA_thr = CTA_HU>130 & CTA_HU<400;

% If the CTA scan has very strong contrast enhancement (much higher than
% 400 HU), the following threshold can be used instead:
% CTA_thr = CTA_HU>130;

% Voxels outside the threshold range are set to have the attenuation of air
CTA_thr2 = CTA_HU;
CTA_thr2(CTA_thr==0)=min(CTA_HU(:));

%% Frangi vesselness filter (implementation by D.J. Kroon)
% Vesselness filtering according to the method by Frangi et al. is applied
```

```
% to boost the vessels.

folder = cd;

% If the function eig3volume.c is not in MATLAB's default user path folder,
% enter the path for the folder the function is in between the brackets
% in the next line and remove the percent sign
%cd(ENTER FOLDER PATH HERE)

% Compile the 3D eigenvector function:
mex eig3volume.c
cd(folder)

% The parameters for Frangi vesselness filtering are set. See the info
% text of the function 'FrangiFilter3D.m' for more information.
options.FrangiScaleRange = [1 6];               % The scale of the vessels the filter should enhance
options.FrangiScaleRatio = 1;
options.FrangiC = 40;                           % As a rule of thumb, set this constant to the expected
                                                % gray value of the vessels, divided by 4 to 6.
options.BlackWhite = false;                     % Set to detect white vessels on a black background

% Frangi filtering is performed
[CTA_ves,whatscale,Voutx,Vouty,Voutz] =...
    FrangiFilter3D(CTA_thr2,options);

%% Fast Marching Method (FMM) segmentation
% Region growing using the fast marching method is performed in the
% vessel-enhanced image volume, starting from the aortic seed point.

% The weight of each pixel is computed, defined as the difference between its gray value and a
% reference value, in this case the value of the aortic seed point.
W = graydiffweight(CTA_ves,x,y,size(CTA_HU,3));

% Define the sensitivity of the FMM segmentation; the higher the value, the
% more structures are included.
W_thr = 0.015;

% FMM segmentation is performed:
```

```
Segm=imsegfmm(W,x,y,size(CTA_ves,3),W_thr);

%% Visualization of the segmentation - Isosurface
figure
S = isosurface(Segm, 0.5);
h = patch(S, 'Facecolor', [1 0 0], 'EdgeColor', 'none');

isonormals(CTA_ves, h);
lighting('gouraud');                            % Applying Gouraud shading to obtain a 'realistic' visualisation
hlight=camlight('headlight');
axis vis3d;
daspect(1./voxel_size)
campos([324 -1e+04 875])                        % Set the camera position.

%% Visualization of the segmentation - Overlay
Segm_2=cat(4,Segm,zeros(size(Segm)),zeros(size(Segm)));   % Calculates a red RGB image for the segmentation
interval = 5;                                             % The number of slices between subsequent frames
frame_pause = 0.5;                                        % The number of seconds every frame should be shown

figure
for i=0:interval:size(CTA,3)-1                            % Reverses the order of the CTA volume to show the
                                                          % aorta first and the feet last
    shg
    imshow(CTA(:,:,size(CTA,3)-i),[])                     % Plots the CTA slice
    hold on
    overlay = imshow(squeeze(...                          % Plots the segmentation over the CTA slice
        Segm_2(:,:,size(CTA,3)-i,:)))
    overlay.AlphaData = 0.2;
    hold off
    pause(frame_pause)
end
```

General conclusion and future perspectives

PAD is associated with a decrease in functional status and high rates of adverse events and mortality. As the prevalence of PAD rises in concert with the prevalence of cardiovascular risk factors such as diabetes, the burden of PAD on patients and healthcare systems is expected to increase even further, calling for improved risk stratification in this patient group [2]. Therefore, the aim of this research project has been to investigate the quantification of calcification using dual-energy CTA in patients with PAD, as a means towards improved risk stratification in these patients.

As a first step towards this aim, a systematic review was conducted to synthesize the available evidence on peripheral calcium scoring methods and the relationship of calcifications with clinical outcomes. The results of the review showed a clear association of higher calcification scores with severity of ischemia at presentation, lower technical success of endovascular intervention, worse primary patency, an increased risk of TLR, amputation, MALE, MACE and all-cause mortality in patients with PAD. However, there was significant heterogeneity between the studies included in the systematic review, in terms of patient groups, investigated arterial segments and calcium scores used. Therefore, the results of the review called for further research in larger, more homogeneous populations to confirm the found associations, as well as standardization of peripheral calcium scoring. Furthermore, there were several limitations to the studies included in the review, including the use of imaging techniques (CT, DSA) not typically applied as a first-line non-invasive imaging modality and limitations to the ubiquitous quantitative scoring method by Agatston et al. [14].

As such, this research project set out to improve on the limitations of the systematic review, by aiming to develop a standardized method of peripheral calcium scoring, using dual-energy CTA to overcome the disadvantages of CTA, the recommended first-line imaging modality in PAD patients. After all, dual-energy CTA may be used to separate calcifications from the iodine contrast agent, allowing for segmentation of calcifications, an essential step towards automatic, standardized peripheral calcium scoring. This can either be performed through VNC scan generation or by means of material decomposition. The latter also allows for quantification of calcification density [37,38,40]; this overcomes the limitations of the quantitative calcium scoring method proposed by Agatston et al., including non-linearity, false homogeneity and high noise sensitivity [14,34]. Therefore, the aim of the remainder of this research project was to investigate the performance of VNC scan generation and material decomposition for the segmentation of calcifications, as well as quantification of calcification density with material decomposition. To this end, a phantom experiment and an analysis of PAD patient data were performed.

The phantom experiment showed that quantification of calcium density using a three-material decomposition algorithm with water, iodine and calcium hydroxyapatite as basis materials was feasible and relatively accurate for the bone density calibration (BDC) phantom used. However, the results of the experiment also suggested that the presence of other atherosclerotic plaque components (e.g. fatty or fibrous components) might lead to inaccuracies on application of the algorithm to patient data. Therefore, further research should investigate the accuracy of the calcium density quantification on patient data and compare the results with reference data obtained through histopathology; these results could also be used to calibrate the algorithm.

The VNC scan was found to suppress the iodine contrast agent, but also hydroxyapatite. As a result, the hydroxyapatite inserts had attenuation values below the standard calcium scoring threshold of 130 HU after iodine suppression. Therefore, further analysis of this method in patient data was warranted.

The performance of VNC scan generation and material decomposition were analyzed on the data of six patients as well. As a preparatory step before the material decomposition analysis, an algorithm was developed to segment the arteries; by only performing the material decomposition analysis on the voxels in the arterial segmentation mask, the vascular calcifications can be separated from bone tissue, which has the same composition. The semiautomatic arterial segmentation algorithm was shown to adequately segment the arteries for all patients within an acceptable time duration. Nevertheless, the algorithm can still be improved in several aspects, including reduction of leakage, elimination of irrelevant arterial side branches and decreasing the amount of user interaction required.

Segmentations of calcifications based on material decomposition analysis and VNC scans were compared to reference segmentations on conventional CTA scans. While this reference standard should be considered imperfect, due to the established risk of under- or overestimation of calcium scores based on these scans, it did provide an initial indication of the performance of the DECT-based methods. The method based on material decomposition was observed to follow the pattern of calcification relatively well and exhibited good accuracy and separation of iodine, metallic implants and calcification. The Dice similarity coefficient was only moderate, however, mainly due to exclusion of the core of dense calcifications. As such, further development of this method is required.

The VNC scan segmentation showed superior overlap with the reference segmentation. However, this method was found to be too laborious and time-consuming for current use in clinical practice. Further streamlining of this method, e.g. by implementing the artery segmentation algorithm as a preparatory step, is warranted.

While this thesis marks an effort towards standardization of peripheral arterial calcium scoring, the results obtained in the phantom experiment and patient data analysis should be seen as a proof-of-concept. Although the results found for calcification quantification and segmentation were promising, the experiments and analyses performed in this research project represent a relatively small sample size. Therefore, the workflow developed in this project should be applied on larger datasets to validate these methods, which will be done in future research. At the department of Vascular Surgery of the UMC Utrecht, a Peripheral Arterial Obstructive Disease (PAOD) cohort is available, consisting of at least 125 patients with varying degrees of PAD, for whom dual-energy CTA scans are available. A research proposal detailing investigation of calcium scoring and the relationship with clinical outcomes in this cohort has been submitted and approved; this is expected to allow for further testing and refining of this workflow in the foreseeable future.

Aside from confirming the results of the reported experiments and analyses in larger, more diverse patient series, the next step towards a standardized peripheral calcium score should be to calculate several calcification parameters based on the calcification segmentations. An automatic scoring algorithm would be preferable, as this would increase the reproducibility and facilitate the application to large patient series. Statistical analysis should be conducted to identify the calcification parameters with the best predictive value for clinical outcomes. After all, while investigation of the accuracy of calcification detection and scoring is important, the relationship with clinical outcomes ultimately has the most implications for clinical practice.

Originally, this research project aimed to make a start with the calculation of a new, standardized calcium score and statistical analysis to compare this score to clinical outcomes, as is reflected by objectives 2c and 3 in the section 'Research Objectives'. However, this ultimately was not possible within the time frame of this internship due to delay in obtaining the patient data and access to the necessary software. Therefore, future research will have to address these research objectives.

To this end, a research proposal has been submitted to the Utrecht Cardiovascular Cohort (UCC) as well, a prospective biobanking cohort created to establish an infrastructure for standardized data collection in all cardiovascular patients referred to the UMC Utrecht [69,70]. Since 2018 the UCC has been combined with the Second Manifestations of ARTerial disease (SMART) cohort, which started in 1996 [69]. The resulting UCC-SMART cohort, which contains extensive clinical measurement data from 13,300 patients, has previously been used to study the relationship between cardiovascular risk factors and clinical outcomes in patients with or at risk of cardiovascular disease. As such, use of the data of this cohort should provide information on calcification aspects with the best predictive value. In addition, this cohort is expected to include non-contrast-enhanced CT scans as well, which may allow further development of the DECT-based calcification segmentation methods in comparison with the current golden standard. The research proposal for this use has recently been approved as well, so results on this cohort can be expected in the near future as well.

Ultimately, the information obtained from the PAOD cohort, UCC and potentially from other cohorts as well will hopefully allow for the development of a new standardized peripheral arterial calcium score. In turn, this may lead to improved risk stratification in PAD, allowing identification and monitoring of high-risk patients and thereby decreasing the risk of adverse events and improving quality-of-life in this growing patient group.

References

Please note that this bibliography does not include the references of Chapter 1; as this chapter is a systematic review intended to be submitted for publication, the choice was made to present this chapter as a complete article. Therefore, a separate bibliography for this review is given at the end of Chapter 1.

[1] Walker CM, Bunch FT, Cavros NG, Dippel EJ. Multidisciplinary approach to the diagnosis and management of patients with peripheral arterial disease. Clin Interv Aging. 2015;10:1147–53. https://doi.org/10.2147/CIA.S79355

[2] Conte MS, Bradbury AW, Kolh P, White J v, Dick F, Fitridge R, et al. Global Vascular Guidelines on the Management of Chronic Limb-Threatening Ischemia. European journal of vascular and endovascular surgery : the official journal of the European Society for Vascular Surgery. 2019;58(1S):S1-S109.e33. https://doi.org/10.1016/j.ejvs.2019.05.006

[3] Cassar K. Intermittent claudication. BMJ. 2006;333(7576):1002–5. https://doi.org/10.1136/bmj.39001.562813.DE

[4] Norgren L, Hiatt WR, Dormandy JA, Nehler MR, Harris KA, Fowkes FGR. Inter-Society Consensus for the Management of Peripheral Arterial Disease (TASC II). J Vasc Surg. 2007;45 Suppl S:S5-67. https://doi.org/10.1016/j.jvs.2006.12.037

[5] Fowkes FGR, Rudan D, Rudan I, Aboyans V, Denenberg JO, McDermott MM, et al. Comparison of global estimates of prevalence and risk factors for peripheral artery disease in 2000 and 2010: a systematic review and analysis. The Lancet. 2013;382(9901):1329–40. https://doi.org/10.1016/S0140-6736(13)61249-0

[6] Song P, Rudan D, Zhu Y, Fowkes FJI, Rahimi K, Gerald F, et al. Global, regional, and national prevalence and risk factors for peripheral artery disease in 2015: an updated systematic review and analysis. 2019; https://doi.org/10.1016/S2214-109X(19)30255-4

[7] Goodney PP, Travis LL, Nallamothu BK, Holman K, Suckow B, Henke PK, et al. Variation in the use of lower extremity vascular procedures for critical limb ischemia. Circ Cardiovasc Qual Outcomes. 2012;5(1):94–102. https://doi.org/10.1161/CIRCOUTCOMES.111.962233

[8] Reinecke H, Unrath M, Freisinger E, Bunzemeier H, Meyborg M, Lüders F, et al. Peripheral arterial disease and critical limb ischaemia: still poor outcomes and lack of guideline adherence. Eur Heart J. 2015;36(15):932–8. https://doi.org/10.1093/eurheartj/ehv006

[9] Mills JL, Conte MS, Armstrong DG, Pomposelli FB, Schanzer A, Sidawy AN, et al. The Society for Vascular Surgery Lower Extremity Threatened Limb Classification System: Risk stratification based on Wound, Ischemia, and foot Infection (WIfI). Journal of Vascular Surgery. 2014;59(1):220-234.e2. https://doi.org/10.1016/j.jvs.2013.08.003

[10] Zhan LX, Branco BC, Armstrong DG, Mills JL. The Society for Vascular Surgery lower extremity threatened limb classification system based on Wound, Ischemia, and foot Infection (WIfI) correlates with risk of major amputation and time to wound healing. Journal of Vascular Surgery. 2015;61(4):939–44. https://doi.org/10.1016/j.jvs.2014.11.045

[11] Falk E. Pathogenesis of atherosclerosis. J Am Coll Cardiol. 2006;47(8 Suppl):C7-12. https://doi.org/10.1016/j.jacc.2005.09.068

[12] Abedin M, Tintut Y, Demer LL. Vascular Calcification. Arteriosclerosis, Thrombosis, and Vascular Biology. 2004;24(7):1161–70. https://doi.org/10.1161/01.ATV.0000133194.94939.42

[13] Hardman RL, Jazaeri O, Yi J, Smith M, Gupta R. Overview of classification systems in peripheral artery disease. Seminars in Interventional Radiology. 2014;31(4):378–88. https://doi.org/10.1055/s-0034-1393976

[14] Agatston AS, Janowitz WR, Hildner FJ, Zusmer NR, Viamonte M, Detrano R. Quantification of coronary artery calcium using ultrafast computed tomography. J Am Coll Cardiol. 1990;15(4):827–32. https://doi.org/10.1016/0735-1097(90)90282-T

[15] Greenland P, Bonow RO, Brundage BH, Budoff MJ, Eisenberg MJ, Grundy SM, et al. ACCF/AHA 2007 Clinical Expert Consensus Document on Coronary Artery Calcium Scoring By Computed Tomography in Global Cardiovascular Risk Assessment and in Evaluation of Patients With Chest Pain: A Report of the American College of Cardiology Foundation Cl. J Am Coll Cardiol. 2007;49(3):378–402. https://doi.org/10.1016/j.jacc.2006.10.001

[16] Adelhoefer S, Uddin SMI, Osei AD, Obisesan OH, Blaha MJ, Dzaye O. Coronary Artery Calcium Scoring: New Insights into Clinical Interpretation-Lessons from the CAC Consortium. Radiol Cardiothorac Imaging. 2020;2(6):e200281–e200281. https://doi.org/10.1148/ryct.2020200281

[17] Bastos Gonçalves F, Voûte MT, Hoeks SE, Chonchol MB, Boersma EE, Stolker RJ, et al. Calcification of the abdominal aorta as an independent predictor of cardiovascular events: a meta-analysis. Heart. 2012;98(13):988–94. https://doi.org/10.1136/heartjnl-2011-301464

[18] Rocha-Singh KJ, Zeller T, Jaff MR. Peripheral arterial calcification: prevalence, mechanism, detection, and clinical implications. Catheterization and cardiovascular interventions : official journal of the Society for Cardiac Angiography & Interventions. 2014;83(6):E212-20. https://doi.org/10.1002/ccd.25387

[19] Richtlijn Perifeer Arterieel Vaatlijden. Federatie Medisch Specialisten - Richtlijnendatabase. 2016; Available from: https://richtlijnendatabase.nl/richtlijn/perifeer_arterieel_vaatlijden_pav/pav_-_startpagina.html

[20] Aboyans V, Ricco J-B, Bartelink M-LEL, Björck M, Brodmann M, Cohnert T, et al. 2017 ESC Guidelines on the Diagnosis and Treatment of Peripheral Arterial Diseases, in collaboration with the European Society for Vascular Surgery (ESVS): Document covering atherosclerotic disease of extracranial carotid and vertebral, mesenteric, renal. Eur Heart J. 2018;39(9):763–816. https://doi.org/10.1093/eurheartj/ehx095

[21] Hong JY, Han K, Jung JH, Kim JS. Association of Exposure to Diagnostic Low-Dose Ionizing Radiation with Risk of Cancer among Youths in South Korea. JAMA Network Open. 2019;2(9). https://doi.org/10.1001/jamanetworkopen.2019.10584

[22] Met R, Bipat S, Legemate DA, Reekers JA, Koelemay MJW. Diagnostic Performance of Computed Tomography Angiography in Peripheral Arterial Disease: A Systematic Review and Meta-analysis. JAMA. 2009;301(4):415–24. https://doi.org/10.1001/jama.301.4.415

[23] Li P, Xu L, Yang L, Wang R, Hsieh J, Sun Z, et al. Blooming Artifact Reduction in Coronary Artery Calcification by A New De-blooming Algorithm: Initial Study. Scientific Reports. 2018;8(1):6945. https://doi.org/10.1038/s41598-018-25352-5

[24] Hoffmann U, Ferencik M, Cury RC, Pena AJ. Coronary CT Angiography. Journal of Nuclear Medicine. 2006;47(5):797 LP – 806. https://doi.org/10.1056/NEJMoa1201161

[25] Wexler L. What Is the Value of Measuring Coronary Artery Calcification? Radiology. 2008;246(1):1–2. https://doi.org/10.1148/radiol.2461071333

[26] Moselewski F, Ferencik M, Achenbach S, Abbara S, Cury RC, Booth SL, et al. Threshold-dependent variability of coronary artery calcification measurements - Implications for contrast-enhanced multi-detector row-computed tomography. European Journal of Radiology. 2006;57(3):390–5. https://doi.org/10.1016/j.ejrad.2005.12.026

[27] Mühlenbruch G, Wildberger JE, Koos R, Das M, Flohr TG, Niethammer M, et al. Coronary Calcium Scoring Using 16-Row Multislice Computed Tomography: Nonenhanced Versus Contrast-Enhanced Studies In Vitro and In Vivo. Investigative Radiology. 2005;40(3). https://doi.org/10.1097/01.rli.0000153024.12712.10

[28] Almutairi A, Sun Z. Dual Energy Computed Tomography Angiography in the Peripheral Arterial Imaging: A Systematic Review of Image Quality, Radiation Dose and Diagnostic Value. Current Medical Imaging. 2017;13(1):66–72. https://doi.org/10.2174/1573405612666160602122647

[29] van Ommen F, Bennink E, Vlassenbroek A, Dankbaar JW, Schilham AMR, Viergever MA, et al. Image quality of conventional images of dual-layer SPECTRAL CT: A phantom study. Medical Physics. 2018;45(7):3031–42. https://doi.org/10.1002/mp.12959

[30] Tran DN, Straka M, Roos JE, Napel S, Fleischmann D. Dual-energy CT Discrimination of Iodine and Calcium: Experimental Results and Implications for Lower Extremity CT Angiography. Academic Radiology. 2009;16(2):160–71. https://doi.org/10.1016/j.acra.2008.09.004

[31] Karçaaltıncaba M, Aktaş A. Dual-energy CT revisited with multidetector CT: review of principles and clinical applications. Diagn Interv Radiol. 2011;17(3):181–94. https://doi.org/10.4261/1305-3825.DIR.3860-10.0

[32] Yamada Y, Jinzaki M, Okamura T, Yamada M, Tanami Y, Abe T, et al. Feasibility of coronary artery calcium scoring on virtual unenhanced images derived from single-source fast kVp-switching dual-energy coronary CT angiography. Journal of Cardiovascular Computed Tomography. 2014;8(5):391–400. https://doi.org/10.1016/j.jcct.2014.08.005

[33] Schwarz F, Nance JW, Ruzsics B, Bastarrika G, Sterzik A, Schoepf UJ, et al. Quantification of Coronary Artery Calcium on the Basis of Dual-Energy Coronary CT Angiography. Radiology. 2012;264(3). https://doi.org/10.1148/radiol.12112455/-/DC1

[34] Demer LL, Tintut Y, Nguyen K-L, Hsiai T, Lee JT. Rigor and Reproducibility in Analysis of Vascular Calcification. Circ Res. 2017;120(8):1240–2. https://doi.org/10.1161/CIRCRESAHA.116.310326

[35] Hoffmann U, Siebert U, Bull-Stewart A, Achenbach S, Ferencik M, Moselewski F, et al. Evidence for lower variability of coronary artery calcium mineral mass measurements by multi-detector computed tomography in a community-based cohort—Consequences for progression studies. European Journal of Radiology. 2006;57(3):396–402. https://doi.org/10.1016/j.ejrad.2005.12.027

[36] Rutten A, Isgum I, Prokop M. Coronary Calcification: Effect of Small Variation of Scan Starting Position on Agatston, Volume, and Mass Scores. Radiology. 2008;246(1):90–8. https://doi.org/10.1148/radiol.2461070006

[37] Patino M, Prochowski A, Agrawal MD, Simeone FJ, Gupta R, Hahn PF, et al. Material Separation Using Dual-Energy CT: Current and Emerging Applications. RadioGraphics. 2016;36(4):1087–105. https://doi.org/10.1148/rg.2016150220

[38] Machida H, Tanaka I, Fukui R, Shen Y, Ishikawa T, Tate E, et al. Dual-Energy Spectral CT: Various Clinical Vascular Applications. RadioGraphics. 2016;36(4):1215–32. https://doi.org/10.1148/rg.2016150185

[39] Dehmeshki J, Ye X, Amin H, Abaei M, Lin X, Qanadli SD. Volumetric Quantification of Atherosclerotic Plaque in CT Considering Partial Volume Effect. IEEE Transactions on Medical Imaging. 2007;26(3):273–82. https://doi.org/10.1109/TMI.2007.893344

[40] McCollough CH, Leng S, Yu L, Fletcher JG. Dual- and Multi-Energy CT: Principles, Technical Approaches, and Clinical Applications. Radiology. 2015;276(3):637–53. https://doi.org/10.1148/radiol.2015142631

[41] McKetty MH. The AAPM/RSNA physics tutorial for residents. X-ray attenuation. RadioGraphics. 1998;18(1):151–63. https://doi.org/10.1148/radiographics.18.1.9460114

[42] Hobbie RK, Roth BJ. Intermediate Physics for Medicine and Biology. 5th ed. Cham: Springer International Publishing; 2015. https://doi.org/10.1007/978-3-319-12682-1

[43] Alvarez RE, Macovski A. Energy-selective reconstructions in X-ray computerised tomography. Physics in Medicine and Biology. 1976;21(5):733–44. https://doi.org/10.1088/0031-9155/21/5/002

[44] Shahmohammadi Beni M, Krstic D, Nikezic D, Yu KN. Monte Carlo studies on photon interactions in radiobiological experiments. PLOS ONE. 2018;13(3):e0193575-. https://doi.org/10.1371/journal.pone.0193575

[45] Lehmann LA, Alvarez RE, Macovski A, Brody WR, Pelc NJ, Riederer SJ, et al. Generalized image combinations in dual KVP digital radiography. Medical Physics. 1981;8(5):659–67. https://doi.org/10.1118/1.595025

[46] Bearden JA, Burr AF. Reevaluation of X-Ray Atomic Energy Levels. Reviews of Modern Physics. 1967;39(1):125–42. https://doi.org/10.1103/RevModPhys.39.125

[47] Schilham A. *Unpublished data.* UMC Utrecht; 2021.

[48] Ananthakrishnan L, Duan X, Rajiah P, Soesbe TC, Lewis MA, Xi Y, et al. Phantom Validation of Spectral Detector Computed Tomography-Derived Virtual Monoenergetic, Virtual Noncontrast, and Iodine Quantification Images. Journal of Computer Assisted Tomography. 2018;42(6):959–64. https://doi.org/10.1097/RCT.0000000000000763

[49] Simons MV. Quantification of calcification with dual energy imaging in peripheral arterial disease. MSc Thesis – Technical Medicine. University of Twente; 2020.

[50] Proudfoot D, Shanahan CM, Weissberg PL. Vascular calcification: new insights into an old problem. The Journal of Pathology. 1998;185(1):1–3. https://doi.org/10.1002/(SICI)1096-9896(199805)185:1<1::AID-PATH89>3.0.CO;2-J

[51] Bone Density Calibration Phantoms For HU vs. HA calibrations with respect to Bone Mineral Densitometry evaluation of bones. QRM. Accessed on 04/04/2022. Available from: https://qrm.de/en/products/bone-density-calibration-phantoms

[52] Ultravist. Bayer Pharmaceuticals. Accessed on 04/04/2022. Available from: https://www.radiology.bayer.com/products/ultravist

[53] Awai K, Inoue M, Yagyu Y, Watanabe M, Sano T, Nin S, et al. Moderate versus High Concentration of Contrast Material for Aortic and Hepatic Enhancement and Tumor-to-Liver Contrast at Multi–Detector Row CT. Radiology. 2004;233(3):682–8. https://doi.org/10.1148/radiol.2333031617

[54] Yanaga Y, Awai K, Nakaura T, Oda S, Funama Y, Bae KT, et al. Effect of Contrast Injection Protocols with Dose Adjusted to the Estimated Lean Patient Body Weight on Aortic Enhancement at CT Angiography. American Journal of Roentgenology. 2009;192(4):1071–8. https://doi.org/10.2214/AJR.08.1407

[55] Bae KT. Intravenous Contrast Medium Administration and Scan Timing at CT: Considerations and Approaches. Radiology. 2010;256(1):32–61. https://doi.org/10.1148/radiol.10090908

[56] Berger MJ, Hubbell JH, Seltzer SM, Chang J, Coursey JS, Sukumar R, et al. XCOM: Photon Cross Sections Database. NIST Standard Reference Database 8 (XGAM). 2010; https://doi.org/10.18434/T48G6X

[57] Boas FE, Fleischmann D. CT artifacts: Causes and reduction techniques. Imaging in Medicine. 2012;4(2). Available from: www.edboas.com/science/CT/0012.pdf

[58] Ecoflex(TM) 00-50. Smooth-On, Inc. Accessed on 04/12/2022. Available from: https://www.smooth-on.com/products/ecoflex-00-50/

[59] Arnold BA, Budoff MJ, Child J, Xiang P, Mao SS. Coronary calcium test phantom containing true CaHA microspheres for evaluation of advanced CT calcium scoring methods. Journal of Cardiovascular Computed Tomography. 2010;4(5):322–9. https://doi.org/10.1016/j.jcct.2010.08.004

[60] Bishop PD, Feiten LE, Ouriel K, Nassoiy SP, Pavkov ML, Clair DG, et al. Arterial Calcification Increases in Distal Arteries in Patients with Peripheral Arterial Disease. Annals of Vascular Surgery. 2008;22(6):799–805. https://doi.org/10.1016/j.avsg.2008.04.008

[61] Hellings WE, Moll FL, de Kleijn DP v, Pasterkamp G. 10-years experience with the Athero-Express study. Cardiovasc Diagn Ther. 2012;2(1):63–73. https://doi.org/10.3978/j.issn.2223-3652.2012.02.01

[62] Moselewski F, O'Donnell CJ, Achenbach S, Ferencik M, Massaro J, Nguyen A, et al. Calcium concentration of individual coronary calcified plaques as measured by multidetector row computed tomography. Circulation. 2005;111(24):3236–41. https://doi.org/10.1161/CIRCULATIONAHA.104.489781

[63] Szpinda M. External diameters of the crural arteries in patients with chronic critical limb ischaemia. Folia Morphologica. 2005;64(4):315–20. Available from: https://pubmed.ncbi.nlm.nih.gov/16425159

[64] Frangi AF, Niessen WJ, Vincken KL, Viergever MA. Multiscale vessel enhancement filtering. In: Wells WM, Colchester A, Delp S, editors. Medical Image Computing and Computer-Assisted

Intervention — MICCAI'98. Berlin, Heidelberg: Springer Berlin Heidelberg; 1998. p. 130–7. https://doi.org/10.1007/BFb0056195

[65] Kroon D-J. Hessian based Frangi Vesselness filter. MATLAB Central File Exchange. 2010 Accessed on 02/01/2022. Available from: https://www.mathworks.com/matlabcentral/fileexchange/24409-hessian-based-frangi-vesselness-filter

[66] Sethian JA. Level Set Methods and Fast Marching Methods: Evolving Interfaces in Computational Geometry, Fluid Mechanics, Computer Vision, and Materials Science. 2nd ed. Cambridge University Press; 1999.

[67] Yushkevich PA, Piven J, Hazlett HC, Smith RG, Ho S, Gee JC, et al. User-guided 3D active contour segmentation of anatomical structures: Significantly improved efficiency and reliability. Neuroimage. 2006;31(3):1116–28. https://doi.org/https://doi.org/10.1016/j.neuroimage.2006.01.015

[68] Zou KH, Warfield SK, Bharatha A, Tempany CMC, Kaus MR, Haker SJ, et al. Statistical validation of image segmentation quality based on a spatial overlap index. Acad Radiol. 2004;11(2):178–89. https://doi.org/10.1016/s1076-6332(03)00671-8

[69] Utrecht Cardiovascular Cohort. UMC Utrecht. Accessed on 09/03/2021. Available from: https://www.umcutrecht.nl/en/utrecht-cardiovascular-cohort

[70] Asselbergs FW, Visseren FLJ, Bots ML, de Borst GJ, Buijsrogge MP, Dieleman JM, et al. Uniform data collection in routine clinical practice in cardiovascular patients for optimal care, quality control and research: The Utrecht Cardiovascular Cohort. European Journal of Preventive Cardiology. 2017;24(8):840–7. https://doi.org/10.1177/2047487317690284